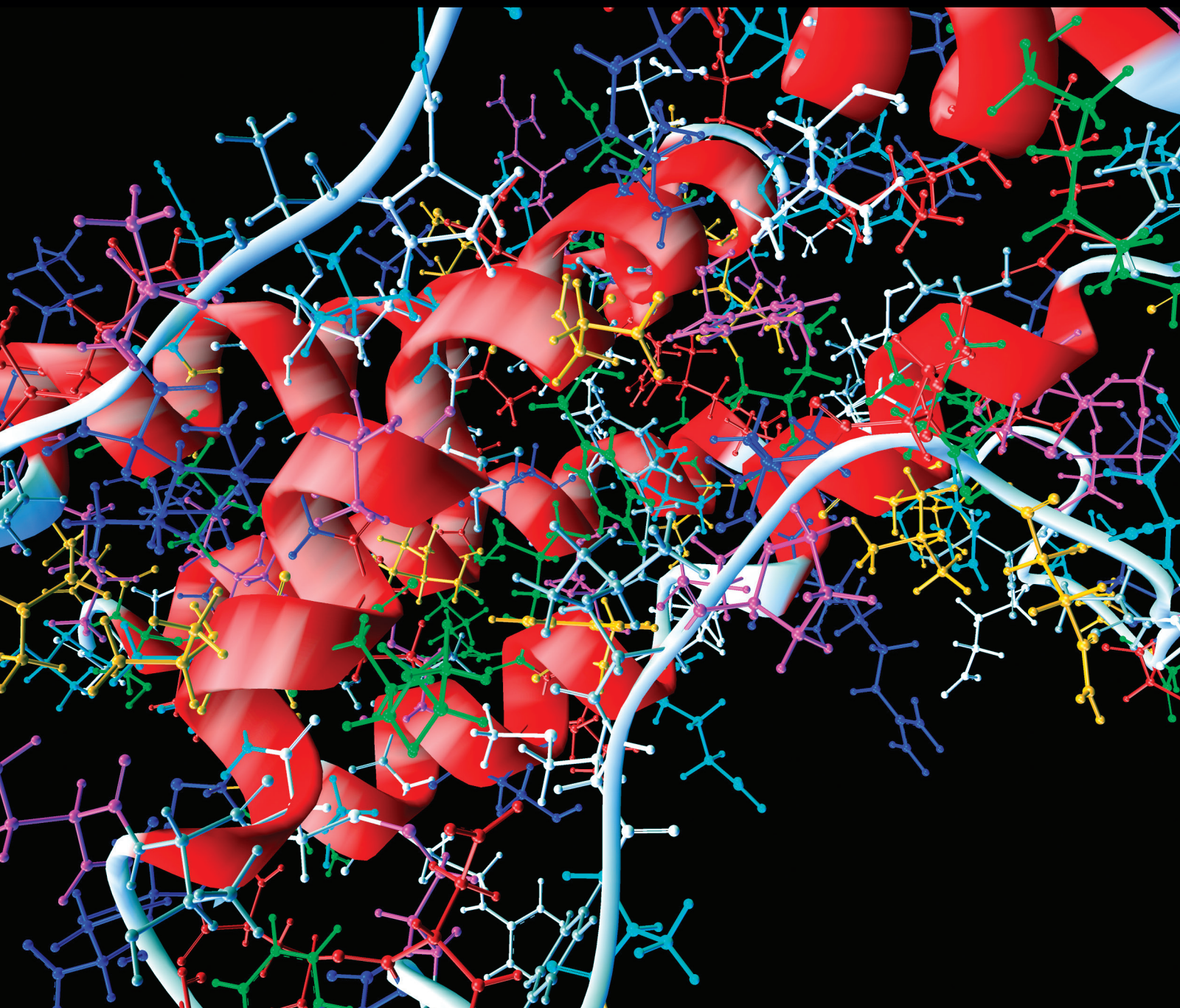


Computational and Mathematical Methods in Medicine

Computational Advances in Cardiovascular Health

Lead Guest Editor: Dominique J. Monlezun

Guest Editors: Francesco Nordio and Tianhua Niu





Computational Advances in Cardiovascular Health

Computational and Mathematical Methods in Medicine

Computational Advances in Cardiovascular Health

Lead Guest Editor: Dominique J. Monlezun

Guest Editors: Francesco Nordio and Tianhua Niu



Copyright © 2019 Hindawi. All rights reserved.

This is a special issue published in “Computational and Mathematical Methods in Medicine.” All articles are open access articles distributed under the Creative Commons Attribution License, which permits unrestricted use, distribution, and reproduction in any medium, provided the original work is properly cited.

Editorial Board

Raul Alcaraz, Spain
Emil Alexov, USA
Konstantin G. Arbeev, USA
Georgios Archontis, Cyprus
Enrique Berjano, Spain
Junguo Bian, USA
Elia Biganzoli, Italy
Konstantin Blyuss, UK
Hans A. Braun, Germany
Zoran Bursac, USA
Thierry Busso, France
Guy Carrault, France
Filippo Castiglione, Italy
Carlos Castillo-Chavez, USA
Prem Chapagain, USA
Hsiu-Hsi Chen, Taiwan
Wai-Ki Ching, Hong Kong
Nadia A. Chuzhanova, UK
Maria N. D.S. Cordeiro, Portugal
Cristiana Corsi, Italy
Irena Cosic, Australia
Qi Dai, China
Chuangyin Dang, Hong Kong
Didier Delignières, France
Jun Deng, USA
Thomas Desaive, Belgium
David Diller, USA
Michel Dojat, France
Irina Doytchinova, Bulgaria
Esmaeil Ebrahimie, Australia
Georges El Fakhri, USA
Issam El Naqa, USA
Angelo Facchiano, Italy

Luca Faes, Italy
Maria E. Fantacci, Italy
Giancarlo Ferrigno, Italy
Marc Thilo Figge, Germany
Alfonso T. García-Sosa, Estonia
Humberto González-Díaz, Spain
Igor I. Goryanin, Japan
Marko Gosak, Slovenia
Damien Hall, Australia
Roberto Hornero, Spain
Tingjun Hou, China
Seiya Imoto, Japan
Hsueh-Fen Juan, Taiwan
Martti Juhola, Finland
Rafik Karaman, Palestine
Andrzej Kloczkowski, USA
Chung-Min Liao, Taiwan
Ezequiel López-Rubio, Spain
Pinyi Lu, USA
Reinoud Maex, Belgium
Valeri Makarov, Spain
Kostas Marias, Greece
Juan Pablo Martínez, Spain
Richard J. Maude, Thailand
Michele Migliore, Italy
John Mitchell, UK
Luminita Moraru, Romania
Chee M. Ng, USA
Michele Nichelatti, Italy
Kazuhisa Nishizawa, Japan
Francesco Pappalardo, Italy
Manuel F. G. Penedo, Spain
Jesús Picó, Spain

Kemal Polat, Turkey
Alberto Policriti, Italy
Giuseppe Pontrelli, Italy
Jesús Poza, Spain
Christopher Pretty, New Zealand
Mihai V. Putz, Romania
Jose Joaquin Rieta, Spain
Jan Rychtar, USA
Vinod Scaria, India
Simon A. Sherman, USA
Dong Song, USA
Xinyuan Song, Hong Kong
João M. Tavares, Portugal
Jlenia Toppi, Italy
Nelson J. Trujillo-Barreto, UK
Anna Tsantili-Kakoulidou, Greece
Markos G. Tsipouras, Greece
Po-Hsiang Tsui, Taiwan
Gabriel Turinici, France
Liangjiang Wang, USA
Ruisheng Wang, USA
David A. Winkler, Australia
Gabriel Wittum, Germany
Yu Xue, China
Yongqing Yang, China
Chen Yanover, Israel
Xiaojun Yao, China
Kaan Yetilmezsoy, Turkey
Hiro Yoshida, USA
Henggui Zhang, UK
Yuhai Zhao, China
Xiaoqi Zheng, China

Contents

Computational Advances in Cardiovascular Health

Dominique J. Monlezun , Francesco Nordio, and Tianhua Niu 
Editorial (2 pages), Article ID 2985984, Volume 2019 (2019)

Model-Based Quantification of Left Ventricular Diastolic Function in Critically Ill Patients with Atrial Fibrillation from Routine Data: A Feasibility Study

Nicholas Kiefer, Maximilian J. Oremek , Andreas Hoeft , and Sven Zenker 
Research Article (11 pages), Article ID 9682138, Volume 2019 (2019)

Arrhythmia Classification of ECG Signals Using Hybrid Features

Syed Muhammad Anwar , Maheen Gul , Muhammad Majid , and Majdi Alnowami 
Research Article (8 pages), Article ID 1380348, Volume 2018 (2019)

Biomechanical Aspects of Closing Approaches in Postcarotid Endarterectomy

Idit Avrahami , Dafna Raz, and Oranit Bash
Research Article (10 pages), Article ID 4517652, Volume 2018 (2019)

The Time-Domain Integration Method of Digital Subtraction Angiography Images

Shuo Huang , Le Cheng, Bin Zhu, Ping Zhou, Yu Sun , Bing Zhang , and Suiren Wan
Research Article (5 pages), Article ID 5284969, Volume 2018 (2019)

Analysis of Exercise-Induced Periodic Breathing Using an Autoregressive Model and the Hilbert-Huang Transform

Tieh-Cheng Fu, Chaur-Chin Chen, Ching-Mao Chang , Hen-Hong Chang , and Hsueh-Ting Chu 
Research Article (8 pages), Article ID 4860204, Volume 2018 (2019)

Wall Shear Stress Estimation of Thoracic Aortic Aneurysm Using Computational Fluid Dynamics

J. Febina, Mohamed Yacin Sikkandar , and N. M. Sudharsan 
Research Article (12 pages), Article ID 7126532, Volume 2018 (2019)

Editorial

Computational Advances in Cardiovascular Health

Dominique J. Monlezun ¹, **Francesco Nordio**,² and **Tianhua Niu** ³

¹Department of Cardiology, University of Texas M.D. Anderson Cancer Center, Houston, USA

²Department of Medicine, Brigham and Women's Hospital, Harvard University, Boston, USA

³Department of Medicine, Tulane University School of Medicine, New Orleans, USA

Correspondence should be addressed to Dominique J. Monlezun; dominique.j.monlezun@uth.tmc.edu

Received 16 April 2019; Accepted 16 April 2019; Published 13 June 2019

Copyright © 2019 Dominique J. Monlezun et al. This is an open access article distributed under the Creative Commons Attribution License, which permits unrestricted use, distribution, and reproduction in any medium, provided the original work is properly cited.

Cardiovascular disease (CVD) is the world's top mortality cause, accounting for 1 in 3 deaths and 1 in 5 dollars of the American healthcare system. Patients deserve more effective, affordable, equitable care—and now—yet we in the clinical and research community struggle to accelerate the rate of reliable and replicable results to keep pace with this growing global epidemic. Computational advances in statistics and machine learning are increasingly bridging the informatics and physiological pipeline uniting precision medicine and population health, getting us thankfully closer to adequately addressing patient needs.

Through improved computational models, we could attain a better understanding of the physiologic (-omics, electrophysiology, solid mechanics, fluid dynamics), clinical (disease trajectories, pharmacology, comorbidity interaction), and population (social networks, social determinants, policies, inequities, and ecosystems of health) factors that help produce the complex phenomenon of CVD. Computational advances must simplify the CVD problem, so we can act, reassess, and act again on the problem through incremental research gains in a growing snowball fashion. Clinically, patients need such methodological improvements; financially, their medical costs are unsustainable; and most important, ethically, our patients deserve faster, better, cheaper results from medical science. Health systems internationally are responding to (or forced to react to) these societal changes—patients are rightfully demanding better treatments, clinicians are expecting better data to guide their decisions, payers are requiring higher value care, and regulatory and funding bodies are mandating greater transparent and impact research. Yet where to begin, or go from

here in CVD, is nearly as obtuse as the complexity of the above challenges we face as there are no widely accepted evidence-based standards in these computational advances, nor how to optimally apply them to reverse the CVD epidemic.

This special issue therefore aims at accelerating the dissemination of promising CVD computational advances. We received 15 submissions worldwide, and after performing rigorous and careful peer review, 6 of them were selected for this special issue. These resultant published studies provided novel computational, statistical, and machine learning approaches or clinical application to improve modelling for blood flow dynamics, solid mechanics, breath wave dynamics, and electrical cardiac rhythm for such patient populations as those affected by aortic aneurysm and dissection, atrial fibrillation, congestive heart failure, and arrhythmias.

One flow dynamic study conducted by J. Febina et al. created a 3D non-Newtonian mathematical model of pulsatile cardiac blood flow using CT data to map thoracic aortic aneurysm for computational fluid dynamics (CFD) to thus demonstrate wall shear stress (WSS) as a predictor for impending rupture, risk stratified throughout the cardiac cycle and stress conditions. This model notably included the vortex formation pattern and flow reversal (as in WSS) and therefore provided evidence for WSS nonoverly predicted through non-Newtonian pulsatile flow (similar to the natural physiology of the cardiac cycle of contraction and relaxation) but overpredicted when the natural flow pattern of laminar-turbulent-laminar is added to the non-Newtonian pattern. Newtonian fluid dynamics on the other hand were

deployed in a different study performed by I. Avrahami and colleagues to assess carotid blood flow and wall dynamics in multiple bifurcation scenarios (normal, narrowed post-operatively with suture, and widened with high, medium, and lower flexibility patches) using fluid-structure interaction (FSI) numerical simulations. This was done to aid in the clinical decision about suture-based carotid endarterectomy versus patch-based angioplasty. The analysis suggested primary suture was superior to patch angioplasty by higher stress and high oscillatory shear index (OSI) along with lower time-averaged wall shear stress (TAWSS), with the high flexibility patch outperforming the lower flexibility patch. Image improvement was the focus of a third flow dynamic study conducted by Huang and co-workers. In this, an image time-domain integration modelled on blood flow periodicity was proposed to streamline improvements in image and noise suppression for digital subtraction angiography (DSA). In this model, postcontrast cardiac cycle images were synthesized for independent application or as a postprocessing noise suppression technique. This approach demonstrated good real-time performance and efficiency for enhancement and noise suppression in aortic dissection. Flow dynamics were included with solid mechanics in another paper by N. Kiefer et al., in which a global optimization algorithm was proposed and deployed in 17 critically ill atrial fibrillation (AF) patients to approximate diastolic stiffness (to aid in the diagnosis of left ventricular diastolic dysfunction (LVDD)) through a mathematical solution for the ill-posed nonlinear inverse problem of parameter estimation rooted in the physiological model of diastolic filling. This study provides the first known quantification of LV diastolic function using routine clinical data from critically ill patients with AF.

Breath wave dynamics were assessed in the study of T.-C. Fu et al. using an autoregressive (AR) mathematical model created to analyze breath-by-breath exercise test data to better analyze cardiopulmonary exercise testing (CPET) exercised-induced periodic breathing (PB) to prognosticate congestive heart failure (CHF). Hilbert–Huang transform (HHT) was utilized to decompose the AR model’s breath-by-breath values into intrinsic mode functions (IMFs), mathematically representative of individual breath’s physiologic oscillation in various frequencies. This model demonstrated predictive performance for CHF prognosis based on the third and fourth IMF components among 61 CHF patients, evidencing the biologic basis as a physiologic reserve indicated by ventilation and the above HHT approach to modelling CHF.

Finally, electrical cardiac rhythm was studied in another paper of S. M. Anwar et al. on dynamic and morphological electrocardiogram (ECG) features which were utilized in a novel approach for arrhythmia classification using discrete wavelet transform (DWT, dimensionality reduced by independent component analysis to minimize redundancy) for heart beats and Teager energy operator for nonlinear dynamic RR intervals. These features were then run through a threefold cross-validation neural network algorithm, which was then compared with the MIT-BIH databases for arrhythmia (13,724 beats) and supraventricular arrhythmia

(22,151 beats). Accuracy for class- and subject-orientated schemes was improved to 99.75% and 99.84% using this unique approach. Machine learning methods, such as neural network applied in this paper, and other popular algorithms including support vector machine, k-nearest neighbor, decision tree, and random forest, are gaining attention in their applications for -omics research and precision medicine to augment translational clinical research, notably by providing the unique advantages of handling high-dimensional data more efficiently than traditional statistical strategies.

To the researchers who submitted these accepted manuscripts and those which were not, we are grateful for their shared commitment to improved scientific understanding and thus clinical care. We hope that, in some small way, the cardiovascular computational advances they contain may not only improve the patient care to which they apply but also accelerate the CVD research to which their methodologies can be more broadly adapted. Our patients and populations deserve better care. And so we offer this special issue as a humble step forward, believing in the promise of such computational advances to help speed up the journey for conquering CVD together as a global human family.

Conflicts of Interest

The editors declare that there are no conflicts of interest regarding the publication of this article.

*Dominique J. Monlezun
Francesco Nordio
Tianhua Niu*

Research Article

Model-Based Quantification of Left Ventricular Diastolic Function in Critically Ill Patients with Atrial Fibrillation from Routine Data: A Feasibility Study

Nicholas Kiefer,^{1,2} Maximilian J. Oremek ,³ Andreas Hoeft ,¹ and Sven Zenker ^{1,3}

¹Department of Anesthesiology & Intensive Care Medicine, University of Bonn Medical Center, Bonn, Germany

²Department of Anesthesiology, Intensive Care Medicine and Pain Treatment, Hospital Dortmund, Dortmund, Germany

³Applied Mathematical Physiology (AMP) Lab, Department of Anesthesiology & Intensive Care Medicine, University of Bonn Medical Center, Bonn, Germany

Correspondence should be addressed to Sven Zenker; zenker@uni-bonn.de

Received 13 July 2018; Accepted 17 March 2019; Published 16 May 2019

Academic Editor: Tianhua Niu

Copyright © 2019 Nicholas Kiefer et al. This is an open access article distributed under the Creative Commons Attribution License, which permits unrestricted use, distribution, and reproduction in any medium, provided the original work is properly cited.

Introduction. Left ventricular diastolic dysfunction (LVDD) and atrial fibrillation (AF) are connected by pathophysiology and prevalence. LVDD remains underdiagnosed in critically ill patients despite potentially significant therapeutic implications since direct measurement cannot be performed in routine care at the bedside, and echocardiographic assessment of LVDD in AF is impaired. We propose a novel approach that allows us to infer the diastolic stiffness, β , a key quantitative parameter of diastolic function, from standard monitoring data by solving the nonlinear, ill-posed inverse problem of parameter estimation for a previously described mechanistic, physiological model of diastolic filling. The beat-to-beat variability in AF offers an advantageous setting for this. **Methods.** By employing a global optimization algorithm, β is inferred from a simple six parameter and an expanded seven parameter model of left ventricular filling. Optimization of all parameters was limited to the interval $]0, 400[$ and initialized randomly on large intervals encompassing the support of the likelihood function. Routine ECG and arterial pressure recordings of 17 AF and 3 sinus rhythm (SR) patients from the PhysioNet MGH/MF Database were used as inputs. **Results.** Estimation was successful in 15 of 17 AF patients, while in the 3 SR patients, no reliable estimation was possible. For both models, the inferred β ($0.065 \pm 0.044 \text{ ml}^{-1}$ vs. $0.038 \pm 0.033 \text{ ml}^{-1}$ ($p = 0.02$) simple vs. expanded) was compatible with the previously described (patho) physiological range. Aortic compliance, α , inferred from the expanded model ($1.46 \pm 1.50 \text{ ml/mmHg}$) also compared well with literature values. **Conclusion.** The proposed approach successfully inferred β within the physiological range. This is the first report of an approach quantifying LVDF from routine monitoring data in critically ill AF patients. Provided future successful external validation, this approach may offer a tool for minimally invasive online monitoring of this crucial parameter.

1. Introduction

Heart failure (HF) and atrial fibrillation (AF) are both frequent cardiovascular conditions that share an increasing prevalence and cause significant morbidity, mortality, and socioeconomic burden [1–5]. Incidence correlates with age [6–8]. In the USA, HF is the most frequent reason for unplanned/medical ICU admission, either primarily as acute HF or as an aggravating comorbidity [9].

About half of HF patients present with left ventricular diastolic dysfunction (LVDD) [5, 10, 11], a condition termed “heart failure with preserved ejection fraction” (HFpEF). LVDD and AF are closely connected by pathophysiology and prevalence: LVDD precipitates AF, and the absence of atrial contraction in AF aggravates LVDD [12–15]. AF is the most common arrhythmia in HF with 65% of HFpEF presenting with AF [16]. AF is associated with increased mortality in HFpEF [17]. Although in cardiology, HFpEF

has become a very common diagnosis, LVDD remains underdiagnosed in the ICU population, despite a potentially large impact on therapeutic decisions [18].

In critically ill patients, prevalence of AF is increased [19] and left ventricular diastolic function (LVDF) may be additionally impaired [20]. Assessment and monitoring of LVDF in presence of AF is challenging as standard echocardiographic measures (E/A , E/E') are difficult to obtain and do not allow for continuous monitoring [21]. Acquisition of invasive measures such as the left ventricular diastolic time constant (τ) is not feasible at the bedside [22].

The fundamental cardiovascular physiology approach to quantify diastolic cardiac function involves the recording of pressure-volume loops under varying preload conditions to estimate the nonlinear diastolic pressure-volume relationship [23]:

$$P_{LV}(V_{LV}) = P_{LV0} \left(e^{\beta(V_{LV} - V_{ED0})} - 1 \right), \quad (1)$$

where β quantifies the exponential diastolic ventricular stiffness, P_{LV0} represents the pressure scaling factor, and V_{ED0} corresponds to the unstressed volume.

According to Frank–Starling’s law and given an otherwise stationary state, variations in end-diastolic volume (EDV) determine beat-to-beat stroke volume variability [24]. In the absence of synchronised atrial contraction in AF, EDV primarily depends on the duration of filling, the diastolic properties of the ventricle, preload, and the end-systolic volume, which in turn depends on the previous cardiac cycle and the systolic properties of the ventricle. Previous attempts to quantify the relationship between variable filling times in AF and stroke volume have produced heterogeneous results [25].

The application of nonlinear mathematical representations of physiology based on solving the inverse problem of parameter estimation from available observations/measurements has become feasible at the bedside due to the recent availability of affordable high-performance computational resources [26, 27]. For such a model-based approach, AF patients are a particularly promising population due to the high intrinsic variability in observable physiological time series. This variability effectively acts as a continuous high-bandwidth perturbation of the underlying biological system, facilitating system identification and subsequent parameter estimation within a short observation period.

Zenker et al. have previously described a simple, nonlinear, mechanistic model of the left ventricle [28]. We hypothesized that inversion of this model would allow quantitative inference of parameters of LVDF from routine ECG and invasive arterial pressure (ABP) recordings in AF patients under minimal assumptions. The aim of this study was to assess whether inference of β , the exponential diastolic ventricular stiffness, is feasible using global optimisation. Additionally, we aimed to evaluate whether uncertainty quantification from the local covariance would allow for robust identification of individual patients in which inference failure occurred.

2. Materials and Methods

2.1. Ethical Approval. The dataset used in this study is freely available and fully deidentified. Thus, no ethical restrictions apply in this context.

2.2. Data Acquisition. We used the PhysioNet [29] Massachusetts General Hospital/Marquette Foundation (MGH/MF) Waveform Database [30]. It contains recordings of patient’s physiological signals including ECG and invasive ABP. The data are 360 Hz 8-bit time series in the PhysioNet binary format. Patients were selected using the patient guide, which contained limited clinical information such as cardiac rhythm. We screened the entire database with regard to documented cardiac rhythm and extracted datasets for two patient groups: the AF group (17 patients) included all patients with AF without pacemakers or intermittent non-AF cardiac rhythms in the available low-noise areas of the recordings. The sinus rhythm (SR) control group included 3 patients with documented SR without ECG alterations or an arrhythmia described in the patient guide.

2.3. Signal Processing and Data Selection. RR intervals (RRIs) were calculated based on an ECG R peak detection algorithm derived from methods described by Arzeno and coworkers [31]. Pulse pressures (PPs) were computed from ABP recordings using an algorithm adapted from Zong et al. [32]. Manual selection of low-noise intervals was then performed to extract 800 pairs of RRIs followed by pulse pressures (PPs). The resulting RRI and PP time series are made available as text files in the online supplement.

2.4. Software Development and Implementation. The main data processing and inference routine was implemented in C++ using the ADOL-C 2.63 [33], Armadillo v8.2 [34], Boost v1.60 [35], and TRNG4 4.19 [36] libraries. The data were visualised and postprocessed using Python v3.6 [37] with the numpy v1.13 [38], Matplotlib v2.1 [39], pandas v0.19 [40], and SciPy v1.0 [41] packages. The estimation of the covariance used MATLAB R2017a, (The Mathworks, Inc, Natick, Massachusetts, USA). The analysis code is available in the online supplement Code.

2.5. Mathematical Model. The mechanistic model of the left ventricle used in this paper derives the diastolic filling behaviour from a simple ODE:

$$V_{ED}(t_{\text{dia}}) = k_3(t_{\text{dia}} + C) - \frac{1}{\beta} \ln \left(\frac{1 - k_1 e^{\beta k_3(t+C)}}{k_3} \right), \quad (2)$$

whose solution predicts end-diastolic volume, V_{ED} , from filling times, t_{dia} , the exponential diastolic stiffness parameter, β , the time shift constant, C , and two combined parameters k_1 and k_3 , which in addition to β , the mitral valve resistance, R_{valve} , and the filling pressure, P_{cvp} , incorporate parameters P_{LV0} and V_{ED0} of the nonlinear pressure-volume relationship [28].

$$\begin{aligned}
k_1 &= \frac{-P_{LV0}}{R_{valve}} e^{-\beta V_{ED0}}, \\
k_3 &= \frac{P_{LV0}}{R_{valve}} + \frac{P_{cvp}}{R_{valve}},
\end{aligned}
\tag{3}$$

where k_1 and k_3 both include the term P_{LV0}/R_{valve} , with k_1 additionally depending on β and V_{ED0} . This interdependence warrants constraint considerations for valid combinations when solving the inverse problem. More information on the model parameters and the limits is provided in the online supplement Expanded Methods-Modeling and Constraints (available here).

The model predicts volumes, whereas in routine data, only pressure measurements are readily available. To convert volumes into pressures, we assume a linear model of the static aortic pressure-volume relationship, expressing pulse pressures as a function of diastolic filling time t_{dia} with the aortic compliance, α , and the zero-offset, δ :

$$PP_i = \frac{V_{ED}(t_{dia i})}{\alpha} + \delta. \tag{4}$$

Equations (2) and (4) jointly define the simple model (SM), in which only the diastolic properties of the left ventricle and aortic pressure-volume relationship are taken into account.

After fitting the SM resulting from equation (4) to patient data, we observed a strong systematic dependence of residuals on the RRI preceding the RRI directly determining the filling duration. Such a dependence has previously been attributed to variations of the inotropic state of the heart, among other things [42, 43]. The model was therefore expanded to include a simple linear correction to compensate these effects. The pulse pressure of the i^{th} beat for this expanded model (EM) then depends on an additional factor k_4 weighting the contribution of the prepreceding RRI:

$$PP_i = \frac{V_{ED}(t_{dia i}) + k_4 * t_{dia i-1}}{\alpha} + \delta. \tag{5}$$

2.6. Global Optimisation. Since initial exploration showed that efficient local optimization algorithms of various types became trapped almost immediately in the local minima in the neighbourhood of randomly chosen starting points, we were forced to fall back to parallel tempering (PT) as a computationally expensive global optimization technique to obtain estimation results independent of subjective choices of starting points [44]. The likelihood was calculated assuming a normally distributed, independent measurement error with a standard deviation (SD) of 12 mmHg for PPs. To minimize the potential influence of assumptions on results, we constrained optimization for all parameters to]0, 400[, a range much larger than known or reasonable physiological constraints. Additionally, the optimization was initialised randomly, rejecting randomly chosen starting points if the local log-likelihood did not exceed a threshold of -5208 , an empirically chosen limit corresponding to the likelihood at a sum of squares error of 1,500,000 mmHg². This was done to ascertain initialisation of the PT on the support of the

likelihood function to obtain appreciable acceptance rates. Based on experience from exploratory sampling runs to determine the support of the likelihood function, the following initialization intervals were chosen: k_1 , β , and C by a uniform distribution in log space]-40, 4[, k_3 by a uniform distribution]120, 400[, α by a uniform distribution]0, 5[, and δ by a uniform distribution]20, 80[.

We ran 40 million PT samples using 24 chains, with a randomised starting point for each chain within the support and a multivariate Gaussian proposal distribution with a diagonal, empirically determined covariance fixed across all patients. The chains were separated by an exponential temperature ladder with base 6. The code, data, and instructions are made available in the online supplement (available here).

2.7. Statistics/Uncertainty Quantification. The best (maximum) likelihood vector (BLV) seen by the sampler was used to compute Pearson's R^2 as a measure of observed fraction of variation explained (FVE) by the model. At this parameter vector, the uncertainty was calculated by estimating the covariance from a local Hessian, regularized following the recommendations of Gill and King [45]. Details are discussed in the online supplement Expanded Methods-Uncertainty Quantification (available here).

The residuals with respect to the filling and prefilling interval were evaluated for any systematic errors. All data are presented as mean \pm standard deviation (SD). Groups were compared using the Mann-Whitney rank sum test, and a two-tailed $p < 0.05$ was considered statistically significant [46].

3. Results

3.1. Patient Population. The analysis included 17 AF and 3 SR patients with mean age 72.5 ± 9.79 yrs and 37.3 ± 25.8 yrs, respectively. The SR group did not have any documented preexisting cardiovascular diseases and included two patients with orthopaedic/trauma diagnosis and one with sepsis. The AF group included 10 patients with various cardiovascular primary diagnoses, four patients with gastrointestinal diagnoses, and one patient each with sepsis, cerebral haemorrhage, and renal calculus with retroperitoneal haematoma.

Mean RRIs and PPs of the individual patient did not differ significantly between AF and SR groups (0.68 ± 0.11 s vs. 0.76 ± 0.04 s, $p = 0.20$; 71.1 ± 17 mmHg vs. 57.8 ± 18 mmHg, $p = 0.20$). Individual variability expressed as SD of RRIs and PPs was significantly higher in the AF group compared to the SR group (SD of RRI 0.12 ± 0.04 s vs. 0.024 ± 0.01 s, $p < 0.005$; SD of PP 12.45 ± 5.65 mmHg vs. 2.89 ± 0.37 mmHg, $p < 0.005$). Within the AF group, two patients (Patient IDs: mgh013 and mgh130) displayed a low variability of RRI (SD of RRI 0.06 s and 0.048 s, respectively) similar to the SR group.

3.2. Population Level Estimation Results: Goodness of Fit and Uncertainty Estimation. The BLVs for both simple model (SM) and expanded model (EM) provided excellent fits to the observed RRI-PP relationships in 15 of 17 AF patients,

with the EM largely eliminating the systematic dependency on the RRI preceding the RRI determining the filling time. FVE was 0.53 ± 0.17 vs. 0.70 ± 0.21 , $p = 0.007$ for SM and EM, respectively. For SR patients, both models were unable to provide adequate fits, as evidenced by the low values of FVE (0.017 ± 0.013 vs. 0.062 ± 0.04 , $p = 0.38$). Examples are provided in Figure 1, showing a side-by-side comparison of the models for a typical sinus and AF patient. Plots of all patients are available in the online supplement Expanded Results (available here).

BLV values of β in AF patients were $0.065 \pm 0.044 \text{ ml}^{-1}$ vs. $0.038 \pm 0.033 \text{ ml}^{-1}$ ($p = 0.02$) for SM and EM, respectively. The EM values of 15 out of 17 AF patients were within the range reported by Kass et al. ($0.044 \pm 0.024 \text{ ml}^{-1}$) [47], whilst on average slightly exceeding the range described by Schmitt et al. ($0.023 \pm 0.006 \text{ ml}^{-1}$) [48], whose measurements were performed in a younger and healthier cohort, who may quite plausibly present with a more compliant ventricle. For all SR patients, values of β were in a similar but higher range ($0.096 \pm 0.049 \text{ ml}^{-1}$ vs. $0.11 \pm 0.016 \text{ ml}^{-1}$ $p = 0.66$).

The only other estimated parameter for which we were able to find literature values is capacitive aortic compliance in ml/mmHg. This was reported in the study by Cohn et al., Duprez et al., Liu et al., and McVeigh et al. [49–52] ranging from 0.8 ml/mmHg to 2.2 ml/mmHg. SM and EM showed values of $3.22 \pm 2.11 \text{ ml/mmHg}$ vs. $1.46 \pm 1.50 \text{ ml/mmHg}$ ($p = 0.04$), respectively, for AF patients. The inferred aortic compliance values of the expanded, but not the simple, model thus compared well with the physiological range.

For both models, the residuals with respect to filling time, prefilling interval, and observed pulse pressure were inspected. A typical example for an AF patient is shown in Figures 2(a)–2(c). For both models, the residuals with respect to filling time appear to be randomly distributed. In the residuals with respect to the prefilling interval, the dependence seen when applying SM is no longer present for the EM. In the case of dependence of residuals on the observed pulse pressure, SM shows a stronger correlation than the EM.

The parameters discussed and their estimated individual errors, as well as the FVE for all individual patients, are summarised in Table 1.

3.3. Individual Inference Results: Identifying Inference Failure. The FVE values in Table 1 allow the identification of one patient (identifier: mgh145) for which both models are not able to explain more than 13% of the observed variation. Further investigation of this patient showed that the measurement data violated the model assumption of stationarity, as seen in Figure 3.

Another outlier can be seen in the values of β for patient mgh130. Whilst this patient shows values within the physiological range for the simple model, the expanded model shows an extreme value of 0.005 ml^{-1} , which is an entire order of magnitude smaller than the expected range. Looking more closely at the input data, the patient shows a linear trend without the nonlinear plateau seen in the plot of pulse pressure vs. filling time as is present in the other AF

patients. Figure 4 shows the plot for mgh130 as compared to typical AF patients in Figure 1.

A further tool for identification of model failure was tested through estimation of the error associated with the parameter vector from the local Hessian. The values are shown in Table 1 for the estimated error on β . Comparison between simple and expanded model shows a mean value across all patients of $0.03 \pm 0.03 \text{ ml}^{-1}$ vs. $0.009 \pm 0.008 \text{ ml}^{-1}$ ($p = 0.01$), suggesting a significantly smaller estimation uncertainty in the expanded model, in addition to the larger FVE. Similarly, comparing the error on the aortic compliance, α , yields $4.54 \pm 4.31 \text{ ml/mmHg}$ vs. $1.38 \pm 1.48 \text{ ml/mmHg}$, $p < 0.05$. Unfortunately, the estimation of the covariance did not flag the previously described model failures or highlight any new AF patients when looking at the errors on β or α .

To summarize, we were able to identify a measure of the diastolic ventricular stiffness within the physiological range for both models from routine data using a mechanistic mathematical model. The simple model described only diastolic features of the left ventricle but produced a strong dependence in residuals with respect to the prefilling interval. An expansion of the model using a correcting term, which takes the RR interval prior to filling into account, not only largely eliminated this dependency but additionally provided estimates of aortic compliance within the physiological range.

4. Discussion

4.1. Inference Results. Our hypothesis was that model-based quantitative inference would enable us to determine exponential diastolic ventricular stiffness, β , an important quantitative parameter of diastolic cardiac function, from ECG and ABP measurements in patients with AF, but not in patients with sinus rhythm. The probability that all global estimates with global search initialized across and constrained to a huge interval would by chance almost without exception converge to values within the comparatively tiny physiological range corresponding to approx. 0.05% of the constraint interval appears vanishingly small. Thus, our data clearly support this hypothesis. This is, to our knowledge, the first report of quantitative estimation of diastolic ventricular function from routine clinical monitoring data in patients with AF.

Not only did employing the expanded model result in improved fits as was expected but also allowed inference of an additional parameter, aortic compliance, within the reported physiological range of 0.8 ml/mmHg to 2.2 ml/mmHg. Interestingly, estimation uncertainty was reduced for the expanded model, as well. Whether this is an artefact of the regularized uncertainty estimation procedure in the presence of ill-posedness and thus local noninvertibility of the Hessian at the maximum likelihood estimate or an effect of reduced misspecification remains to be elucidated.

4.2. Identifiability of Inference Failure. With respect to potential clinical application, robust and, ideally, automatically determining valid individual inference results is crucial. In this investigation, we observed a case in which the violation

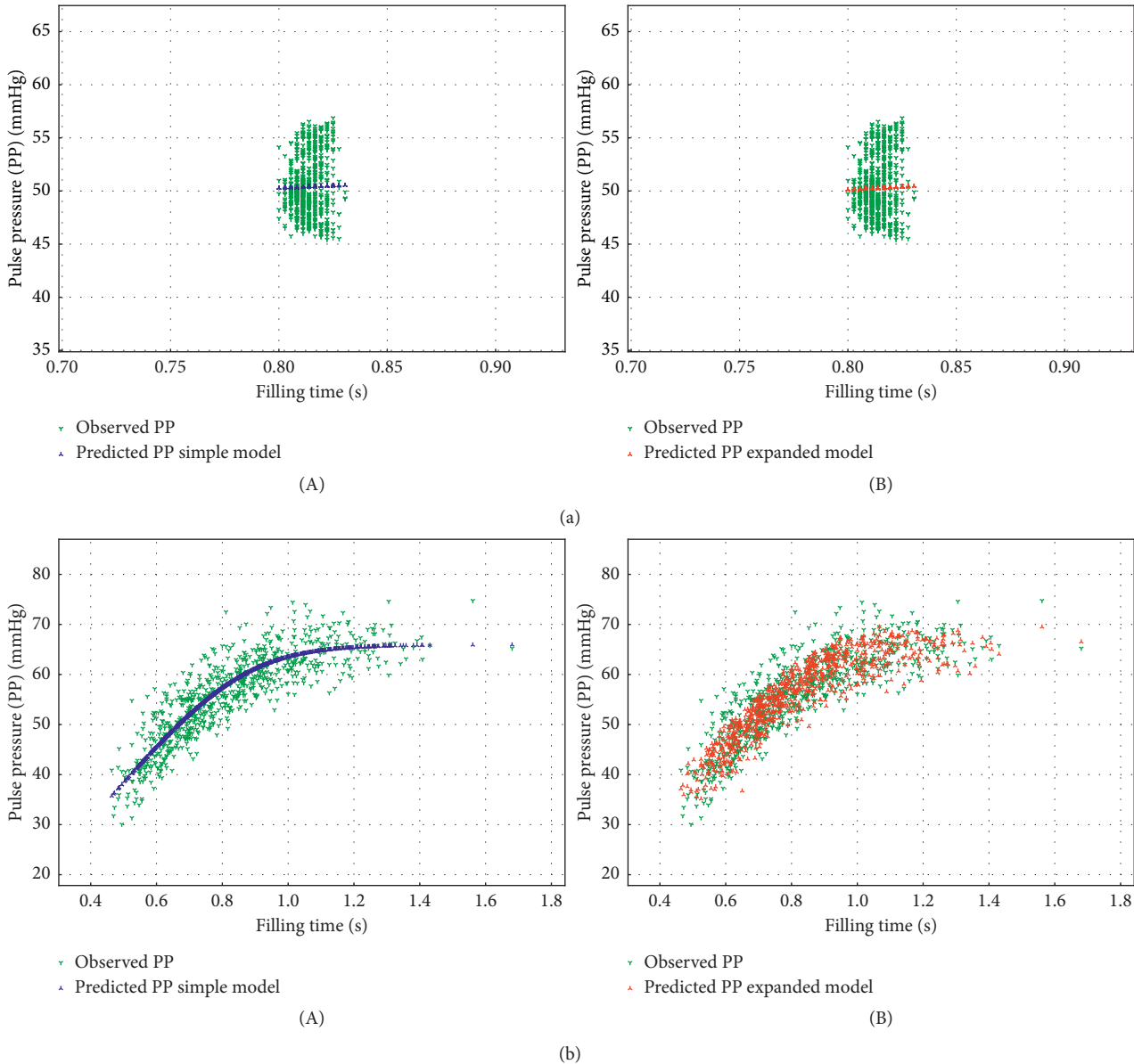


FIGURE 1: Observed (green) vs. predicted (blue for the simple model, red for the expanded model) relationship between pulse pressures (PPs) and filling times for a typical sinus rhythm patient (mgh079) (a) and a typical atrial fibrillation patient (mgh126) (b). (A) Simple model. (B) Expanded model.

of the model assumption of stationarity resulted in an extremely low FVE for both models. In the expanded model, a second outlier was identifiable only through the implausibly low (by an order of magnitude below the physiological range) β value. When inspecting the data, we found that this patient did not exhibit the nonlinear plateau seen in the other patients, resulting in the optimization effectively converging to a linear reduced model as β approaches zero rather than the full nonlinear model. Neither of these patients were identifiable from the covariance matrix at the point of best likelihood seen by the sampler when inspecting the errors on β and aortic compliance, suggesting either a thresholding approach or comparison of FVE with a reduced linear model as possible ways of identifying this type of inference failure induced by insufficient or nonstationary data in practice.

In the SR patients, no adequate fit to the observed pulse pressures was achieved, as evidenced by the low FVE values and supported by visual inspection of fits and residuals. Yet, the inferred values of β were only slightly above the physiological range. Inspecting the errors as estimated from the covariance matrix showed larger errors for both β and aortic compliance. The actual usefulness of this estimation, however, appears questionable as the model's assumptions are violated by the underlying physiology in sinus patients. Ultimately, only experimental corroboration will determine usefulness in the clinical setting.

When examining residuals for systematic errors and comparing results between the simple and expanded model, it becomes apparent that focusing on the diastolic properties of the ventricle only cannot explain the entire beat-

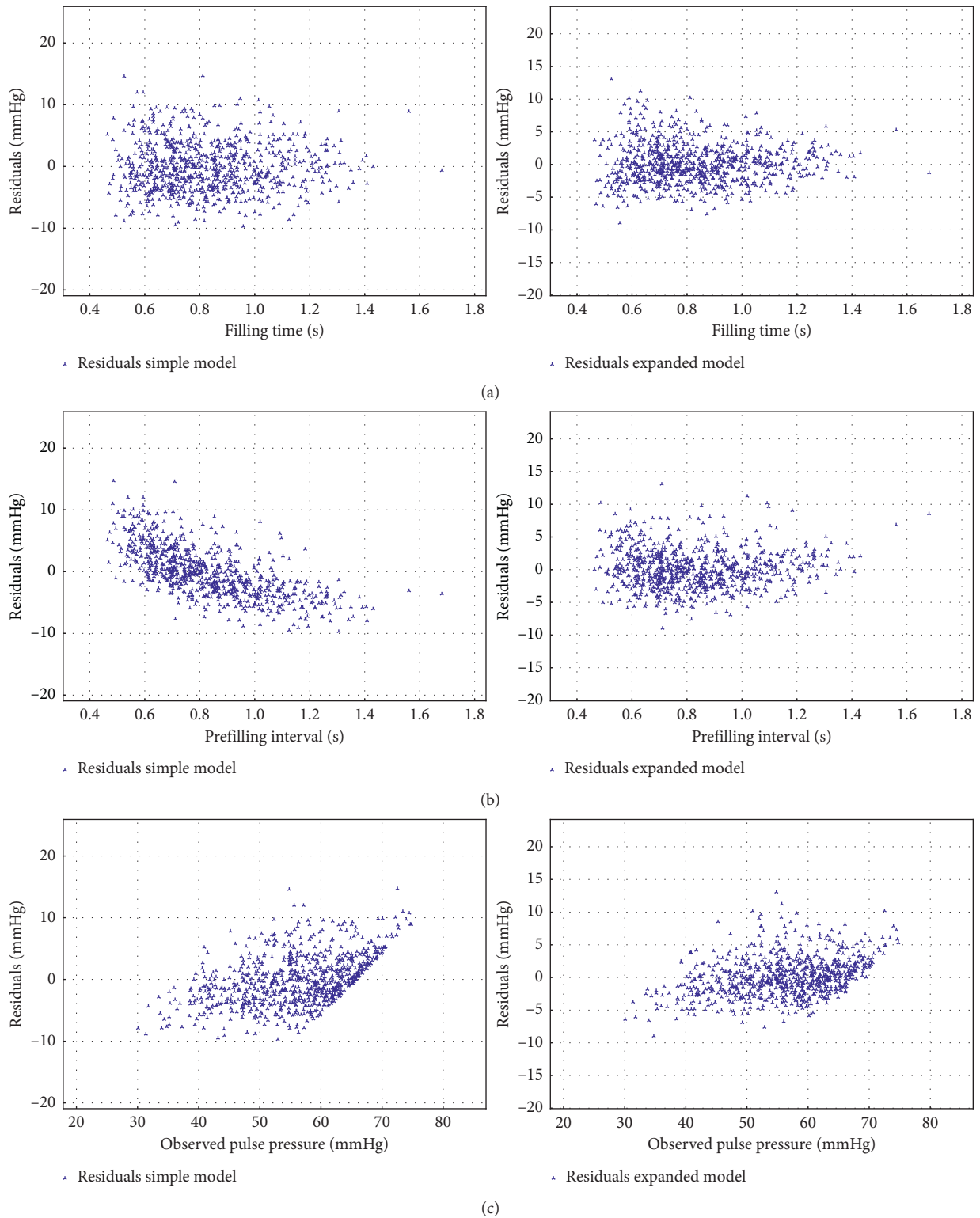


FIGURE 2: Residuals with respect to filling interval, prefilling interval, and observed pulse pressures for mgh126, a typical AF patient: residuals with respect to the (a) filling interval for the simple and expanded model, (b) RR interval prior to the filling interval for the simple and expanded model, and (c) observed pulse pressure for the simple and expanded model.

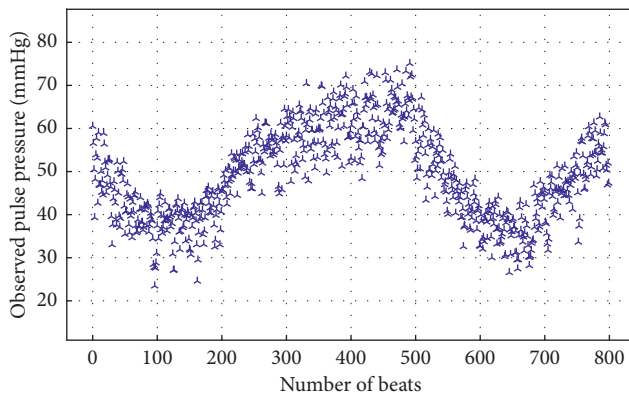
to-beat variability. Taking into account the systematic dependence on the prefilling interval in the expanded model largely resolved this systematic dependence in the residuals

but not the systematic dependence of residuals on observed values. This suggests a role for more realistic, physiologically motivated models directly accounting for effects of end-

TABLE 1: Summary of patient characteristics and results for both models. The results were rounded to three significant figures where applicable.

Patient	Age	Rhythm	Mean RR \pm SD (s)	Mean PP \pm SD (mmHg)	FVE simple model	β simple model \pm EE (ml^{-1})	α simple model \pm EE (ml/mmHg)	FVE expanded model	β expanded model \pm EE (ml^{-1})	α expanded model (ml/mmHg)
mgh013	73	AF	0.787 \pm 0.06	72.1 \pm 7.89	0.36	0.0755 \pm 0.0215	3.86 \pm 3.58	0.48	0.0136 \pm 0.00205	0.711 \pm 0.621
mgh019	79	AF	0.75 \pm 0.11	46.5 \pm 12.9	0.5	0.0649 \pm 0.104	3.71 \pm 8.11	0.82	0.150 \pm 0.0244	0.684 \pm 0.237
mgh023	78	AF	0.794 \pm 0.19	108.3 \pm 18.3	0.73	0.0347 \pm 0.0050	2.80 \pm 2.14	0.91	0.0124 \pm 0.00113	1.25 \pm 0.985
mgh027	73	AF	0.671 \pm 0.175	70.6 \pm 19.1	0.45	0.0700 \pm 0.0343	4.07 \pm 2.48	0.64	0.0471 \pm 0.0104	1.70 \pm 0.594
mgh032	78	AF	0.733 \pm 0.15	76.0 \pm 15.6	0.82	0.0378 \pm 0.0103	3.01 \pm 3.39	0.93	0.0198 \pm 0.00415	0.880 \pm 2.36
mgh105	86	AF	0.628 \pm 0.16	51.5 \pm 8.70	0.53	0.128 \pm 0.0655	7.60 \pm 11.5	0.73	0.0368 \pm 0.00916	5.37 \pm 3.88
mgh126	46	AF	0.830 \pm 0.203	55.9 \pm 8.47	0.77	0.0218 \pm 0.0051	4.70 \pm 5.87	0.87	0.0335 \pm 0.00855	4.98 \pm 4.13
mgh129	63	AF	0.420 \pm 0.08	80.8 \pm 22.0	0.51	0.0574 \pm 0.0269	1.03 \pm 2.68	0.74	0.0472 \pm 0.00516	0.529 \pm 0.398
mgh130	73	AF	0.856 \pm 0.05	59.7 \pm 4.06	0.5	0.105 \pm 0.0621	5.62 \pm 10.38	0.74	0.0052 \pm 0.00112	0.622 \pm 0.177
mgh135	65	AF	0.549 \pm 0.11	88.9 \pm 11.8	0.44	0.0523 \pm 0.0089	0.324 \pm 0.432	0.47	0.0553 \pm 0.0220	0.333 \pm 0.463
mgh139	64	AF	0.608 \pm 0.13	82.4 \pm 13.8	0.7	0.0387 \pm 0.0084	2.33 \pm 1.41	0.834	0.0187 \pm 0.00796	0.652 \pm 0.749
mgh141	73	AF	0.714 \pm 0.14	56.9 \pm 12.7	0.41	0.0125 \pm 0.0034	0.252 \pm 0.069	0.58	0.0112 \pm 0.00237	0.461 \pm 0.208
mgh144	71	AF	0.735 \pm 0.12	74.1 \pm 7.69	0.52	0.0538 \pm 0.0137	5.64 \pm 2.27	0.76	0.0441 \pm 0.0112	2.40 \pm 3.69
mgh145	81	AF	0.578 \pm 0.09	49.1 \pm 10.6	0.13	0.0459 \pm 0.0062	0.482 \pm 0.151	0.14	0.0672 \pm 0.0286	2.57 \pm 3.85
mgh146	87	AF	0.637 \pm 0.08	97.7 \pm 8.94	0.34	0.0736 \pm 0.0388	3.59 \pm 14.83	0.46	0.0347 \pm 0.00548	0.560 \pm 0.260
mgh147	76	AF	0.533 \pm 0.11	70.1 \pm 24.6	0.61	0.0340 \pm 0.0092	0.511 \pm 0.481	0.86	0.0328 \pm 0.00424	0.211 \pm 0.215
mgh149	67	AF	0.706 \pm 0.09	78.7 \pm 8.15	0.64	0.194 \pm 0.0845	5.18 \pm 7.46	0.89	0.0110 \pm 0.00173	0.955 \pm 0.596
mgh059	25	S	0.717 \pm 0.04	44.7 \pm 2.73	0.02	0.160 \pm 0.516	44.89 \pm 177	0.09	0.118 \pm 0.0823	19.8 \pm 12.2
mgh079	20	S	0.813 \pm 0.02	50.4 \pm 2.64	0	0.0862 \pm 0.241	10.93 \pm 9.51	0.01	0.124 \pm 0.0942	31.4 \pm 24.6
mgh152	67	S	0.764 \pm 0.02	78.4 \pm 3.33	0.03	0.0409 \pm 0.0226	27.7 \pm 51.0	0.1	0.0880 \pm 0.211	4.71 \pm 3.12

AF = atrial fibrillation; S = sinus; RR = ECG R-peak intervals; PP = pulse pressure; SD = standard deviation; FVE = fraction of variation explained; β = left ventricular diastolic stiffness; α = aortic compliance; EE = error estimate.



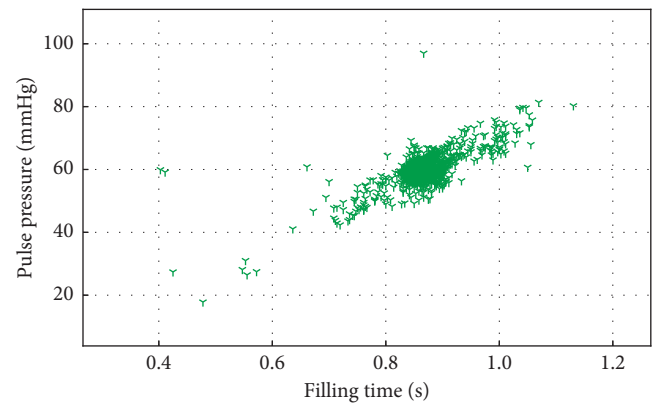
▲ Observed pulse pressure time series

FIGURE 3: Example of the nonstationary time series of pulse pressures in patient mgh145, leading to inference failure due to violation of modeling assumptions.

systolic volume, inotropic state, and afterload on ventricular performance.

4.3. Clinical Relevance. Our findings, if transferable to the bedside, are of high clinical importance for the large group of ICU patients with combined AF and LVDD.

To our knowledge, no epidemiological data on the combined prevalence of LVDD and AF in critically ill patients exist in the literature, but it is likely to be high. Quantification of LVDD is impaired in presence of AF, while it is of significant clinical importance in critically ill patients.



▼ Observed pulse pressure

FIGURE 4: Example of atrial fibrillation patient (mgh130) without nonlinear plateau of pulse pressures for higher filling times, leading to estimation of a degenerate linear rather than the informative nonlinear model.

Treatment of acute heart failure in the ICU typically focuses on adjusting systolic function, volume balance, and peripheral resistance, usually based on combining volume therapy with catecholaminergic inotropes and vasopressors. These catecholamines may further impair diastolic function, if their contractile effect outweighs their lusitropic effect, a condition commonly referred to as overstimulation [53]. LVDD plays a key role in overstimulation, and presence of inflammation may further aggravate this mechanism [53]. Milrinone and levosimendan, in contrast, have been shown to improve diastolic function [54–56]. Also, LVDD plays a

role in weaning pulmonary edema and weaning failure [57]. Our approach may thus enable automated, continuous, and user-independent assessment of LVDF, providing online guidance for differential intensive care therapy of shock. In the future, the continuous monitoring of LVDD may lead to novel insights into the physiology of diastolic function under volume and catecholaminergic therapy in the ICU setting. It might also contribute to provide better guidance to volume therapy in the AF subpopulation.

4.4. Limitations. An issue requiring further investigation is the robust and automatic identification of inference failure. The approach of estimating the covariance from the Hessian, which was not positive definite and thus noninvertible to a classical covariance in this case, did not yield a robust measure of such failure. The noninvertible, nonpositive definite Hessian is a well-known issue especially in the case of nonlinear models with only partial identifiability and has been discussed in depth with various suggested approaches ranging from rethinking the model to employing Bayesian sense sampling techniques [45]. We have been unable to definitively resolve this issue so far. From our experience when attempting to sample full Bayesian posterior distributions for this model to more robustly estimate parameter uncertainty, only complex algorithmic approaches such as parallel tempering with large number of samples combined with manual tuning of the sampling covariance for each individual patient/dataset were able to generate reasonably stable posterior estimates, which of course, aside from not being amenable to full automation in the translational setting, also carry the risk of introducing subjective bias through the manual tuning process. We therefore decided not to report such preliminary results at this stage.

The advantage of robust inference failure identification is the confidence in the quality and reliability of results. Currently, haemodynamic monitoring devices that rely on complex processing algorithms may provide information on the quality of the input signal, e.g., as a signal quality index, but they are often inherently unable to give any information on the quality of the computed output. This makes such monitors a black box for the clinician, who has to use the displayed parameters for clinical decisions without information on their reliability in the current clinical situation.

In this retrospective study, independent validation measurements of the inferred β were not available. Therefore, this preliminary report can only serve to stimulate further research using prospective data that contain quantitative measurements of diastolic function, and data collected during interventions to validate our findings. External validation is also required to assess whether the inferred β values may be usable in situations of estimation failure and in SR patients, given that estimation results also approach the physiological range in this pilot study. With regard to inference methodology, the current approach using parallel tempering as a global optimisation routine is limited to relatively short stationary time series, which could be addressed by applying sequential Monte Carlo techniques [58] to allow for online estimation of time-varying

parameters by sequentially assimilating incoming measurements. For bedside use of such an approach, robust identification of model failure in the case of noisy input data is required and future work needs to address this.

A further limitation is the small number of SR patients matching the inclusion criteria, resulting in a significantly younger and healthier SR group. This, however, does not question the findings. The purpose of including an SR group in the study design was to demonstrate that the approach only works with broadband beat-to-beat variation as seen in AF, not in SR, and that its failure can clearly be identified.

4.5. Outlook and Future Work. The observation of better fits from the expanded model with reduced estimation uncertainty, along with reduced, but not eliminated systematic dependencies in residuals, suggests applying a physiologically more accurate model of left ventricular function, which includes a quantitative description of systole.

Such a more complex approach will require further investigation of sampling techniques and algorithms as the current simple model already proved challenging to estimate. We believe this to be due to the highly nonlinear underlying parameter space, which could only be effectively sampled by the PT algorithm. Sequential Monte Carlo techniques may work better if employed in a continuous tracking scenario, as is required for clinical application, but the fundamental challenge of estimation from distributions with narrow support on a curved submanifold, which appears as the primary source of the estimation difficulty, will remain.

5. Conclusion

In this study, we demonstrated for the first time that inferring diastolic ventricular stiffness, β , from routine monitoring data may be possible in ICU patients presenting with AF. This is of potentially high clinical importance for the large group of ICU patients with combined LVDD and AF because of relevant therapeutic implications. Uncertainty estimation, via local evaluation of the covariance from the Hessian, in the setting of an ill-posed, nonlinear problem did not allow for robust identification of inference failure. In order to translate the methodology to the bedside, further work with regard to robust and automated identification of inference failure and continuous parameter estimation is needed. A crucial next step will be the prospective validation of the quantitative correctness of the inferred parameter values from clinical information.

Abbreviations

HF:	Heart failure
AF:	Atrial fibrillation
LVDD:	Left ventricular dysfunction
HFpEF:	Heart failure with preserved ejection fraction
LVDF:	Left ventricular diastolic function
EDV:	End-diastolic volume
ABP:	Invasive arterial blood pressure
SR:	Sinus rhythm
RRI:	RR intervals

PP: Pulse pressure
 SM: Simple model
 EM: Expanded model
 PT: Parallel tempering
 BLV: Best (maximum) likelihood vector
 FVE: Fraction of variation explained
 SD: Standard deviation

Model Parameters

α : Aortic compliance
 β : Left ventricular diastolic stiffness
 δ : Offset factor (linear compliance)
 k_1/k_3 : Combined factors of model
 C: Factor from integration
 P_{cvp} : Left ventricular filling pressure
 P_{LV0} : Pressure scaling factor of pressure-volume equation
 R_{valve} : Mitral valve resistance
 V_{ED0} : Unstressed volume factor of pressure-volume equation.

Data Availability

The waveform data supporting this numerical analysis are from previously reported datasets, which have been cited and are freely available at PhysioNet.org. The processed input data and algorithm are available in the online supplement and upon request to PD Dr. Sven Zenker.

Conflicts of Interest

The authors declare that they have no conflicts of interest.

Authors' Contributions

Nicholas Kiefer and Maximilian J. Oremek contributed equally to this work.

Acknowledgments

Simulations were performed with computing resources granted by RWTH Aachen University under project nova0002. This work was supported in part through funding from DFG under grant ZE 904/2-1.

Supplementary Materials

Online Supplement Expanded Methods and Results: this document provides further details on methodological considerations and details about the model employed. Furthermore, the Results section includes figures of the entire cohort corresponding to those displayed in the manuscript for a selection of patients. Online Supplement Code: this is the product of the research and enables the reader to verify results and potentially apply the methodology to their data. We have a strong commitment to open sourcing the analysis code to promote transparency and reproducibility and thus further future research in this area. This supplement provides the complete analysis code and processed data for the research presented within this manuscript. Within the ZIP folder, the file "Readme.md" provides instructions for building and running the code. If additional questions or issues arise with

regard to usage of the code, do not hesitate to contact the authors. (*Supplementary Materials*)

References

- [1] M. Gheorghade, F. Zannad, G. Sopko et al., "Acute heart failure syndromes," *Circulation*, vol. 112, no. 25, pp. 3958–3968, 2005.
- [2] A. P. Ambrosy, G. C. Fonarow, J. Butler et al., "The global health and economic burden of hospitalizations for heart failure," *Journal of the American College of Cardiology*, vol. 63, no. 12, pp. 1123–1133, 2014.
- [3] M. Gheorghade, M. Vaduganathan, G. C. Fonarow, and R. O. Bonow, "Rehospitalization for heart failure," *Journal of the American College of Cardiology*, vol. 61, no. 4, pp. 391–403, 2013.
- [4] B. A. Steinberg, X. Zhao, P. A. Heidenreich et al., "Trends in patients hospitalized with heart failure and preserved left ventricular ejection fraction," *Circulation*, vol. 126, no. 1, pp. 65–75, 2012.
- [5] B. Ziaieian and G. C. Fonarow, "Epidemiology and aetiology of heart failure," *Nature Reviews Cardiology*, vol. 13, no. 6, pp. 368–378, 2016.
- [6] W. B. Kannel, "Incidence and epidemiology of heart failure," *Heart Failure Reviews*, vol. 5, no. 2, pp. 167–173, 2000.
- [7] B. M. Psaty, T. A. Manolio, L. H. Kuller et al., "Incidence of and risk factors for atrial fibrillation in older adults," *Circulation*, vol. 96, no. 7, pp. 2455–2461, 1997.
- [8] E. J. Benjamin, D. Levy, S. M. Vaziri, R. B. D'Agostino, A. J. Belanger, and P. A. Wolf, "Independent risk factors for atrial fibrillation in a population-based cohort. The Framingham Heart Study," *JAMA: The Journal of the American Medical Association*, vol. 271, no. 11, pp. 840–844, 1994.
- [9] D. Farmakis, G. Papingiotis, and J. Parissis, "Acute heart failure: epidemiology and socioeconomic burden," *Continuing Cardiology Education*, vol. 3, no. 3, pp. 88–92, 2017.
- [10] G. C. Fonarow, W. G. Stough, W. T. Abraham et al., "Characteristics, treatments, and outcomes of patients with preserved systolic function hospitalized for heart failure," *Journal of the American College of Cardiology*, vol. 50, no. 8, pp. 768–777, 2007.
- [11] T. E. Owan, D. O. Hodge, R. M. Herges, S. J. Jacobsen, V. L. Roger, and M. M. Redfield, "Trends in prevalence and outcome of heart failure with preserved ejection fraction," *New England Journal of Medicine*, vol. 355, no. 3, pp. 251–259, 2006.
- [12] P. Ponikowski, A. A. Voors, S. D. Anker et al., "2016 ESC guidelines for the diagnosis and treatment of acute and chronic heart failure," *European Heart Journal*, vol. 37, no. 27, pp. 2129–2200, 2016.
- [13] P. Kirchhof, S. Benussi, and D. Kotecha, "2016 ESC guidelines for the management of atrial fibrillation developed in collaboration with EACTS," *European Heart Journal*, vol. 37, no. 38, pp. 2893–2962, 2016.
- [14] R. G. Pai and P. Varadarajan, "Prognostic significance of atrial fibrillation is a function of left ventricular ejection fraction," *Clinical Cardiology*, vol. 30, no. 7, pp. 349–354, 2007.
- [15] D. Kotecha, C. S. P. Lam, D. J. Van Veldhuisen, I. C. Van Gelder, A. A. Voors, and M. Rienstra, "Heart failure with preserved ejection fraction and atrial fibrillation," *Journal of the American College of Cardiology*, vol. 68, no. 20, pp. 2217–2228, 2016.
- [16] U. Sartipy, U. Dahlström, M. Fu, and L. H. Lund, "Atrial fibrillation in heart failure with preserved, mid-range, and

- reduced ejection fraction,” *JACC: Heart Failure*, vol. 5, no. 8, pp. 565–574, 2017.
- [17] R. A. Vermond, B. Geelhoed, N. Verweij et al., “Incidence of atrial fibrillation and relationship with cardiovascular events, heart failure, and mortality,” *Journal of the American College of Cardiology*, vol. 66, no. 9, pp. 1000–1007, 2015.
- [18] P. Vignon, “Ventricular diastolic abnormalities in the critically ill,” *Current Opinion in Critical Care*, vol. 19, no. 3, pp. 242–249, 2013.
- [19] H. Artucio and M. Pereira, “Cardiac arrhythmias in critically ill patients,” *Critical Care Medicine*, vol. 18, no. 12, pp. 1383–1388, 1990.
- [20] L. A. Eisen, P. Davlouros, and D. Karakitsos, “Left ventricular diastolic dysfunction in the intensive care unit: trends and perspectives,” *Critical Care Research and Practice*, vol. 2012, Article ID 964158, 5 pages, 2012.
- [21] S. F. Nagueh, C. P. Appleton, T. C. Gillebert et al., “Recommendations for the evaluation of left ventricular diastolic function by echocardiography,” *European Journal of Echocardiography*, vol. 10, no. 2, pp. 165–193, 2008.
- [22] X. Bai and Q. Wang, “Time constants of cardiac function and their calculations~!2010-05-30~!2010-06-24~!2010-08-09~!,” *Open Cardiovascular Medicine Journal*, vol. 4, no. 1, pp. 168–172, 2010.
- [23] D. D. Glower, J. A. Spratt, N. D. Snow et al., “Linearity of the Frank–Starling relationship in the intact heart: the concept of preload recruitable stroke work,” *Circulation*, vol. 71, no. 5, pp. 994–1009, 1985.
- [24] A. T. Gosselink, P. K. Blanksma, H. J. G. M. Crijns et al., “Left ventricular beat-to-beat performance in atrial fibrillation: contribution of Frank–Starling mechanism after short rather than long RR intervals,” *Journal of the American College of Cardiology*, vol. 26, no. 6, pp. 1516–1521, 1995.
- [25] C. I. O. Brookes, P. A. White, M. Staples et al., “Myocardial contractility is not constant during spontaneous atrial fibrillation in patients,” *Circulation*, vol. 98, no. 17, pp. 1762–1768, 1998.
- [26] G. Clermont and S. Zenker, “The inverse problem in mathematical biology,” *Mathematical Biosciences*, vol. 260, pp. 11–15, 2015.
- [27] S. Zenker, “Parallel particle filters for online identification of mechanistic mathematical models of physiology from monitoring data: performance and real-time scalability in simulation scenarios,” *Journal of Clinical Monitoring and Computing*, vol. 24, no. 4, pp. 319–333, 2010.
- [28] S. Zenker, J. Rubin, and G. Clermont, “From inverse problems in mathematical physiology to quantitative differential diagnoses,” *PLoS Computational Biology*, vol. 3, no. 11, article e204, 2007.
- [29] A. L. Goldberger, L. A. N. Amaral, L. Glass et al., “PhysioBank, PhysioToolkit, and PhysioNet: components of a new research resource for complex physiologic signals,” *Circulation*, vol. 101, no. 23, pp. e215–e220, 2000.
- [30] J. P. Welch, P. J. Ford, R. S. Teplick, and R. M. Rubsamen, “The Massachusetts general hospital-marquette foundation hemodynamic and electrocardiographic database -- comprehensive collection of critical care waveforms,” *Journal of Clinical Monitoring*, vol. 7, no. 1, pp. 96–97, 1991.
- [31] N. M. Arzeno, Z.-D. Deng, and C.-S. Poon, “Analysis of first-derivative based QRS detection algorithms,” *IEEE Transactions on Biomedical Engineering*, vol. 55, no. 2, pp. 478–484, 2008.
- [32] W. Zong, T. Heldt, G. B. Moody, and R. G. Mark, “An open-source algorithm to detect onset of arterial blood pressure pulses,” in *Proceedings of the Computers in Cardiology Conference, 2003*, pp. 259–262, Thessaloniki, Greece, September 2003.
- [33] A. Griewank, D. Juedes, and J. Utke, “Algorithm 755; ADOL-C: a package for the automatic differentiation of algorithms written in C/C++,” *ACM Transactions on Mathematical Software*, vol. 22, no. 2, pp. 131–167, 1996.
- [34] C. Sanderson and R. Curtin, “Armadillo: a template-based C++ library for linear algebra,” *Journal of Open Source Software*, vol. 1, no. 2, p. 26, 2016.
- [35] B. Schling, *The Boost C++ Libraries*, XML Press, Durham, North Carolina, 2011.
- [36] H. Bauke and S. Mertens, “Random numbers for large-scale distributed Monte Carlo simulations,” *Physical Review E*, vol. 75, no. 6, article 066701, 2007.
- [37] Python Software Foundation, *Python Language Reference*, Network Theory Limited, Boston, MA, USA, 2003.
- [38] S. van der Walt, S. C. Colbert, and G. Varoquaux, “The NumPy array: a structure for efficient numerical computation,” *Computing in Science & Engineering*, vol. 13, no. 2, pp. 22–30, Mar. 2011.
- [39] J. D. Hunter, “Matplotlib: a 2D graphics environment,” *Computing in Science & Engineering*, vol. 9, no. 3, pp. 90–95, 2007.
- [40] W. McKinney, “Data structures for statistical computing in python,” in *Proceedings of the 9th Python in Science Conference*, vol. 445, pp. 51–56, Austin, TX, USA, 2010.
- [41] E. Jones, T. Oliphant, and P. Peterson, *SciPy: Open Source Scientific Tools for Python*, 2001.
- [42] T. Meguro, M. Akaishi, Y. Suzuki, T. Matsubara, H. Yokozuka, and S. Ogawa, “Application of mechanical restitution,” *Japanese Circulation Journal*, vol. 62, no. 11, pp. 829–836, 1998.
- [43] R. E. Edmands, K. Greenspan, and C. Fisch, “The role of inotropic variation in ventricular function during atrial fibrillation,” *Journal of Clinical Investigation*, vol. 49, no. 4, pp. 738–746, 1970.
- [44] D. J. Earl and M. W. Deem, “Parallel tempering: theory, applications, and new perspectives,” *Physical Chemistry Chemical Physics*, vol. 7, no. 23, pp. 3910–3916, 2005.
- [45] J. Gill and G. King, “What to do when your hessian is not invertible,” *Sociological Methods & Research*, vol. 33, no. 1, pp. 54–87, 2004.
- [46] H. B. Mann and D. R. Whitney, “On a test of whether one of two random variables is stochastically larger than the other,” *Annals of Mathematical Statistics*, vol. 18, no. 1, pp. 50–60, 1947.
- [47] D. A. Kass, M. Midei, J. Brinker, and W. L. Maughan, “Influence of coronary occlusion during PTCA on end-systolic and end-diastolic pressure-volume relations in humans,” *Circulation*, vol. 81, no. 2, pp. 447–460, Feb. 1990.
- [48] B. Schmitt, P. Steendijk, K. Lunze et al., “Integrated assessment of diastolic and systolic ventricular function using diagnostic cardiac magnetic resonance catheterization,” *JACC: Cardiovascular Imaging*, vol. 2, no. 11, pp. 1271–1281, 2009.
- [49] J. N. Cohn, S. Finkelstein, G. McVeigh et al., “Noninvasive pulse wave analysis for the early detection of vascular disease,” *Hypertension*, vol. 26, no. 3, pp. 503–508, 1995.
- [50] D. Duprez, M. L. De Buyzere, E. R. Rietzschel et al., “Inverse relationship between aldosterone and large artery compliance in chronically treated heart failure patients,” *European Heart Journal*, vol. 19, no. 9, pp. 1371–1376, 1998.

- [51] Z. R. Liu, C. T. Ting, S. X. Zhu, and F. C. Yin, "Aortic compliance in human hypertension," *Hypertension*, vol. 14, no. 2, pp. 129–136, 1989.
- [52] G. E. McVeigh, C. W. Bratteli, and D. J. Morgan, "Age-related abnormalities in arterial compliance identified by pressure pulse contour analysis: aging and arterial compliance," *Hypertension*, vol. 33, no. 6, pp. 1392–1398, 1999.
- [53] M. W. Dünser and W. R. Hasibeder, "Sympathetic overstimulation during critical illness: adverse effects of adrenergic stress," *Journal of Intensive Care Medicine*, vol. 24, no. 5, pp. 293–316, 2009.
- [54] V. Malik, A. Subramanian, M. Hote, and U. Kiran, "Effect of levosimendan on diastolic function in patients undergoing coronary artery bypass grafting," *Journal of Cardiovascular Pharmacology*, vol. 66, no. 2, pp. 141–147, 2015.
- [55] B. Axelsson, M. Arbeus, A. Magnuson, and J. Hultman, "Milrinone improves diastolic function in coronary artery bypass surgery as assessed by acoustic quantification and peak filling rate: a prospective randomized study," *Journal of Cardiothoracic and Vascular Anesthesia*, vol. 24, no. 2, pp. 244–249, 2010.
- [56] C. A. Albrecht, G. M. Giesler, B. Kar, R. Hariharan, and R. M. Delgado, "Intravenous milrinone infusion improves congestive heart failure caused by diastolic dysfunction: a brief case series," *Texas Heart Institute Journal*, vol. 32, no. 2, pp. 220–223, 2005.
- [57] C. A. de M. Almeida, W. L. Nedel, V. D. Morais, M. M. Boniatti, and O. C. de Almeida-Filho, "Diastolic dysfunction as a predictor of weaning failure: a systematic review and meta-analysis," *Journal of Critical Care*, vol. 34, pp. 135–141, 2016.
- [58] A. Doucet, N. de Freitas, and N. Gordon, "An introduction to sequential Monte Carlo methods," in *Sequential Monte Carlo Methods and Particle Filters Resources*, A. Doucet, N. de Freitas, and N. Gordon, Eds., pp. 3–14, Springer, New York, NY, USA, 2001.

Research Article

Arrhythmia Classification of ECG Signals Using Hybrid Features

Syed Muhammad Anwar ¹, Maheen Gul ², Muhammad Majid ²,
and Majdi Alnowami ³

¹Department of Software Engineering, University of Engineering and Technology, Taxila, Pakistan

²Department of Computer Engineering, University of Engineering and Technology, Taxila, Pakistan

³Department of Nuclear Engineering, King Abdulaziz University, Jeddah, Saudi Arabia

Correspondence should be addressed to Syed Muhammad Anwar; s.anwar@uettaxila.edu.pk

Received 17 August 2018; Accepted 15 October 2018; Published 12 November 2018

Guest Editor: Dominique J. Monlezun

Copyright © 2018 Syed Muhammad Anwar et al. This is an open access article distributed under the Creative Commons Attribution License, which permits unrestricted use, distribution, and reproduction in any medium, provided the original work is properly cited.

Automatic detection and classification of life-threatening arrhythmia plays an important part in dealing with various cardiac conditions. In this paper, a novel method for classification of various types of arrhythmia using morphological and dynamic features is presented. Discrete wavelet transform (DWT) is applied on each heart beat to obtain the morphological features. It provides better time and frequency resolution of the electrocardiogram (ECG) signal, which helps in decoding important information of a quasiperiodic ECG using variable window sizes. RR interval information is used as a dynamic feature. The nonlinear dynamics of RR interval are captured using Teager energy operator, which improves the arrhythmia classification. Moreover, to remove redundancy, DWT subbands are subjected to dimensionality reduction using independent component analysis, and a total of twelve coefficients are selected as morphological features. These hybrid features are combined and fed to a neural network to classify arrhythmia. The proposed algorithm has been tested over MIT-BIH arrhythmia database using 13724 beats and MIT-BIH supraventricular arrhythmia database using 22151 beats. The proposed methodology resulted in an improved average accuracy of 99.75% and 99.84% for class- and subject-oriented scheme, respectively, using three-fold cross validation.

1. Introduction

Cardiac arrhythmias are a type of irregular heartbeats in which the heart rhythm is either too fast (tachycardia) or too slow (bradycardia). A small change in electrocardiogram (ECG) morphology or dynamics may lead to severe arrhythmia attacks, which can reduce the ability of the heart to pump blood and causes shorting of breath, pain in chest, tiredness, and loss of consciousness. There are several types of arrhythmia, and some of these are dangerous which may lead to cardiac arrest and sudden death if not detected and monitored in time [1]. There are other types of arrhythmias which are not essentially life-threatening, but still require proper analysis to avoid future clinical problems. A few categories of arrhythmia appear infrequently in the ECG signal and hence require long electrocardiogram recordings in order to be detected. A manual analysis of longer ECG recordings requires time and great effort. The automatic

detection and classification of these arrhythmias offer great assistance to physicians [2, 3]. Moreover, early diagnosis of arrhythmias would help in proper treatment and support sustained life. Therefore, several techniques have been proposed for automatic detection and classification of various types of arrhythmia [4–10].

A method for classification of sixteen types of arrhythmia based on ECG morphology and dynamics was proposed in [11]. Morphological features were extracted using discrete wavelet transform (DWT) and independent component analysis (ICA), while ECG dynamic features were extracted by calculating RR interval. These features were then classified using support vector machine with an average accuracy of 99.6%. Five types of heartbeats, namely, normal, premature ventricular contractions (PVC), atrial premature contractions (APC), left bundle branch block (LBBB), and right bundle branch block (RBBB) were recognized in [4]. Stationary wavelet transform (SWT) was

applied on each ECG signal to make it noise free. The high-order statistics of ECG signals and three timing intervals were considered as features, which were then fed to a hybrid bees algorithm for training the radial basis function and resulted in an average accuracy of 95.18%.

Some techniques rely on fiducial features, which are temporal and dynamic features that directly depend upon the ECG characteristics, e.g., wave onset point, peaks (maxima/minima), and offset [5]. Nonfiducial features that are directly derived from the fiducial features or obtained by segmenting the ECG signal into several parts have also been used [6]. These features are not found good enough when used independently for accurate classification of ECG arrhythmia. A combination of both fiducial and nonfiducial features was used for defining a biological marker for person identification [7, 12].

The extracted features have usually been analyzed either in time domain or frequency domain. Some of the most important time domain features, including RR interval, ST segment, and T height, require identification of key time points within the signal [13]. An approach for heartbeat classification with dynamic rejection thresholds was proposed using QRS morphology, frequency information, AC power of QRS detail coefficients, and RR intervals as features to represent ECG beats [8]. A support vector machine (SVM) was used to classify with an improved accuracy of 97.2% and minimum rejection cost. A combination of time and frequency information has also been used in [9, 11, 14–16], giving better extraction of information from a quasiperiodic ECG signal using wavelet transform, which provides a good time and frequency resolution. Five important types of arrhythmia, namely, nonectopic, ventricular ectopic, supraventricular ectopic, unclassifiable beats, and fusion beats, were analyzed and detected in [9]. Features were extracted using DWT, and only significant coefficients were selected by applying independent component analysis which in combination with neural network yielded an accuracy of 99.28%.

All methods discussed above have the following shortcomings:

- (1) Performances of most of the methods have been tested only on smaller data sets, and there is a need to verify their performance on larger databases
- (2) Selected classes of arrhythmia have been evaluated, and there is a need to test all arrhythmia classes
- (3) The classification accuracy on sparsely occurring arrhythmia classes is not good

In this paper, a novel technique for ECG beat classification of arrhythmia is proposed that considers a hybrid of enhanced morphological and dynamic features to overcome these shortcomings. Morphological features are obtained using DWT on each heartbeat. The resulting features consist of DWT approximation coefficient and detail coefficients at level 4. Independent component analysis is applied on both approximation and detail coefficients independently to extract only important coefficients. In addition, four types of RR interval features are calculated to represent the dynamic

features of ECG heartbeats. Moreover, to enhance the dynamic features of ECG heartbeats corrupted with Gaussian noise, Teager energy operator (TEO) [17] is used. All these features are combined and fed to a neural network (NN) for automatic classification of heartbeats into different arrhythmia types according to both class-oriented scheme (18 classes) and subject-oriented scheme (5 classes).

The rest of the paper is organized as follows. Firstly, the proposed methodology is explained in detail in Section 2. Class- and subject-oriented evaluation of the proposed system is presented in Section 3, followed by conclusion in Section 4.

2. Methodology

The proposed methodology is presented in Figure 1, which consists of four major phases, namely, preprocessing, heartbeat segmentation, feature extraction, and feature classification. The details of these phases are presented in the following subsections.

2.1. ECG Signal Preprocessing. Mostly ECG signals are affected by baseline wander or power line interface (PLI). Different methods were introduced to remove these types of noises from the ECG signal [18]. Experiments showed that baseline wander significantly affects the detection of arrhythmia and makes the ECG signal analysis difficult for an expert [19]. PLI is a type of noise that occurs due to broken electrodes, offset voltages in the electrodes, movement of patient, respiration errors, or electrode resistance while recording the ECG signal. It is a low frequency noise and typically exists in the frequency range of 0–0.3 Hz. For baseline wander removal, the expected value of the signal was subtracted from the raw ECG signal to obtain the noise-free ECG signal using

$$x[n] = x_r[n] - \mu, \quad (1)$$

where $x[n]$ is the denoised signal, $x_r[n]$ represents the raw ECG signal, and μ is the expected value of the raw EEG signal.

2.2. Heartbeat Segmentation. Three basic constituents of a heart cycle are QRS complex, T wave, and P wave, termed as fiducial points. The correct splitting of the ECG signal into heartbeat segments involves recognition of borders and peak locations of these fiducial points. The information about the R-peak locations given in the dataset was used to obtain these heartbeat segments. A single heartbeat consisted of 200 samples including the R-peak and the samples around the peak. This segment size contained maximum information of a single heartbeat and is shown in Figure 2.

2.3. Feature Extraction. In feature extraction, improved features based on DWT, RR interval, and Teager energy operator were selected, which were able to represent the morphological and dynamic changes in the ECG signal with more significance.

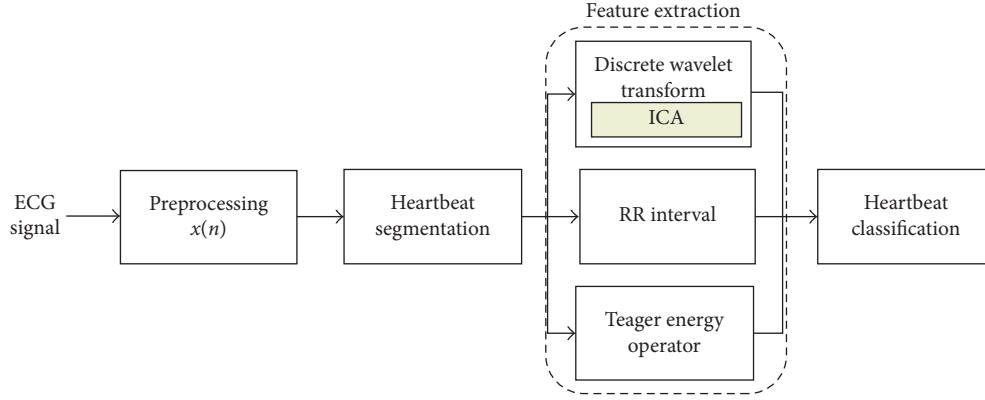


FIGURE 1: Block diagram of the proposed arrhythmia classification scheme using hybrid features.

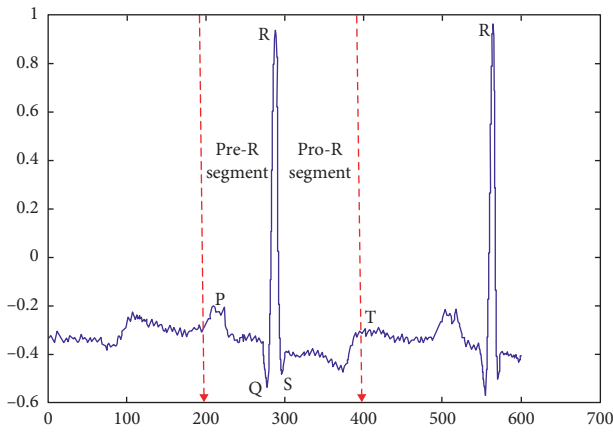


FIGURE 2: Heartbeat segmentation of ECG signal from MITDB database.

2.3.1. Discrete Wavelet Transform (DWT). Statistical features of biomedical signals usually change over position or time. Wavelet transform offers signal representation in both time and frequency domains, which makes it capable for analyzing quasiperiodic signals like ECG. Wavelet transform was employed in processing of the ECG signals for feature extraction [1], denoising [11], and heartbeat recognition [20]. In the proposed method, DWT was used as a feature extraction technique. After applying DWT, the ECG signal decomposed into low-frequency approximation components and high-frequency detail components.

The most commonly used wavelets which provide orthogonality properties are Daubechies, Coiflets, Symlets, and Discrete Meyer [21]. Each heartbeat was disintegrated using the finite impulse response (FIR) approximation of the Discrete Mayers wavelet transform. The frequency range of fourth-level approximation subband was 011.25 Hz, and the frequency range for fourth level detail subband was 11.2522.5 Hz. A total of 200 coefficients were extracted as wavelet features, which were processed using ICA for dimensionality reduction. Six major ICA components were selected from each of the two DWT subbands, resulting in a total of twelve morphological features from the two subbands.

2.3.2. RR Interval Features. R is a point corresponding to the highest peak of the ECG waveform, and RR interval is the time between the successive QRS complexes. The ECG signal has a nonlinear dynamic behavior, and during arrhythmia, nonlinear dynamic components change more significantly than the linear counterparts. RR interval is simple, easy to calculate, and less prone to noise. Four types of RR interval features, namely, previous-RR, post-RR, average-RR, and local-RR interval, were derived from the RR sequence, to characterize the dynamic features of the heartbeat. The calculation of these features uses the following equations:

$$RR_{pre}(i) = R(i) - R(i-1),$$

$$RR_{post}(i) = R(i+1) - R(i),$$

$$RR_{local} = \frac{1}{10} \sum_{i=-5}^5 RR(i), \quad (2)$$

$$RR_{ave} = \frac{1}{N_{RR}} \sum_{i=1}^{N_{RR}} RR(i),$$

where i shows the location of the current R-peak and RR_{pre} , RR_{post} , RR_{local} , and RR_{ave} represent the previous, post, local, and average RR interval, respectively. $R(i)$ is the current R-peak, $R(i-1)$ and $R(i+1)$ represent the previous and post R-peaks, respectively, and N_{RR} shows the total number of RR intervals in an ECG segment.

2.3.3. Teager Energy Operator (TEO). An independent analysis of RR interval does not capture the nonlinear nature of RR interval inconsistency. TEO was utilized to represent the nonlinear behavior of the RR interval, which is a nonlinear operator for energy tracking [17]. It measures the instantaneous frequency, amplitude envelope, and the energy of the system that generated the signal. The energy required by a source to generate signals with different frequencies and same energy and amplitude would be different. More energy is needed to generate a high-frequency signal as compared with a low-frequency signal. TEO reflects the source energy; hence, any instability in the conduction path and impulse generation gets revealed in the Teager energy

function. For a discrete time signal $x[n]$, the Teager–Kaiser nonlinear energy (NE) and the average nonlinear energy (ANE) in the time domain are given as

$$\text{NE}\{x[n]\} = x^2[n] - x[n-1]x[n+1], \quad (3)$$

$$\text{ANE} = \frac{1}{N} \sum \text{NE}\{x[n]\}, \quad (4)$$

where N represents the total number of samples in ECG heartbeat.

2.4. Neural Network (NN) Classifier. An artificial neural network consists of interconnected neurons which send and receive messages between each other. These interconnections are assigned weights, which represent a network state and are updated during the learning process. A feedforward neural network with 10 hidden layers was used for the classification of arrhythmia in this study. The network was implemented on MATLAB R2013a. The number of neurons in each hidden layer was limited to 50, which allowed training this network on a core-i5 CPU-based system with a RAM of 8 GB. An activation function based on rectified linear unit (ReLU) was used for the hidden layers, and a sigmoid function was used at the output layer. Back propagation with stochastic gradient decay was used for updating the network weights. The learning rate was optimized to a value of 0.63, using grid search for accuracy and to avoid over fitting.

3. Experimental Results

The details of the dataset used and the experimental results are presented in the following subsections.

3.1. Dataset. The MIT-BIH arrhythmia database (MITDB) [22] and MIT-BIH supraventricular arrhythmia database (SVDB) [23] from physionet were used for evaluation of the performance of the proposed algorithm. The MITDB includes 48 ECG recordings of 47 subjects, whereas the SVDB contains 78 half-hour ECG recordings. The data in SVDB were recorded to increase the supraventricular arrhythmias examples in MITDB. The databases contain an annotation file with locations of the “QRS” complex and the type of the heartbeat for each record. These class annotations for heartbeats were exploited as reference annotations for evaluation purpose of the proposed model.

3.2. Evaluation Strategy. Two different types of evaluation strategies were considered, namely, class-oriented [24] and subject-oriented [9]. In class-oriented strategy, all signals from both databases were segmented down using already annotated QRS locations. The resulting segments were divided into 18 different types of beats, namely, normal beat (NOR “N”), atrial premature contraction (APC “A”), fusion of ventricular and normal beat (FVN “F”), left bundle branch block (LBBB “L”), unclassifiable beat (UN “Q”), premature ventricular contraction (PVC “V”), right bundle branch

block beat (RBBB “R”), ventricular flutter wave (VF “!”), atrial escape beat (AE “e”), fusion of paced and normal beat (FPN “f”), nodal (junctional) premature beat (NP “J”), isolated QRS-like artifact (—), aberrated atrial premature beat (AP “a”), ventricular escape beat (VE “E”), nodal (junctional) escape beat (NE “j”), nonconducted P-wave (blocked APB “x”), paced beat (PACE “/”), and supraventricular premature beat (SP “S”).

In addition, subject-oriented strategy was also evaluated. All 126 records from both the datasets were divided into a similar training and testing ratio as for the class-oriented scheme, but performance was reported according to ANSI/AAMI EC57:1998 standard [25]. The original 18 classes of heartbeats were grouped into five bigger classes, namely, nonectopic beats (N), ventricular ectopic beat (V), supraventricular ectopic beat (S), unknown beat (Q), and fusion beat (F). The mapping from the MITDB and SVDB classes to the ANSI/AAMI heartbeat classes is presented in Table 1.

The ECG signal from MITDB and SVDB datasets are first denoised to remove baseline wander. The denoised signal was segmented into different heartbeats of same length (200 samples each) by using R-peak location information in the given annotations. In total, 35875 beats from both databases (13724 from MIT-BIH arrhythmia dataset and 22151 beats from MIT-BIH supraventricular arrhythmia dataset) were considered. FIR approximation of Mayers wavelet was applied on each heartbeat segment. ICA was applied on the resulting 4th level approximation and 4th level detail coefficients independently to remove the redundancy between feature coefficients. In addition, dynamic features of the ECG signal were represented by four types of RR interval features, and Teager energy operator was used to represent the nonlinear dynamics of the ECG signal.

A 3-fold cross-validation method was used for training and testing of the classifier. The complete dataset (35,875 beats) was subsampled into two sets, one having 70% of the total samples and the other with the remaining heartbeats from each of the classes (50% data was selected for training from atrial escape beat (e), due to very low number of beats). 70% of total heartbeats were utilized for training purpose, and the rest of the heartbeats were used in testing and evaluation of the performance of the classifier. The process was repeated three times with different heartbeats used for training and testing. The average results of the three folds were calculated to assess the general performance of the proposed method. Sensitivity (Se), specificity (Sp), positive predictive value (PPV), and accuracy (Acc) were calculated to analyze the performance.

3.2.1. Class-Oriented Evaluation. In class-oriented evaluation scheme, a neural network was trained to predict the class of test heartbeats among 18 different classes of arrhythmia. The specificity, sensitivity, and PPV of each individual class are summarized in Table 2, which shows that the proposed approach demonstrates a reasonable individual-class performance, showing greater specificity, good sensitivity, and PPV. Moreover, it has given better results on classes whose

TABLE 1: Mapping from MIT-BIH arrhythmia database (MITDB)/supraventricular arrhythmia database (SVDB) heartbeat classes to ANSI/AAMI heartbeat classes.

AAMI classes	MITDB/SVDB classes	Total
Nonectopic beat (N)	NOR, LBBB, RBBB, AE, NE	30929
Supraventricular ectopic beat (S)	APC, AP, APB, NP, SP	1538
Ventricular ectopic beat (V)	PVC, VE, VF	2035
Fusion beat (F)	F	14
Unknown beat (Q)	UN, FPN, PACE,	1329

TABLE 2: A summary of performance analysis of the proposed method on each arrhythmia class in the “class-oriented” scheme.

Heartbeat type	Fold I				Fold II				Fold III				Average			
	Sp	Se	PPV	Acc	Sp	Se	PPV	Acc	Sp	Se	PPV	Acc	Sp	Se	PPV	Acc
Normal beat (NOR)	100	100	99.8	99.4	100	100	99.9	99.7	99.8	100	99.7	99.7	99.9	100	99.8	99.6
Atrial premature contraction	100	97	100	100	100	96.5	100	100	100	97.5	100	100	100	97	100	100
Fusion of ventricular and normal beat	100	100	100	100	100	100	100	92.7	100	100	100	100	100	100	100	97.5
Left bundle branch block (LBBB)	100	97.5	100	100	100	97	100	99.3	100	96.5	100	100	100	97	100	99.7
Unclassifiable beat (UN)	100	100	100	100	100	100	100	100	100	100	100	100	100	100	100	100
Right bundle branch block beat (RBBB)	99.8	99.4	99.4	99.7	99.9	99.2	99.4	99.4	99.9	99.3	99.4	99.4	99.8	99.3	99.4	99.5
Premature ventricular contraction (PVC)	100	99.1	99.6	99.7	100	99.2	99.6	99.5	100	99.3	99.6	99.6	100	99.2	99.6	99.6
Ventricular flutter wave (VF)	100	100	100	100	100	100	100	100	100	100	100	100	100	100	100	100
Aberrated atrial premature beat (AP)	100	100	100	100	100	100	100	100	100	100	100	100	100	100	100	100
Nodal (junctional) premature beat (NP)	100	92.6	100	100	100	92.8	100	100	100	92.7	100	100	100	92.8	100	100
Atrial escape beat (AE)	100	100	100	100	100	100	100	100	100	100	100	100	100	100	100	100
Fusion of paced and normal beat (FPN)	100	100	100	100	99.9	100	100	100	100	100	100	100	100	100	100	100
Isolated QRS-like artifact (Iso)	99.9	100	97.2	100	99.9	100	98.1	100	99.9	99.1	99.1	99.1	99.9	98.1	98.1	99.5
Ventricular escape beat (VE)	100	100	100	100	99.9	100	95.2	100	99.9	100	98.5	100	100	95.2	100	100
Nodal (junctional) escape beat	99.9	100	95	100	99.9	100	97.5	100	100	100	100	100	100	100	100	100
Paced beat (PACE)	99.9	100	99.2	100	100	100	100	100	99.9	100	99.6	100	100	99.2	100	100
Nonconducted P-wave (blocked APB)	100	100	100	100	100	100	100	100	100	100	100	100	100	100	100	100
Supraventricular premature beat (SP)	100	100	100	100	100	100	100	100	100	100	100	100	100	99.4	100	100
Average	99.9	99.9	99.4	99.9	99.9	99.3	99.4	99.3	99.9	99.9	99.8	99.9	99.9	98.7	99.8	99.75

presence was low like “Q,” “e,” and “x.” The performance evaluation measures are shown for all three folds in Table 2, where the best accuracy achieved was 99.9%. In addition, 98.7% average sensitivity, 99.9% average specificity, 99.8% average PPV, and 99.75% overall accuracy were achieved. The confusion matrix is presented in Table 3, which shows the correctly classified and misclassified arrhythmia classes.

A comparison of the classification accuracy of the proposed approach and state-of-the-art methods based on class-oriented strategy is presented in Table 4. An improvement in accuracy with increased number of classes and reduced feature dimension is observed. In addition, other performance parameters such as sensitivity, specificity, and PPV have also shown improvement. These results depict that the proposed method is more generalized and computationally efficient for arrhythmia classification. An assessment based solely on “class-oriented” scheme is not a faithful measure for the performance analysis of a real-time heartbeat classification system. The performance of the subject-oriented scheme is also analyzed for practical evaluation.

3.2.2. Subject-Oriented Evaluation. In subject-oriented scheme, results have reported according to the ANSI/AAMI standard. The specificity, sensitivity, PPV and

accuracy of each individual class in ANSI/AAMI standard is shown in Table 5. The hybrid feature approach demonstrated reasonable individual-class performances, showing greater specificity, good sensitivity, positive PPV, and accuracy for all classes. The fusion beats showed lower PPV in Fold II, which can be attributed to smaller number of beats in this class. The peak accuracy achieved was 99.9% with 99.7% average sensitivity, 99.9% average specificity, 99.1% of average PPV, and 99.8% average accuracy. Table 6 shows the confusion matrix depicting an improved performance on all classes with an average accuracy of 99.8%. A comparative analysis is presented in Table 7 with state-of-the-art techniques for subject-oriented classification. A significant improvement is observed, when taking this fact into account that 18 arrhythmia classes were classified. The comparison is reported for methods using the MIT-BIH data for adding credence to the results.

4. Conclusion

In this paper, a new technique for automatic heartbeat classification of all types of arrhythmia was presented. An improved hybrid feature representation of heartbeat segments was used based on a mixture of a set of derived morphological and dynamic features. The classification was done using twelve ICA projection coefficients computed

TABLE 3: Confusion matrix for the proposed method using a neural network based classifier (class-oriented scheme).

Predicted labels	N	A	F	L	Q	R	V	!	a	J	E	f	—	E	J	/	X	S
<i>Actual labels</i>																		
N	8656	0	0	0	0	0	0	0	0	0	0	0	0	0	0	0	0	0
A	2	65	0	0	0	0	0	0	0	0	0	0	0	0	0	0	0	0
F	0	0	14	0	0	0	0	0	0	0	0	0	0	0	0	0	0	0
L	8	0	0	260	0	0	0	0	0	0	0	0	0	0	0	0	0	0
Q	0	0	0	0	5	0	0	0	0	0	0	0	0	0	0	0	0	0
R	2	0	0	0	0	314	0	0	0	0	0	0	0	0	0	0	0	0
V	4	0	0	0	0	0	564	0	0	0	0	0	0	0	0	0	0	0
!	0	0	0	0	0	0	0	21	0	0	0	0	0	0	0	0	0	0
a	0	0	0	0	0	0	0	0	1	0	0	0	0	0	0	0	0	0
J	1	0	0	0	0	0	0	0	0	13	0	0	0	0	0	0	0	0
e	0	0	0	0	0	0	0	0	0	0	1	0	0	0	0	0	0	0
f	0	0	0	0	0	0	0	0	0	0	0	33	0	0	0	0	0	0
—	0	0	0	0	0	2	0	0	0	0	0	0	105	0	0	0	0	0
E	1	0	0	0	0	0	0	0	0	0	0	0	0	20	0	0	0	0
j	0	0	0	0	0	0	0	0	0	0	0	0	0	0	40	0	0	0
/	0	0	0	0	0	0	0	0	0	0	0	0	2	0	0	254	0	0
x	0	0	0	0	0	0	0	0	0	0	0	0	0	0	0	0	2	0
S	0	0	0	0	0	0	2	0	0	0	0	0	0	0	0	0	0	376

TABLE 4: Comparison of the proposed scheme with state-of-the-art methods using class-oriented scheme.

	Features	Dimension	Classes	Accuracy	Sensitivity	Specificity	PPV
<i>Proposed</i>	<i>DWT + RR + TEO</i>	17	18	99.75	98.7	99.9	99.8
Zidelmal et al. [8]	Frequency content + RR + QRS	13	2	97.2	99	—	—
Ye et al. [11]	WT + ICA + RR	18	16	99.3	91.3	—	—
Ebrahimzadeh et al. [4]	HOS + timing interval	24	5	95.18	95.61	98.8	90.6
Pathoumvanh et al. [24]	DCT	5	5	99.11	97.01	99.44	—
Rabee and Barhumi [26]	Multi resolution WT	251	14	99.2	96.2	100	—
Alajlan et al. [27]	HOS of 2nd-order-cumulant	604	2	94.96	92.19	95.19	—
de Oliveira et al. [14]	Waveform + RR	—	2	95	95	99.87	98
Li et al. [19]	Timing interval + waveform amplitude	—	2	98.2	93.1	—	81.4

TABLE 5: Performance of the proposed method on each arrhythmia class in the “subject-oriented” scheme.

Heartbeat type	Fold I				Fold II				Fold III				Average			
	Sp	Se	PPV	Acc	Sp	Se	PPV	Acc	Sp	Se	PPV	Acc	Sp	Se	PPV	Acc
Nonectopic beats (N)	99.9	100	94.2	100	99.7	99.9	99.8	99.9	100	100	99.8	100	99.9	99.9	97.9	99.9
Supraventricular ectopic beats (S)	100	99.8	100	100	99.9	100	99.8	100	100	99.9	100	100	99.9	99.9	99.6	99.9
Ventricular ectopic beats (V)	100	99.6	100	100	100	99.5	100	99.9	100	99.7	100	100	100	99.6	100	99.9
Fusion beats (F)	99.9	100	99.9	100	99.9	100	92.8	98.9	99.9	100	100	100	99.9	100	97.6	99.6
Unclassifiable beats (Q)	100	99.6	100	99.8	100	99.4	100	100	100	99.5	100	99.7	100	99.5	100	99.8
Average	99.9	99.8	98.8	99.9	99.9	99.7	99.6	97.7	99.9	99.8	99.9	99.9	99.9	99.7	99.1	99.8

TABLE 6: Confusion matrix for Fold II using NN (subject-oriented scheme).

Predicted labels	N	S	V	F	Q
<i>Actual labels</i>					
N	9280	1	0	0	0
S	1	458	0	1	0
V	2	0	604	0	0
F	0	0	0	14	0
Q	2	0	0	0	398

from the DWT features, plus four RR interval features, and Teager energy value. Two types of evaluation schemes, class- and subject-oriented, were implemented for analyzing the system. On the standard benchmark of MIT-BIH arrhythmia database and MIT-BIH supraventricular arrhythmia database, an average accuracy of 99.75% with a peak accuracy in a single fold of 99.9% in the class-oriented evaluation was achieved. An accuracy of 99.8% in the subject-oriented evaluation was achieved. In future, an automatic patient customization scheme will be considered, allowing

TABLE 7: Comparison of the proposed scheme with state-of-the-art methods using subject-oriented scheme.

	Features	Dimensions	Classes	Accuracy	Sensitivity	Specificity
<i>Proposed</i>	<i>DWT + RR interval + TEO</i>	17	5 (18)	99.8	99.7	99.9
Ye et al. [11]	WT + ICA + RR	18	5 (16)	86.4	91.3	—
Martis et al. [9]	DWT + ICA	12	5 (15)	99.28	97.97	99.83
Mar et al. [15]	RR interval series and WT	—	3	93	80	82
de Lannoy et al. [5]	Waveform + HOS + RR	249	5 (16)	94	—	—

the heartbeat classification method to be able to adjust to individual physiological features using wearable sensors.

Data Availability

The data used in this study are available for download at the physionet MIT-BIH website.

Conflicts of Interest

The authors declare that there are no conflicts of interest regarding the publication of this paper.

Authors' Contributions

Syed Muhammad Anwar and Maheen Gul contributed equally to the study.

References

- [1] H. V. Huikuri, A. Castellanos, and R. J. Myerburg, "Sudden death due to cardiac arrhythmias," *New England Journal of Medicine*, vol. 345, no. 20, pp. 1473–1482, 2001.
- [2] P. de Chazal and R. B. Reilly, "A patient-adapting heartbeat classifier using ECG morphology and heartbeat interval features," *IEEE Transactions on Biomedical Engineering*, vol. 53, no. 12, pp. 2535–2543, 2006.
- [3] A. Mustaqeem, S. M. Anwar, M. Majid, and A. R. Khan, "Wrapper method for feature selection to classify cardiac arrhythmia," in *Proceedings of 39th Annual International Conference of the IEEE Engineering in Medicine and Biology Society (EMBC)*, pp. 3656–3659, IEEE, Jeju Island, South Korea, July 2017.
- [4] A. Ebrahimzadeh, B. Shakiba, and A. Khazaei, "Detection of electrocardiogram signals using an efficient method," *Applied Soft Computing*, vol. 22, pp. 108–117, 2014.
- [5] G. de Lannoy, D. François, J. Delbeke, and M. Verleysen, "Weighted conditional random fields for supervised inter-patient heartbeat classification," *IEEE Transactions on Biomedical Engineering*, vol. 59, no. 1, pp. 241–247, 2012.
- [6] S. Pongponsri and X.-H. Yu, "An adaptive filtering approach for electrocardiogram (ECG) signal noise reduction using neural networks," *Neurocomputing*, vol. 117, pp. 206–213, 2013.
- [7] E. J. d. S. Luz, D. Menotti, and W. R. Schwartz, "Evaluating the use of ECG signal in low frequencies as a biometry," *Expert Systems with Applications*, vol. 41, no. 5, pp. 2309–2315, 2014.
- [8] Z. Zidelmal, A. Amirou, D. Ould-Abdeslam, and J. Merckle, "ECG beat classification using a cost sensitive classifier," *Computer Methods and Programs in Biomedicine*, vol. 111, no. 3, pp. 570–577, 2013.
- [9] R. J. Martis, U. R. Acharya, and L. C. Min, "ECG beat classification using PCA, LDA, ICA and discrete wavelet transform," *Biomedical Signal Processing and Control*, vol. 8, no. 5, pp. 437–448, 2013.
- [10] A. Mustaqeem, S. M. Anwar, and M. Majid, "Multiclass classification of cardiac arrhythmia using improved feature selection and SVM invariants," *Computational and Mathematical Methods in Medicine*, vol. 2018, Article ID 7310496, 10 pages, 2018.
- [11] C. Ye, B. V. Kumar, and M. T. Coimbra, "Heartbeat classification using morphological and dynamic features of ECG signals," *IEEE Transactions on Biomedical Engineering*, vol. 59, no. 10, pp. 2930–2941, 2012.
- [12] M. Abo-Zahhad, S. M. Ahmed, and S. N. Abbas, "Biometric authentication based on PCG and ECG signals: present status and future directions," *Signal, Image and Video Processing*, vol. 8, no. 4, pp. 739–751, 2014.
- [13] E. Ullah, A. D. Bakhshi, M. Majid, and S. Bashir, "Empirical mode decomposition for improved least square t-wave alternans estimation," in *Proceedings of 15th International Bhurban Conference on Applied Sciences and Technology (IBCAST)*, pp. 334–338, IEEE, Islamabad, Pakistan, January 2018.
- [14] L. S. de Oliveira, R. V. Andreão, and M. Sarcinelli-Filho, "Premature ventricular beat classification using a dynamic bayesian network," in *Proceedings of Annual International Conference of the IEEE Engineering in Medicine and Biology Society, EMBC*, pp. 4984–4987, IEEE, Boston, MA, USA, August–September 2011.
- [15] T. Mar, S. Zauneder, J. P. Martínez, M. Llamedo, and R. Poll, "Optimization of ECG classification by means of feature selection," *IEEE Transactions on Biomedical Engineering*, vol. 58, no. 8, pp. 2168–2177, 2011.
- [16] M. M. Tantawi, K. Revett, A.-B. Salem, and M. F. Tolba, "A wavelet feature extraction method for electrocardiogram (ECG)-based biometric recognition," *Signal, Image and Video Processing*, vol. 9, no. 6, pp. 1271–1280, 2015.
- [17] F. Jabloun, A. E. Cetin, and E. Erzin, "Teager energy based feature parameters for speech recognition in car noise," *IEEE Signal Processing Letters*, vol. 6, no. 10, pp. 259–261, 1999.
- [18] S. Khan, S. M. Anwar, W. Abbas, and R. Qureshi, "A novel adaptive algorithm for removal of power line interference from ECG signal," *Science International*, vol. 28, no. 1, pp. 139–143, 2016.
- [19] P. Li, C. Liu, X. Wang, D. Zheng, Y. Li, and C. Liu, "A low-complexity data-adaptive approach for premature ventricular contraction recognition, signal," *Image and Video Processing*, vol. 8, no. 1, pp. 111–120, 2014.
- [20] S. Kadambe, R. Murray, and G. F. Boudreaux-Bartels, "Wavelet transform-based QRS complex detector," *IEEE Transactions on Biomedical Engineering*, vol. 46, no. 7, pp. 838–848, 1999.
- [21] P. S. Addison, "Wavelet transforms and the ECG: a review," *Physiological Measurement*, vol. 26, no. 5, p. R155, 2005.
- [22] G. B. Moody and R. G. Mark, "The MIT-BIH arrhythmia database on cd-rom and software for use with it," in

- Proceedings of Computers in Cardiology 1990*, pp. 185–188, IEEE, Chicago, IL, USA, 1990.
- [23] A. L. Goldberger, L. A. Amaral, L. Glass et al., “Physiobank, physiotoolkit, and physionet,” *Circulation*, vol. 101, no. 23, pp. e215–e220, 2000.
 - [24] S. Pathoumvanh, K. Hamamoto, and P. Indahak, “Arrhythmias detection and classification base on single beat ECG analysis,” in *Proceedings of 4th Joint International Conference on Information and Communication Technology, Electronic and Electrical Engineering (JICTEE)*, pp. 1–4, IEEE, Chiang Rai, Thailand, March 2014.
 - [25] Association for the Advancement of Medical Instrumentation and others, Testing and reporting performance results of cardiac rhythm and st segment measurement algorithms, *ANSI/AAMI EC38*, vol. 1998, 1998.
 - [26] A. Rabee and I. Barhumi, “ECG signal classification using support vector machine based on wavelet multiresolution analysis,” in *Proceedings of 11th International Conference on Information Science, Signal Processing and their Applications (ISSPA)*, pp. 1319–1323, IEEE, Montreal, Canada, July 2012.
 - [27] N. Alajlan, Y. Bazi, F. Melgani, S. Malek, and M. A. Bencherif, “Detection of premature ventricular contraction arrhythmias in electrocardiogram signals with kernel methods,” *Signal, Image and Video Processing*, vol. 8, no. 5, pp. 931–942, 2014.

Research Article

Biomechanical Aspects of Closing Approaches in Postcarotid Endarterectomy

Idit Avrahami , Dafna Raz, and Oranit Bash

Department of Mechanical Engineering and Mechatronics, Ariel University, Ariel, Israel

Correspondence should be addressed to Idit Avrahami; iditavrahami@gmail.com

Received 16 June 2018; Revised 25 August 2018; Accepted 17 September 2018; Published 28 October 2018

Guest Editor: Dominique J. Monlezun

Copyright © 2018 Idit Avrahami et al. This is an open access article distributed under the Creative Commons Attribution License, which permits unrestricted use, distribution, and reproduction in any medium, provided the original work is properly cited.

The carotid bifurcation tends to develop atherosclerotic stenoses which might interfere with cerebral blood supply. In cases of arterial blockage, the common clinical solution is to remove the plaque via carotid endarterectomy (CEA) surgery. Artery closure after surgery using primary closures along the cutting edge might lead to artery narrowing and restrict blood flow. An alternative approach is patch angioplasty which takes longer time and leads to more during-surgery complications. The present study uses numerical methods with fluid-structure interaction (FSI) to explore and compare the two solutions in terms of hemodynamics and stress and strain fields developed in the artery wall.

1. Introduction

The carotid bifurcation tends to develop atherosclerotic stenosis, which might interfere with cerebral blood supply and can cause coma, hemodynamic disturbance, stroke, and even death. The common clinical solution is to remove the plaque via carotid endarterectomy (CEA) surgery [1], with approximately 100,000 CEAs performed in the United States each year [2–4]. There are few approaches for postsurgery closure [5], and the preferred closure technique still remains an issue of debate [6, 7].

The CEA procedure often associated with intimal hyperplasia [8] or progression of atherosclerosis in the zone of arterial reconstructions [9], attributed to the inflammatory process due to foreign materials in vascular reconstruction [10].

A regular suture (primary closure) is the simplest way to close an arteriotomy, which leads to smaller artery diameter and increased stiffness of the structure. Therefore, routine use of patch graft has been advocated to reduce restenosis, stroke, and death [11, 12]. Patch angioplasty reduces the risk of immediate postoperative complications, results in a larger carotid artery diameter, and significantly lowers vessel restenosis and occlusion rates [13], especially in women [14].

However, the procedure of patch suturing takes longer and thus might increase the risk of stroke and death during surgery. Moreover, a concern is raised about the thrombogenic nature of the conventionally used patches and their protective effect, particularly from late restenosis [15]. Patch angioplasty has also been associated with specific complications, such as patch rupture or expansion and increased risk of infection [16]. In addition, carotid patch was shown to promote irregular neointimal lining with prominent proliferative activity [17].

According to a statistical study by Mannheim et al. [18], a 2-year restenosis-free rate is 97.6% for patch angioplasty vs. 90.9% for primary closure. Nevertheless, overall mortality or morbidity is similar for all closure procedures [13, 19, 20]. Therefore, the use of patch grafts today is targeted selectively only to patients who have very small (<4 mm) or highly constricted and tortuous vessels [7, 20].

There are several types of patches such as prosthetic patches (woven Dacron or PTFE), venous patches, and biomaterial patches (bovine pericardium) [6, 21]. Vein patch is considered the preferred one, thanks to its high compliance and biocompatibility [14]; its main disadvantage is the need for an additional incision to obtain it and occasional deterioration with aneurysmal dilatation and rupture [16]. The advantages of prosthetic patches include

immediate availability, avoidance of additional incision, and preservation of vein for future use in other cardiovascular operations. The main shortcomings of the prosthetic patches are higher thrombogenicity, increased risk for infection [22], and higher risks for infections [6]. Bovine pericardium patches recently proved high durability and better long-term survival rates, compared to the other patches [23]. Overall, despite the preference of using biological patches, the clinical results with most available synthetic patches are currently similar enough to prevent clear recommendation of any particular one [6].

Some studies used computational fluid dynamics (CFD) to investigate the blood flow regime in the post-CEA region in patient-specific geometries. Harrison et al. [24] showed that incorporation of a patch indeed increases the artery diameter, but it results with larger areas of low-wall shear stress (WSS) and high-oscillatory shear index (OSI) at the bifurcation, and therefore, its benefit is questionable. Similarly, Guerciotti et al. [25] and Domanin et al. [26] also analyzed WSS, vorticity, time-averaged OSI, and relative residence time (RRT). According to all these studies, cases with primary suture resulted with better hemodynamic parameters and smaller areas of disturbed flow in comparison with patch graft cases. Especially, OSI and RRT values were generally higher in patch graft cases with respect to primary closure, especially for high carotids or when the arteriotomy is mainly at the bulb region.

Although these studies discussed the effect of the closing approach on blood flow hemodynamics to support the clinical decision and to provide a hemodynamic insight into the patch complications, they neglected the biomechanical effect on the arterial tissue and the artificial graft. Excessive stress and cyclic strains are correlated to risk of patch rupture, aneurysms, wall injury, restenosis, irregular neo-intimal lining [27]. Kamenskiy et al. [22] used fluid-structure interaction (FSI) numerical simulations to explore tissue strain and stress in addition to WSS parameters for models with different patch types, widths, and location. In their study, they showed that narrow patches are superior to wide patches, and anterior arteriotomy are superior to lateral arteriotomy.

As far as we know, no study examined the biomechanical aspects of patch angioplasty in comparison to primary suture. In this study, we use FSI numerical models in order to examine the hemodynamics and biomechanical aspects of the patch procedure in comparison with primary suture.

2. Methods

2.1. Cases Studied and Models Geometry. The research study used FSI numerical simulations to explore blood flows and wall dynamics in five different models of the carotid artery region. The examined cases are listed in Table 1.

The geometric specifications of healthy and postsurgery bifurcation models were based on data specified by Tada and Tarbell [28] and Halak et al. [29]. The geometries were idealized to represent a typical model within the framework of the anatomy variance. Geometry dimensions are shown in

TABLE 1: Cases studied.

Case#1	A healthy carotid bifurcation: a time-dependent simulation of the coupled domains
Case#2	A narrowed postoperation carotid bifurcation with a suture: a time-dependent simulation of the coupled domains
Case#3	A widened carotid bifurcation with a <i>high</i> flexibility patch: a time-dependent simulation of the coupled domains
Case#4	A widened carotid bifurcation with a <i>medium</i> flexibility patch: a time-dependent simulation of the coupled domains
Case#5	A widened carotid bifurcation with a <i>low</i> flexibility patch: a time-dependent simulation of the coupled domains

Figure 1 and detailed in Table 2. The fluid and the structural domains of the model are shown in Figure 2.

2.2. Mathematical Model. Blood was assumed homogenous and Newtonian fluid with viscosity of $\mu = 0.0035$ gr/cm-s and density of $\rho = 1.05$ g/cm³. The flow was assumed laminar, and the arterial wall was assumed linearly elastic with an elasticity of $E = 5 \times 10^6$ dyn/cm² and Poisson's ratio of $\nu = 0.499$ [30]. Small displacement/small-strain formulation was assumed. Patches and suture parameters are listed in Table 3.

The flow and pressure fields in the fluid domain (Ω_f) were calculated by solving the governing equations for the fluid domain for laminar, Newtonian, and incompressible flow in a nongravity field:

$$\left. \begin{aligned} \nabla \cdot \mathbf{U}_f &= 0, \\ \rho_f \left(\frac{\partial \mathbf{U}_f}{\partial t} + \mathbf{U}_f \cdot \nabla \mathbf{U}_f \right) &= -\nabla P + \mu \cdot \nabla^2 \mathbf{U}_f, \end{aligned} \right\} \text{ in } \Omega_f, \quad (1)$$

where P is the static pressure, \mathbf{U}_f is the velocity vector, t is the time, ρ_f is the fluid density, and μ is the dynamic viscosity.

The governing equation for the solid domain (Ω_s) is the Lagrangian momentum conservation equation:

$$\left. \rho_s \frac{\partial^2 \mathbf{d}_s}{\partial t^2} - \nabla \cdot \boldsymbol{\sigma}_s = \mathbf{f} \right\} \text{ in } \Omega_s, \quad (2)$$

where $\boldsymbol{\sigma}_s$ is the Cauchy stress tensor, \mathbf{d}_s is the vector of structure displacement, ρ_s is the wall density, and \mathbf{f} represents the body force applied on the structure.

We used artificial boundary conditions (BC) [22, 31] for the fluid domain as follows. Prescribed velocity conditions $\int (\mathbf{U} \cdot \mathbf{n}) dA = Q(t)$ were imposed at the ICA and the ECA outlets (marked as Γ_f^{ICA} and Γ_f^{ECA} in Figure 2), reflecting a typical physiological waveform [30] of a normal healthy human with a heart rate of 60 bpm, as shown in Figure 3. At the CCA inlet (Γ_f^{in}), stress free conditions were employed, thus the CCA flow was achieved from mass conservation. In addition, a typical physiological time-dependent pressure was imposed, as shown in Figure 4, based on a systolic/diastolic pressure of 120/80 mmHg:

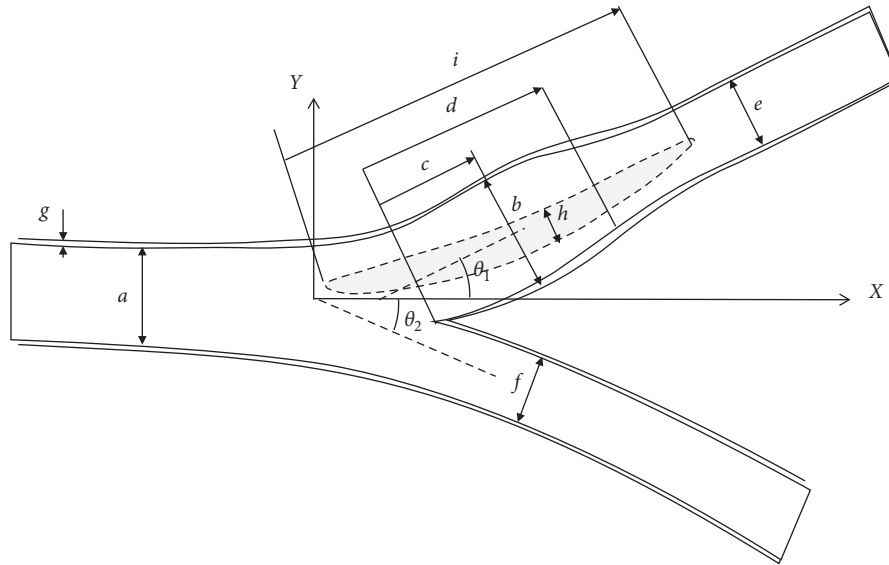


FIGURE 1: Geometry of the artery bifurcation.

TABLE 2: Geometric dimensions of the bifurcation models.

Dimension	Labels in Figure 1	Value (mm)		
		Healthy	Suture	Patch
CCA internal diameter	a	6.6		
Max. bulb internal diameter	b	7.8	7.0	8.4
Max. bulb location	c	7.7		
Bulb length	d	16.0		
ICA internal diameter	e	5.0		
ECA internal diameter	f	4.7		
Wall thickness	g	0.7		
Patch width	h			8.0
Patch length	i			18.0
Patch thickness		0.7	0.7	0.7
ICA bifurcation	θ_1	25°		
ECA bifurcation	θ_2	25°		

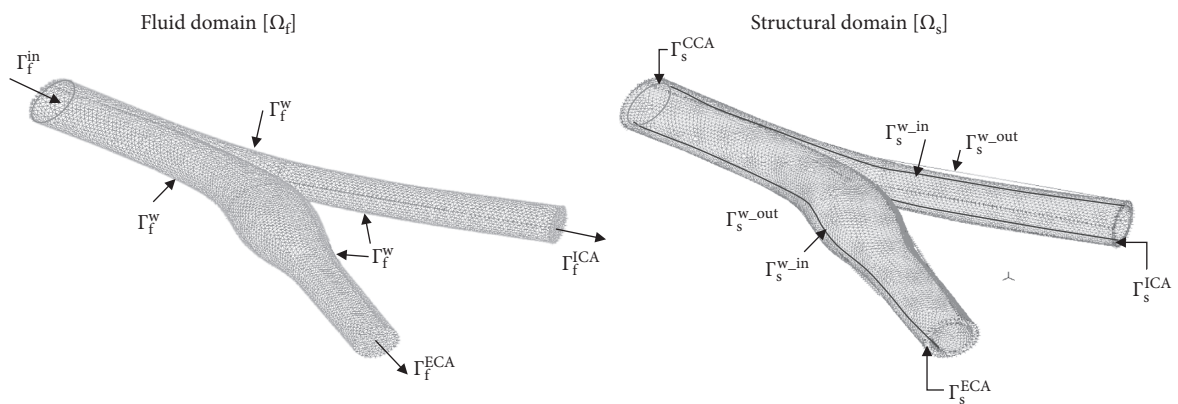


FIGURE 2: The fluid (Ω_f) and Structural (Ω_s) domains and the corresponding boundary conditions (specified in Equations (1)–(3)).

TABLE 3: Material properties.

ν	E ($\cdot 10^6$ dyn/cm ²)	ρ (g/cm ³)	μ (dyn*s/cm ²)	
		1.05	$3.5 \cdot 10^{-2}$	Blood
0.499	5	1.05		Artery
0.499	10	1.05		High flexibility patch
0.499	200	1.05		Medium flexibility patch
0.499	800	1.05		Low flexibility patch
0.37	2000	1.35		Suture

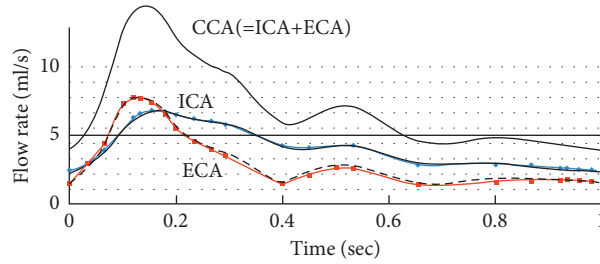


FIGURE 3: Time-dependent flow at the three arteries outlets (CCA, ICA, and ECA) [30].

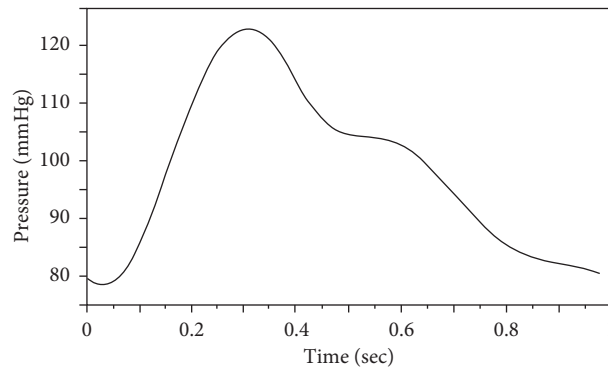


FIGURE 4: Imposed arterial pressure as a function of time [30].

$$\mathbf{n} \cdot \boldsymbol{\tau}_f = 0, P = P(t) \quad \text{on } \Gamma_f^{\text{in}}, \quad (3)$$

where $\mathbf{n} \cdot \boldsymbol{\tau}_f$ are the normal stresses to the surface. BC on the structural domains were fixed ($\mathbf{d}_s = 0$) at the edges $\Gamma_s^{\text{CCA}}, \Gamma_s^{\text{ECA}},$ and $\Gamma_s^{\text{ICA}},$ and stress-free conditions ($\partial \mathbf{d}_s / \partial \mathbf{n} = 0$) were set at the outer faces $\Gamma_s^{\text{w-out}}$.

The BC at the FSI interfaces (Γ_f^{w} and $\Gamma_s^{\text{w-in}}$) states that (i) displacements of the fluid and solid domain must be compatible, (ii) tractions at these boundaries must be at equilibrium, and (iii) fluid obeys the no-slip/no-penetration conditions. These conditions are given in the following equations:

$$\left. \begin{array}{l} \mathbf{d}_f = \mathbf{d}_s, \mathbf{U}_f = \dot{\mathbf{d}}_s, \\ \mathbf{n} \cdot \boldsymbol{\tau}_f = \mathbf{n} \cdot \boldsymbol{\sigma}_s, \end{array} \right\} \quad \text{on } \Gamma_f^{\text{w}} \text{ and } \Gamma_s^{\text{w-in}}, \quad (4)$$

where $\boldsymbol{\sigma}_s, \boldsymbol{\tau}_f, \mathbf{d}_s,$ and \mathbf{d}_f are the wall structure, fluid stress tensors, and wall displacement, respectively.

2.3. Numerical Model. The simulations used the commercial package ADINA (ADINA R&D, Inc., v. 9.0.0) to solve

numerically the governing differential equations (Equations (1) and (2)) using the finite elements method (FEM).

The fluid domain (Ω_f) was meshed using 3D 1st order tetrahedral elements, and the structural domain was meshed using triangular 3D 2nd order tetrahedral elements. Several mesh and time-step independence tests were conducted, where the simulations results obtained from several numerical models with different mesh and time steps were compared (Appendix). Based on these tests, the numerical model selected was with $\sim 100,000$ fluid elements and $\sim 20,000$ structural elements. Each cardiac cycle consisted of 28 time steps of 0.035 sec, and the automatic-time-stepping procedure was used to subdivide the load-step increment when necessary. Three cardiac cycles were computed to obtain results independent of the initial conditions. The results of the third calculated cycle were fully periodic. Convergence is achieved when all mass, velocity component, and energy changes, from iteration to iteration, achieved are less than 10^{-5} root-mean-square error (RMSE).

The three mesh models (of the healthy, suture, and patch) are shown in Figure 5. The suture or the patch elements (marked in red in the figure) were fully connected to the

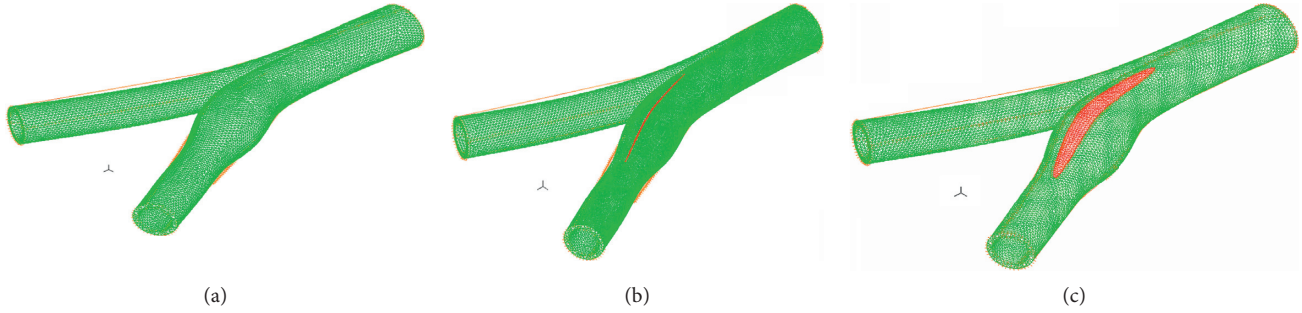


FIGURE 5: Mesh models of the healthy artery (a), suture (b), and patch (c).

arterial elements (marked in green). In the suture model, 817 elements were defined as suture, and in the patch models, 5790 elements were defined as patches. The suture or the patch elements were defined as fully connected to the arterial elements.

The ADINA iterative solver was used for the FSI coupling [32]. The fluid and the structure solvers were solved iteratively until convergence was reached or until it reached 150 iterations. The FSI algorithm included models of linear wall displacements and strains. In order to control the moving mesh under deformations of the flow domains, the arbitrary Lagrangian-Eulerian (ALE) approach was defined on geometric entities. The ALE approach integrates the Eulerian description of the fluid domain with the Lagrangian formulation of the moving mesh using curvature correction [32, 33]. The Newton–Raphson method was used to solve the nodal matrices [34, 35]. A first-order Euler backward implicit time integration method was used for the time marching.

2.4. Examined Parameters. The simulations examined several hemodynamic and biomechanical parameters in order to address the effect of the patch or primary suture in the carotid bifurcation, including effective stress, flow patterns, time-averaged WSS (TAWSS), and OSI. These parameters are known as critical factors in artery occlusion and thrombosis [36].

Wall stresses of the arterial tissue and artificial graft were calculated as the product of blood viscosity and the local velocity gradient in the direction of local surface normal (\mathbf{n}):

$$\boldsymbol{\tau}_w = \mu \frac{\partial \mathbf{u}}{\partial \mathbf{n}}. \quad (5)$$

TAWSS and OSI were calculated according to Equations (6) and (7):

$$\text{TAWSS} = \frac{1}{T} \int_0^T |\boldsymbol{\tau}_w| dt, \quad (6)$$

$$\text{OSI} = 0.5 \left(1 - \frac{\int_0^T \boldsymbol{\tau}_w dt}{\int_0^T |\boldsymbol{\tau}_w| dt} \right), \quad (7)$$

where $\boldsymbol{\tau}_w$ represents the instantaneous WSS vector and T represents the period of the cardiac cycle.

3. Results

3.1. Structural Results. Effective stresses at the wall were calculated at each point according to von Mises criteria. In all cases, elevated effective stresses were found at the bifurcation origin and bifurcation junction (Figures 6 and 7). In the suture and patches with medium and low flexibility cases, there were higher effective stresses (with values above 70 kPa) along the sutures. For the case with high flexibility patch, stress distribution resembled the values of healthy case.

4. Results of Fluid

Figure 8 presents midplane velocity vectors in a magnified view of the bulb for the five models after peak flow at the time $t = 0.385$ sec. In all five cases, a recirculation zone appears in the outer side of the bifurcation bulb. In the healthy case, the recirculation zone is small and most of the flow is unidirectional. In the model of the primary suture, the smaller diameter leads to a sustained velocity stream leaving room to a narrow vortex with less recirculation. In the patch model, although the diameter bulb is wide and the flow has plenty of room, the larger diameter promotes a large vortex that takes over almost the whole bulb space, which interferes with the axial flow stream.

Figure 9 presents time-averaged wall shear stress (TAWSS), and Figure 10 presents the oscillatory shear index (OSI) distribution in the five models. Lower TAWSS and higher OSI values were present mostly in the bulb area, and low values of TAWSS and high values of OSI were rarely found in the primary suture case (in respect with the other cases) because of the smaller diameter in the bulb area.

5. Discussion

High-concentration stresses are found in the suture and low-flexibility patch cases (Figures 6 and 7). The stress concentrations are a result of the discontinuity of the material property of the patch and suture from the arterial wall. High-effective stress values are also found at the bifurcation junction. The values (in the range of 0.5–70 kPa) are in agreement with values reported by Kamenskiy et al. [22]. Concentration of stresses on the artificial graft might imply a higher risk of rupture. High stresses at the arterial wall might lead to atherosclerosis and neointima growth [37–39].

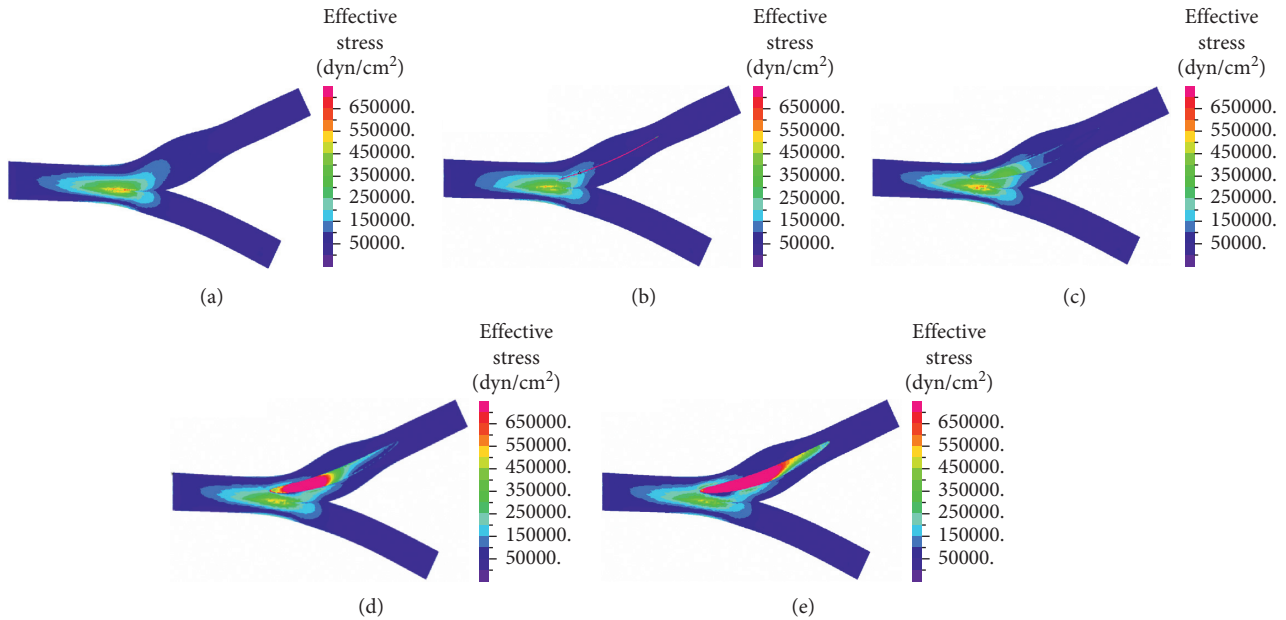


FIGURE 6: Effective stresses—top view in healthy artery (a), suture (b), high flexibility patch (c), medium flexibility patch (d), and low flexibility patch (e).

When there is stress concentration over a larger area (like in the low flexibility patch), the chances of developing restenosis are larger. The high flexibility patch resulted in lower stresses (>35 kPa), both at the artificial graft and the arterial wall. Therefore, in specific cases, when it is decided to prefer a patch over a suture in patients with relatively small arteries, high flexibility patch (such as vein or bovine patch) should result in lower risk for stress-induced restenosis because its properties resemble those of the artery. However, they have a larger risk of forming an aneurysm. Ultimately, the primary suture exhibits effective stress distribution in the artery similar to the healthy artery, indicating that, from our study, the primary suture has less potential effect on the arterial tissue.

From examination of flow patterns in the different models (Figure 8), we conclude that some vortical flow patterns are found in all cases but in different sizes. In a primary suture model, the flow in the bulb is mostly unidirectional and only a negligible vortex is found. In the patch and in the healthy models, the large diameter bulb promotes a large vortex that dominates the flow. According to Gimbrone et al. [40], vortices and disruptions in the flow are factors that cause a decrease in endothelial function and eventually might increase risk for stenosis or other vascular diseases. In addition, these vortices might disturb the flow and lead to thrombus formation and thus increase the risk for stroke.

The results of TAWSS (Figure 9) and OSI (Figure 10) reveal that WSS values in the bulb region are similar to the healthy case and the patches cases, while in the suture case, the values are higher. It can be concluded that bulb diameter is the cause for variations in WSS. In regions with larger diameter, the velocities are smaller, and therefore, WSS are smaller and OSI are higher. Low WSS and high OSI are

correlated with plaque deposition, artery occlusion, and endothelium dysfunction [41]. Therefore, from our study, the suture case which has higher WSS and lower OSI is also preferred by this parameter. These results agree with Domanin et al. [26] that showed higher values of OSI and RRT in patch graft vs. direct suture cases in patient-specific simulations, and with Kamenskiy et al. [22] that showed that artery with a narrow patch showed significant improvement in hemodynamics in comparison with wider patches.

The influence of fluid shear forces on structure dynamics is relatively small. WSS is negligible (<70 dyn/cm²) compared to the effected stresses due to hydrostatic pressure ($<70,000$ dyn/cm²). Therefore, when a simplified simulation is needed for estimation of local effective stresses, it may be valid to consider the structural domain separately from the fluid domain.

The study assumes a relatively simplified model of a specific anatomy, with linearly elastic material and Newtonian fluid, and does not consider possible physiological or anatomic variations between healthy and post-CEA [29]. The actual values are highly geometry-dependent and therefore, patient-specific. Moreover, in reality, during the CEA procedure, a part of the media layer is removed, with only adventitia layer remaining. This might further increase the effective stress in the bifurcation wall in relation with the healthy case and increase the risk for rupture or aneurysm. In addition, the results and conclusions discuss only the mechanical aspects and did not take the clinical aspect as argument.

Another limitation relates to the time and space discretization parameters. Note that a time-step interval of 0.035 sec is relatively elevated, in respect of systolic interval (of 0.4 sec), and may limit capturing the systolic fluid dynamics. To minimize this limitation, an automatic-time-stepping

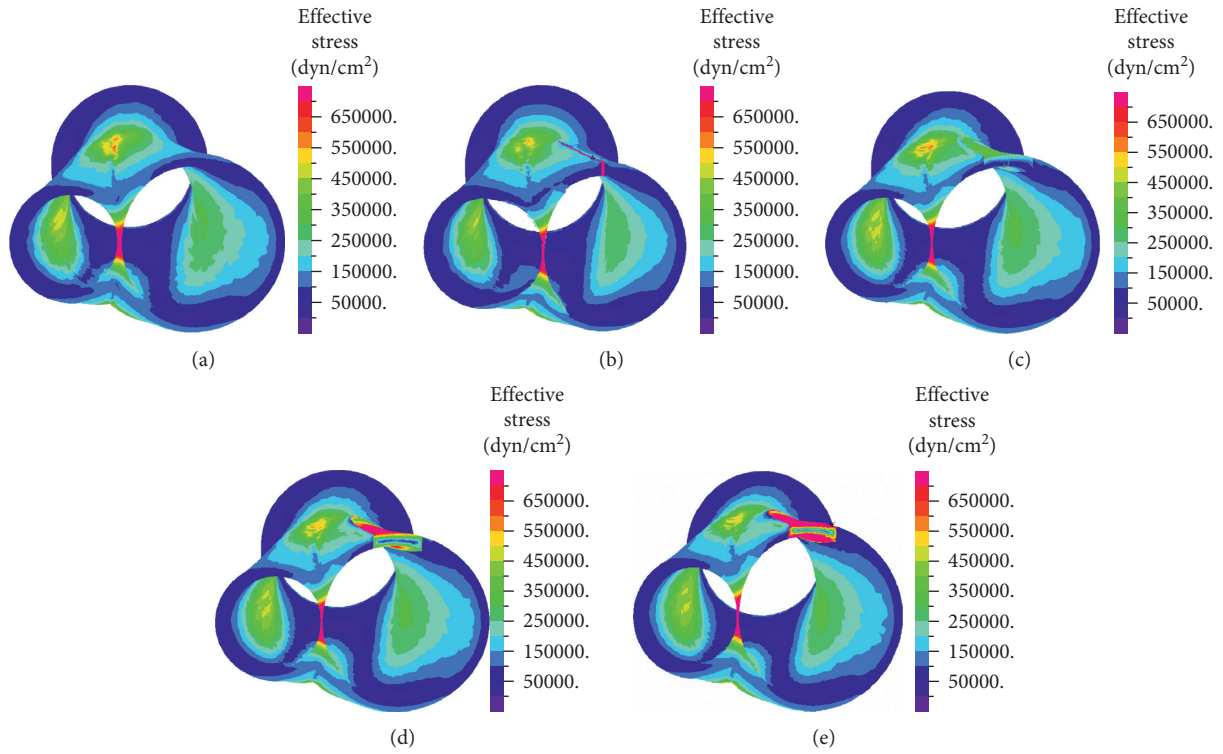


FIGURE 7: Effective stresses—cut view in healthy artery (a), suture (b), high flexibility patch (c), medium flexibility patch (d), and low flexibility patch (e).

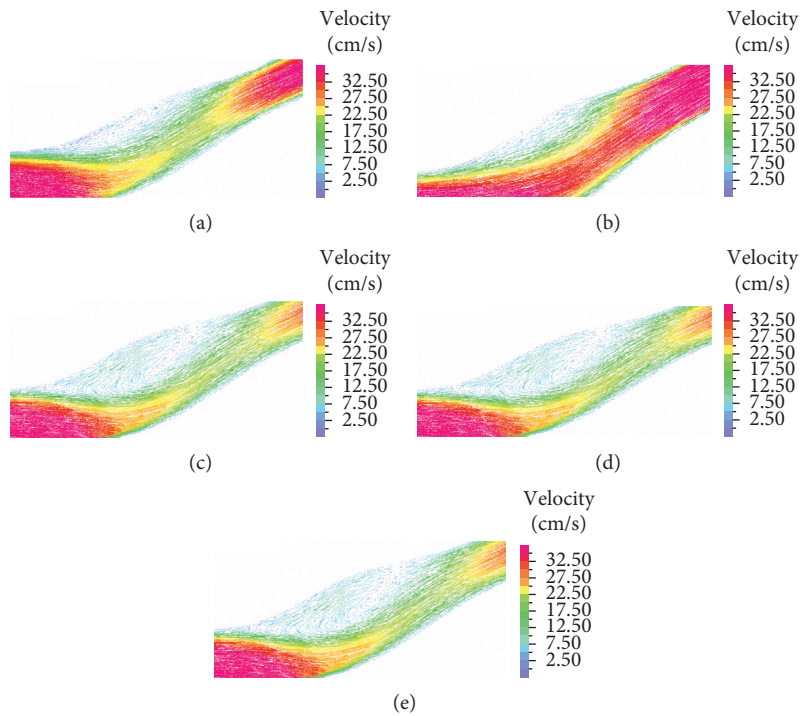


FIGURE 8: Velocity vectors—magnified view in healthy artery (a), suture (b), high flexibility patch (c), medium flexibility patch (d), and low flexibility patch (e).

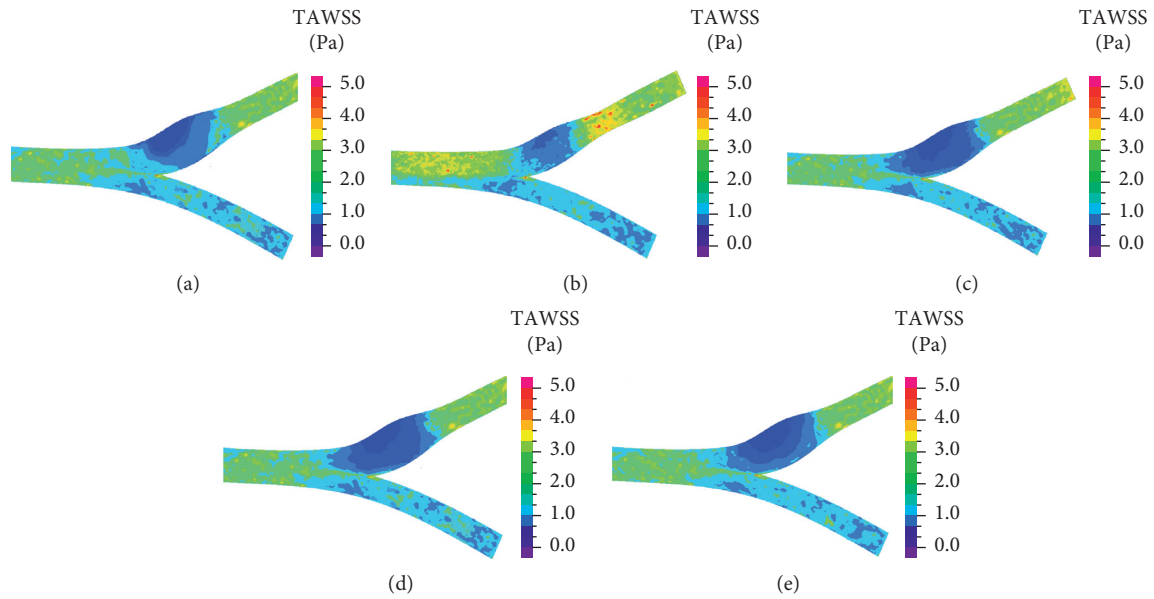


FIGURE 9: Time-averaged WSS in healthy artery (a), suture (b), high flexibility patch (c), medium flexibility patch (d), and low flexibility patch (e).

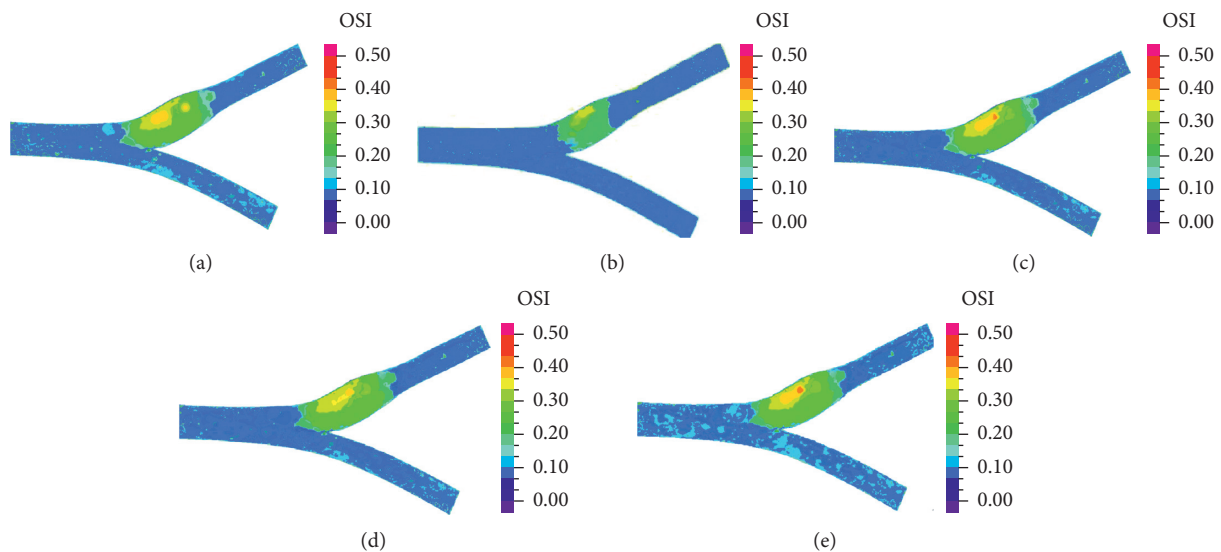


FIGURE 10: OSI in healthy artery (a), suture (b), high flexibility patch (c), medium flexibility patch (d), and low flexibility patch (e).

procedure was used to subdivide the load-step increment when necessary. According to our mesh and time discretization refinement studies (Appendix), the discretization errors in the calculation of WSS are up to 10%.

However, the model results are in agreement with clinical and previous studies [25, 26, 42], and the comparative results between the different models are clear and distinct. Most guidelines suggest to prefer primary suture for narrow ICA (>4 mm), and the current model assumes ICA with 5 mm, showing preferred performance with primary patch. This study may delineate the dominant parameters affecting the combined hemodynamic and biomechanics of the patches versus suture approach. Thus, its results may

shed a light on the controversy between physicians regarding the preferred approach and explain the reason for the nonsignificant advantage of the patch procedure in CEA.

6. Conclusion

In this manuscript, we examined the biomechanical aspects of patch angioplasty in comparison with primary suture. The examined parameters included elevated stress, in addition to the previously examined hemodynamic (WSS) parameters. Based on our results of elevated stress and OSI values and low TAWSS values, primary suture has shown better

performance in our study than patch, and the high flexibility patch has shown better performance compared to lower flexibility patch.

Data Availability

The data used to support the findings of this study are included within the article and appendix. Raw data files of the models and simulations can be released upon application to the corresponding author (iditav@ariel.ac.il).

Conflicts of Interest

The authors declare that they have no conflicts of interest.

Acknowledgments

The research was partly funded by the Ariel Research Authority.

Appendix

A. Model Validation

A.1. Time-Step Independence Tests. Mesh and time-step independence tests were conducted to validate the numerical model. To evaluate the optimal time-step size for the transient simulations, FSI simulations of the healthy case with the mesh of 100,000 elements were performed using 28 steps of 0.035 sec and 98 steps of 0.01 sec. The resulted maximal values in the domains for the two cases are detailed in Table 4.

To evaluate the discretization error, we calculated the relative difference (ERR) between the maximal value in the course and the fine time resolution, as follows:

$$ERR_i (\%) = \left(\frac{(X)_{\text{fine}} - (X)_{\text{course}}}{(X)_{\text{fine}}} \right) * 100 (\%), \quad (\text{A.1})$$

where X is the maximal value in the domain (velocity and shear stress in the fluid domain and effective stress in the structural domain). The resulted errors are detailed in the table. The results show that the time step of $dt = 0.035$ sec is sufficient, with $ERR < 2\%$ in the three critical parameters. Therefore, for the transient analyses in this study, 28 steps were set per cycle.

Note that only maximum values were examined (in space and time), thus instantaneous differences at a given instance (e.g., systole) were not examined. Note that this time-step interval is relatively elevated, in respect of systolic interval (of 0.4 sec), and may limit capturing the systolic fluid dynamics. To minimize this limitation, an automatic-time-stepping procedure was used to subdivide the load-step increment when necessary.

A.2. Mesh Independence Tests. To evaluate the optimal mesh resolution, three models of the healthy base case with different mesh resolutions were built (with 50,000–500,000 elements). The models were simulated during a period of one cardiac cycle, each with 28 time steps. The resulted maximal values in the domains of each model mesh are listed in

TABLE 4: Resulted values with different time steps (error in % is indicated in parentheses).

Time step (sec)	0.035	0.01
Max. velocity magnitude (cm/s)	58.5 (1.8%)	59.5
Max. shear stress (dyn/cm ²)	122.1 (1.7%)	124.2
Max. effective stress (dyn/cm ²)	2.12×10^7 (1.8%)	2.15×10^7

TABLE 5: Maximum values for different mesh resolutions (error in % is indicated in parentheses).

No. of elements	51,544	100,268	484,401
Max. velocity magnitude (cm/s)	57.5 (5.7%)	58.5 (2.7%)	60.1
Max. shear stress (dyn/cm ²)	94.7 (28.1%)	122.1 (3.5%)	126.4
Max. effective stress (dyn/cm ²)	1.64×10^7 (28.9%)	2.12×10^7 (8.5%)	2.21×10^7

Table 5, together with their error relative to the finest mesh (Equation (A.1)). Based on these results, mesh resolutions of 100,000 elements were found suitable for our model with $ERR \leq 10\%$ of the finest mesh.

References

- [1] N. A. S. C. E. T. Collaborators*, “Beneficial effect of carotid endarterectomy in symptomatic patients with high-grade carotid stenosis,” *New England Journal of Medicine*, vol. 325, no. 7, pp. 445–453, 1991.
- [2] J. H. Lichtman, M. R. Jones, E. C. Leifheit et al., “Carotid endarterectomy and carotid artery stenting in the US Medicare population, 1999–2014,” *JAMA*, vol. 318, no. 11, pp. 1035–1046, 2017.
- [3] D. C. Hsia, L. M. Moscoe, and W. M. Krushat, “Epidemiology of carotid endarterectomy among Medicare beneficiaries: 1985–1996 update,” *Stroke*, vol. 29, no. 2, pp. 346–350, 1998.
- [4] R. W. Hobson, W. C. Mackey, E. Ascher et al., “Management of atherosclerotic carotid artery disease: clinical practice guidelines of the Society for Vascular Surgery,” *Journal of Vascular Surgery*, vol. 48, no. 2, pp. 480–486, 2008.
- [5] K. I. Paraskevas, V. Robertson, A. N. Saratzis, and A. R. Naylor, “An updated systematic review and meta-analysis of outcomes following eversion vs. conventional carotid endarterectomy in randomised controlled trials and observational studies,” *European Journal of Vascular and Endovascular Surgery*, vol. 67, no. 5, p. 1632, 2018.
- [6] D. Treat-Jacobson, K. Fitzgerald, A. Foley, C. AGACNP, and D. Kohlman-Trigoboff, “Society for Vascular Nursing Carotid Endarterectomy (CEA) Updated Nursing Clinical Practice Guideline,” *Journal of Vascular Nursing*, vol. 35, no. 2, pp. 90–111, 2017.
- [7] J. Byrne, P. Feustel, and R. C. Darling, “Primary closure, routine patching, and eversion endarterectomy: what is the current state of the literature supporting use of these techniques?,” *Seminars in Vascular Surgery*, vol. 20, no. 4, pp. 226–235, 2007.
- [8] A. Szabó, E. Brazda, E. Dósa, A. Apor, Z. Szabolcs, and L. Entz, “Long-term restenosis rate of eversion endarterectomy on the internal carotid artery,” *European Journal of Vascular and Endovascular Surgery*, vol. 27, no. 5, pp. 537–539, 2004.

- [9] G. P. Clagett, M. Robinowitz, J. R. Youkey et al., "Morphogenesis and clinicopathologic characteristics of recurrent carotid disease," *Journal of Vascular Surgery*, vol. 3, no. 1, pp. 10–23, 1986.
- [10] C. Lattimer and K. Burnand, "Recurrent carotid stenosis after carotid endarterectomy," *British Journal of Surgery*, vol. 84, no. 9, pp. 1206–1219, 1997.
- [11] R. Bond, K. Rerkasem, A. Naylor, A. Aburahma, and P. Rothwell, "Systematic review of randomized controlled trials of patch angioplasty versus primary closure and different types of patch materials during carotid endarterectomy," *Journal of Vascular Surgery*, vol. 40, no. 6, pp. 1126–1135, 2004.
- [12] K. J. Ho, L. L. Nguyen, and M. T. Menard, "Intermediate-term outcome of carotid endarterectomy with bovine pericardial patch closure compared with Dacron patch and primary closure," *Journal of Vascular Surgery*, vol. 55, no. 3, pp. 708–714, 2012.
- [13] V. Maertens, H. Maertens, M. Kint, C. Coucke, and Y. Blomme, "Complication rate after carotid endarterectomy comparing patch angioplasty and primary closure," *Annals of Vascular Surgery*, vol. 30, pp. 248–252, 2016.
- [14] A. F. AbuRahma, P. A. Robinson, S. Saiedy, J. H. Khan, and J. P. Boland, "Prospective randomized trial of carotid endarterectomy with primary closure and patch angioplasty with saphenous vein, jugular vein, and polytetrafluoroethylene: long-term follow-up," *Journal of Vascular Surgery*, vol. 27, no. 2, pp. 222–234, 1998.
- [15] A. F. AbuRahma, P. A. Robinson, R. S. Hannay, J. Hudson, and L. Cutlip, "Prospective controlled study of carotid endarterectomy with Hemashield patch: is it thrombogenic?," *Vascular and Endovascular Surgery*, vol. 35, no. 3, pp. 167–174, 2001.
- [16] J. P. Archie, "Carotid endarterectomy saphenous vein patch rupture revisited: selective use on the basis of vein diameter," *Journal of Vascular Surgery*, vol. 24, no. 3, pp. 346–352, 1996.
- [17] M. Ito, Y. Niiya, H. Uchino, N. Nakayama, S. Mabuchi, and K. Houkin, "Irregular neointimal lining with prominent proliferative activity after carotid patch angioplasty: an autopsy case report," *World Neurosurgery*, vol. 82, no. 1–2, pp. 240.e1–240.e6, 2014.
- [18] D. Mannheim, B. Weller, E. Vahadim, and R. Karmeli, "Carotid endarterectomy with a polyurethane patch versus primary closure: a prospective randomized study," *Journal of Vascular Surgery*, vol. 41, no. 3, pp. 403–407, 2005.
- [19] P. G. Al-Rawi, C. L. Turner, V. Waran, I. Ng, and P. J. Kirkpatrick, "A randomized trial of synthetic patch versus direct primary closure in carotid endarterectomy," *Neurosurgery*, vol. 59, no. 4, pp. 822–829, 2006.
- [20] K. Rerkasem and P. M. Rothwell, "Patch angioplasty versus primary closure for carotid endarterectomy," *Cochrane Database of Systematic Reviews*, vol. 7, no. 4, 2009.
- [21] A. Muto, T. Nishibe, H. Dardik, and A. Dardik, "Patches for carotid artery endarterectomy: current materials and prospects," *Journal of Vascular Surgery*, vol. 50, no. 1, pp. 206–213, 2009.
- [22] A. V. Kamenskiy, J. N. MacTaggart, I. I. Pipinos, P. K. Gupta, and Y. A. Dzenis, "Hemodynamically motivated choice of patch angioplasty for the performance of carotid endarterectomy," *Annals of Biomedical Engineering*, vol. 41, no. 2, pp. 263–278, 2013.
- [23] W. A. Oldenburg, T. Almeray, M. Selim, H. Farres, and A. G. Hakaim, "Durability of carotid endarterectomy with bovine pericardial patch," *Annals of Vascular Surgery*, vol. 50, pp. 218–224, 2018.
- [24] G. J. Harrison, T. V. How, R. J. Poole et al., "Closure technique after carotid endarterectomy influences local hemodynamics," *Journal of Vascular Surgery*, vol. 60, no. 2, pp. 418–427, 2014.
- [25] B. Guerciotti, C. Vergara, L. Azzimonti et al., "Computational study of the fluid-dynamics in carotids before and after endarterectomy," *Journal of Biomechanics*, vol. 49, no. 1, pp. 26–38, 2016.
- [26] M. Domanin, D. Bissacco, D. Le Van, and C. Vergara, "Computational fluid dynamic comparison between patch-based and primary closure techniques after carotid endarterectomy," *Journal of Vascular Surgery*, vol. 67, no. 3, pp. 887–897, 2018.
- [27] J. Ando and K. Yamamoto, "Effects of shear stress and stretch on endothelial function," *Antioxidants & Redox Signaling*, vol. 15, no. 5, pp. 1389–1403, 2011.
- [28] S. Tada and J. M. Tarbell, "Oxygen mass transport in a compliant carotid bifurcation model," *Annals of Biomedical Engineering*, vol. 34, no. 9, pp. 1389–1399, 2006.
- [29] M. Halak, S. Fajer, H. Ben-Meir, Z. Loberman, B. Weller, and R. Karmeli, "Neck irradiation: a risk factor for occlusive carotid artery disease," *European Journal of Vascular and Endovascular Surgery*, vol. 23, no. 4, pp. 299–302, 2002.
- [30] S. Tada and J. Tarbell, "A computational study of flow in a compliant carotid bifurcation—stress phase angle correlation with shear stress," *Annals of Biomedical Engineering*, vol. 33, no. 9, pp. 1202–1212, 2005.
- [31] L. Formaggia, A. Quarteroni, and A. Veneziani, *Cardiovascular Mathematics: Modeling and Simulation of the Circulatory System*, Vol. 1, Springer Science & Business Media, Berlin, Germany, 2010.
- [32] I. ADINA R&D, *ADINA Theory and Modeling Guide*, ADINA, Watertown, MA, USA, 2000.
- [33] K.-J. Bathe, *Finite Element Procedures*, Prentice Hall, Upper Saddle River, NJ, USA, 2006.
- [34] H. Zhang and K.-J. Bathe, *Direct and Iterative Computing of Fluid Flows Fully Coupled with Structures*, Computational Fluid and Solid Mechanics, 2001.
- [35] M. G. Doyle, S. Tavoularis, and Y. Bourgault, "Application of Parallel Processing to the Simulation of Heart Mechanics," in *High Performance Computing Systems and Applications*, Springer, Berlin, Germany, 2010.
- [36] T. Meirson, E. Orion, and I. Avrahami, "Numerical analysis of venous external scaffolding technology for saphenous vein grafts," *Journal of Biomechanics*, vol. 48, no. 10, pp. 2090–2095, 2015.
- [37] M. J. Thubrikar and F. Robicsek, "Pressure-induced arterial wall stress and atherosclerosis," *Annals of Thoracic Surgery*, vol. 59, no. 6, pp. 1594–1603, 1995.
- [38] R. S. Salzar, M. J. Thubrikar, and R. T. Eppink, "Pressure-induced mechanical stress in the carotid artery bifurcation: a possible correlation to atherosclerosis," *Journal of Biomechanics*, vol. 28, no. 11, pp. 1333–1340, 1995.
- [39] M. J. Thubrikar, S. K. Roskelley, and R. T. Eppink, "Study of stress concentration in the walls of the bovine coronary arterial branch," *Journal of Biomechanics*, vol. 23, no. 1, pp. 1519–1726, 1990.
- [40] M. A. Gimbrone, J. N. Topper, T. Nagel, K. R. Anderson, and G. Garcia-cardena, "Endothelial dysfunction, hemodynamic forces, and atherogenesis," *Annals of the New York Academy of Sciences*, vol. 902, no. 1, pp. 230–240, 2000.
- [41] C. Caro, J. Fitz-Gerald, and R. Schroter, "Atheroma and arterial wall shear observation, correlation and proposal of a shear dependent mass transfer mechanism for atherogenesis," in *Proceedings of the Royal Society of London. Series B. Biological Sciences*, vol. 177, 1046, pp. 109–133, 1971.
- [42] M. Domanin, A. Buora, F. Scardulla et al., "Computational fluid-dynamic analysis after carotid endarterectomy: patch graft versus direct suture closure," *Annals of Vascular Surgery*, vol. 44, pp. 325–335, 2017.

Research Article

The Time-Domain Integration Method of Digital Subtraction Angiography Images

Shuo Huang ^{1,2}, Le Cheng,³ Bin Zhu,³ Ping Zhou,¹ Yu Sun ^{1,4}, Bing Zhang ³, and Suiren Wan¹

¹School of Biological Sciences and Medical Engineering, Southeast University, Nanjing 210096, China

²Shanghai United Imaging Healthcare Co., Ltd., Shanghai 201807, China

³Department of Radiology, The Affiliated Drum Tower Hospital of Nanjing University Medical School, Nanjing 210008, China

⁴Institute of Cancer and Genomic Science, University of Birmingham, Birmingham B15 2TT, UK

Correspondence should be addressed to Yu Sun; 1546655418@qq.com

Received 21 May 2018; Accepted 28 August 2018; Published 30 September 2018

Academic Editor: Dominique J. Monlezun

Copyright © 2018 Shuo Huang et al. This is an open access article distributed under the Creative Commons Attribution License, which permits unrestricted use, distribution, and reproduction in any medium, provided the original work is properly cited.

The clarity improvement and the noise suppression of digital subtraction angiography (DSA) images are very important. However, the common methods are very complicated. An image time-domain integration method is proposed in this study, which is based on the blood flow periodicity. In this method, the images of the first cardiac cycle after the injection of the contrast agent are integrated to obtain the time-domain integration image. This method can be used independently or as a postprocessing method of the denoising method on the signal image. The experimental results on DSA data from an aortic dissection patient show that the image time-domain integration method is efficient in image denoising and enhancement, which also has a good real-time performance. This method can also be used to improve the denoising and image enhancement effect of some common models.

1. Introduction

Circulatory system diseases, such as aortic dissection, have been the focus of medical research [1, 2] for their dangerousness and high incidence. Improving the clarity of the captured medical image helps us to diagnose more accurately, which is an important research field.

Digital subtraction angiography (DSA), as a real-time approach, is commonly employed in the clinical diagnosis of circulatory system disease [3, 4], especially in the real-time surgical monitoring and the medical examination among small branches of blood vessels which are difficult to be measured by other methods. In order to protect the patient, it is important to shorten the shooting time and to reduce the dosage of contrast media when capturing the images.

A lot of image denoising methods have been proposed in recent years, but they are all problematic when applied to the DSA images. For example, the image reconstruction

method based on the level set theory [5], wavelet decomposition and reconstruction method [6, 7], Bayesian method [8], and image denoising method based on anisotropic diffusion [9] generally need a long operation time, which cannot meet the real-time requirements of DSA image processing. Moreover, images processed by these approaches are usually not clear enough to show the details such as edges and textures. In 2004, Candes et al. [10] proposed an image denoising method based on the sparse decomposition. On this basis, Needell and Vershynin [11] proposed the regularized orthogonal matching pursuit (ROMP) method; Scholefield and Dragotti [12] used a sparse quadtree decomposition representation to remove the noise in images; Adler et al. employed the shrinkage learning approach to acquire the high-resolution reconstruction image [13–17]. However, the operation of these approaches is also very complicated. Therefore, it is necessary to find an image processing method which is more suitable for the real-time analysis of DSA images.

In this work, an image time-domain integration method based on blood flow periodicity has been proposed. In this algorithm, the DSA images of the first cardiac cycle after the injection of the contrast agent are extracted denoised by the wavelet reconstruction method firstly, and then these images are integrated to obtain the time-domain integration image, which is named after the TDI image in this paper. This method contributes to the diagnosis of circulatory system diseases.

2. Materials and Methods

2.1. The Noise Model. The theoretical gray-scale $w_j(x_0, y_0)$ at a certain pixel (x_0, y_0) on the j -th frame of DSA images can be obtained from the following equation by the Lambert–Beer law [18, 19]:

$$\begin{aligned} w_j(x_0, y_0) &= -\ln\left(\frac{I_j(x_0, y_0)}{I_0(x_0, y_0)}\right) \\ &= -\ln\left(e^{-k \times \iiint_{V_j(x_0, y_0)} c(V_j) dV}\right) = k \times N_j(x_0, y_0), \end{aligned} \quad (1a)$$

where I_0 and I_r are the X-ray transmission amount before and after the addition of the contrast agent, respectively. $V_j(x_0, y_0)$ is the volume of blood vessels at pixel (x_0, y_0) . $N_j(x_0, y_0)$ and $c(V_j)$ are the number and amount of substance concentration of contrast agent particles at pixel (x_0, y_0) , respectively. k donates the absorption coefficient.

The image quality degrades in the original DSA image, as a result of the limitations on the imaging system's resolution and the influence of additive noise such as Gaussian noise, which is denoted by \mathbf{w}_j and can be expressed in as follows [6]:

$$\mathbf{W}_j = \mathbf{w}_j * \mathbf{h}_j + \mathbf{n}_j, \quad (1b)$$

where \mathbf{h}_j and \mathbf{n}_j represent the point spread function and the additive noise, respectively. Operator “*” is the convolution operator. Equation (1b) can be rewritten to matrix form using the block Toeplitz matrix \mathbf{H}_j , as shown in the following equation:

$$\mathbf{W}_j = \mathbf{w}_j \cdot \mathbf{H}_j + \mathbf{n}_j. \quad (1c)$$

It is difficult to solve Equation (1c) when only \mathbf{W}_j is given. However, since the gray-scale level of a certain pixel is proportional to the number of contrast agent particles in that pixel, the number of contrast agent particles follows the motion pattern of blood. And as for the blood motion pattern, on consideration of the periodicity of human heartbeat, the blood flow rate in human body is also cyclical, which can be expressed in the following equation:

$$\mathbf{v}_b(nT + t) = \overline{\mathbf{v}_b}(t) + \Psi(\overline{\mathbf{v}_b}), \quad t \in Z, \quad (2)$$

where $\mathbf{v}_b(nT + t)$ is the velocity field of blood at time $(nT + t)$. $\overline{\mathbf{v}_b}(t)$ denotes the average velocity field of blood at

time t , which is the mean flow velocity at the same time in multiple cardiac cycles. T is the length of the cardiac cycle. $\Psi(\overline{\mathbf{v}_b})$ characterizes the changes in flow velocity owing to factors such as the instability of human blood pressure. $\Psi(\overline{\mathbf{v}_b})$ can be regarded as a zero-mean-value distribution with a small variance, since patients are under the total anesthesia during the shooting process and their vital signs remain stable. According to the Wilke–Chang equation [20], the free diffusion rate of the contrast agent in the blood is much smaller than the blood flow rate, and thus the contrast agent obeys the same movement law as the blood. Therefore, the periodicity of the blood flow rate can be employed to improve the clarity of DSA images.

2.2. Image Integration. In order to decrease the shoot time and the contrast agent's injection quantity, images in the first cardiac cycle (denoted by the cardiac cycle S) after the injection of the contrast agent are analyzed in this study. Firstly, the time at which the cardiac cycle begins is set to be $t = 0$. Subsequently, the velocity of the i -th contrast agent particle in this cardiac cycle is expressed as $\mathbf{u}_i(t) = (\mathbf{u}_i(t) \cdot x, \mathbf{u}_i(t) \cdot y, \mathbf{u}_i(t) \cdot z)$. Since the motion of the contrast agent particles is consistent with that of the blood, and on consideration of the velocity stability shown in Equation (2), the velocity of the particle at each position on its trajectory can be regarded as a sample of the blood flow field at that location. Therefore, once the substantial number of particles is extracted, the average velocity field of the contrast agent at the pixel (x_0, y_0) in the entire cardiac cycle can be estimated by the mean velocity field value of particles which flowed through that pixel during the calculated cardiac cycle, as shown in the following equation:

$$\overline{\mathbf{v}_c}(x_0, y_0) = \frac{1}{N(x_0, y_0)} \sum_{i=1}^{N(x_0, y_0)} \mathbf{u}_i(t_i), \quad (3a)$$

where t_i represents the time when the i -th particle approached pixel (x_0, y_0) .

The total time length that the i -th particle appears in pixel (x_0, y_0) during one cardiac cycle T satisfies Equation (3b), where $L_i(x_0, y_0)$ represents the distance of the i -th particle in the range of pixel (x_0, y_0) and $u_{i//}(x_0, y_0)$ is set to be the magnitude of velocity component which is parallel to the image plane in pixel (x_0, y_0) during that cardiac cycle since the photographing each DSA image can be regarded as a sample of each particle's location:

$$T_i(x_0, y_0) = \min\left\{\frac{L_i(x_0, y_0)}{u_{i//}(x_0, y_0)}, T\right\}. \quad (3b)$$

A variate λ is set to represent the absorption capacity of light in the unit time of a single contrast agent particle. After that, the time-weighted gray-scale value of the i -th particle at pixel (x_0, y_0) , $p_i(x_0, y_0)$, can be expressed by the following equation:

$$p_i(x_0, y_0) = \lambda \cdot T_i(x_0, y_0). \quad (3c)$$

On combination of Equations (3a)–(3c), $\overline{v_{b,j}}(x_0, y_0)$ can be characterized by the sum of the time integral intensities of particles which have appeared in pixel (x_0, y_0) during the cardiac cycle, as shown in the following equation:

$$\begin{aligned} \sum_{i=1}^{N(x_0, y_0)} p_i(x_0, y_0) &= \lambda \cdot \sum_{i=1}^{N(x_0, y_0)} T_i(x_0, y_0) \\ &= \lambda \cdot N(x_0, y_0) \cdot \frac{\overline{L}(x_0, y_0)}{\overline{v_{b,j}}(x_0, y_0)}, \end{aligned} \quad (3d)$$

where \overline{L} is the average moving distance of the contrast agent particles within that pixel. Since the size of a pixel is small, \overline{L} is approximately equal to the length of each pixel, L_{pixel} . According to Equations (1a) and (3d), when the frame rate M tends to infinity, the following equation can be obtained:

$$\begin{aligned} \sum_{i=1}^{N(x_0, y_0)} p_i(x_0, y_0) &= \sum_{i=1}^{N(x_0, y_0)} (\lambda \times T_i(x_0, y_0)) \\ &= k \times \sum_{j=0}^{M-1} (N_j(x_0, y_0) \times \Delta t) \\ &= \sum_{j=0}^{M-1} (w_j(x_0, y_0) \times \Delta t) \\ &\equiv b(x_0, y_0), \quad \text{when } M \rightarrow +\infty \text{ and } \Delta t \\ &= \frac{T}{M} \rightarrow 0. \end{aligned} \quad (3e)$$

Equation (3e) demonstrates that the overall time-domain integration value of pixel (x_0, y_0) , $b(x_0, y_0)$, can be expressed as the integral of each picture's gray value at that position in the entire cardiac cycle. On consideration that the time step Δt is short in the actual case, Equation (3e) can be employed in the calculation of the captured DSA images. Therefore, the relationship shown in Equation (3f) can be established. And the image \mathbf{b} is named after the time-domain integration image or the TDI image:

$$\begin{aligned} b(x_0, y_0) &= \sum_{j=0}^{M-1} (w_j(x_0, y_0) \times \Delta t) \\ &= \lambda \times L_{\text{pixel}} \times \frac{N(x_0, y_0)}{\overline{v_{c,j}}(x_0, y_0)} \\ &= \sum_{j=0}^{M-1} (W_j(x_0, y_0) \times \Delta t). \end{aligned} \quad (3f)$$

Furthermore, to strength the denoising effect, the images are denoised by the median filter before the time-domain integration since Ling's work [21] shows that the noiseless image is usually insensitive to a median filter. Table 1 shows the specific steps of our method.

TABLE 1: The image time-domain iteration method.

1. Delineate the region-of-interest
2. Extract the images in the first cardiac cycle after the contrast agent enters the region-of-interest
3. Image denoising with the median filter
4. Extract the time-weighted image, $\mathbf{p}_i: \mathbf{p}_i = \mathbf{W}_j \times \Delta t_j$
5. Image time-domain integration, $\mathbf{b} = \sum_{j=0}^{M-1} \mathbf{p}_i$
6. Extract the TDI image in the region-of-interest

3. Results

Figure 1 shows a group of DSA images from a patient with aortic dissection. Figures 1(a1)–1(c1) are the DSA images at $t = 1/6T$, $1/2T$, and $5/6T$, respectively. Figure 1(d1) is the TDI image of the dissecting aneurysm extracted by our algorithm. For the sake of comparison, the image of dissecting aneurysm region in Figures 1(a1)–1(c1) are extracted and then the normalized gray-scale histograms of dissecting aneurysm regions among Figures 1(a1)–1(d1) are obtained, which are shown in Figures 1(a2)–1(d2), respectively. Table 2 shows the mean value, standard deviation, and coefficient of variation of DSA images of the dissecting aneurysm region in one cardiac cycle of the patient in Figure 1.

Table 2 shows that the coefficient of variation of the TDI image is higher than all the DSA images in that cardiac cycle, which means that our TDI image can enhance the details. Moreover, the gap between the peaks in Figure 1(d2) is clearer than those in Figures 1(a2)–1(c2), which means that our TDI image has higher resolution than the original images.

4. Discussion

Since the blood flow velocity has a certain degree of uncertainty in the actual situation, which directly influenced the gray-scale value of the shot DSA image, Equation (1c) can be rewritten as follows:

$$\mathbf{W}_j = \mathbf{w}_j \cdot \mathbf{H}_j + \mathbf{n}_j = ((\mathbf{q}_j + \Phi_j) \cdot \mathbf{H}_j) + \mathbf{n}_j, \quad (4)$$

where \mathbf{q}_j donates the gray-scale value after the removal of motion randomness.

Equations (3f) and (4) illustrate that the time-domain integration image \mathbf{b} can be obtained by the following equation:

$$\begin{aligned} \mathbf{b} &= \Delta t \times \left(\sum_{j=0}^{M-1} \mathbf{W}_j \right) = \Delta t \times \left(\sum_{j=0}^{M-1} ((\mathbf{q}_j + \Phi_j) \cdot \mathbf{H}_j) + \sum_{j=0}^{M-1} \mathbf{n}_j \right) \\ &= \Delta t \times \left(\sum_{j=0}^{M-1} (\mathbf{q}_j + \mathbf{G}_j) \right), \end{aligned} \quad (5a)$$

where matrix \mathbf{G}_j is defined to characterize the differences between \mathbf{W}_j and \mathbf{q}_j . A new symbol \mathbf{b}_x is defined here, which represents the noise-free time-domain integration image. $\mathbf{b}_x = \sum_{j=0}^{M-1} \mathbf{q}_j$. Then, the error analysis of Equation (5a) is implemented below.

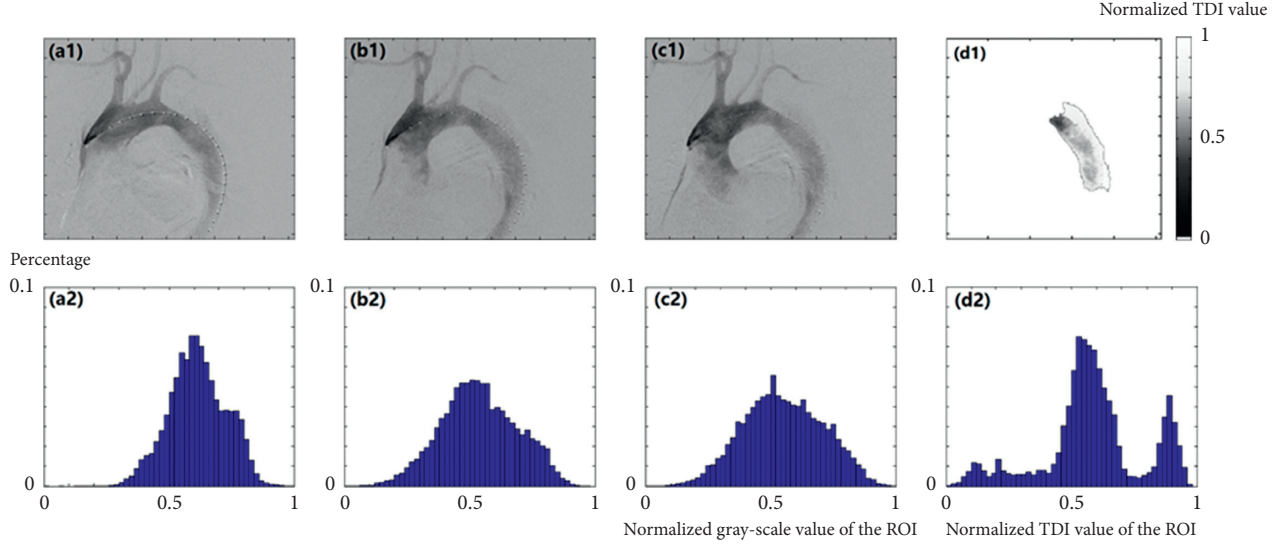


FIGURE 1: A set of DSA images from a patient.

TABLE 2: The mean value, standard deviation, and coefficient of variation of DSA images of the aortic dissection for the patient in Figure 1 in the first cardiac cycle after the contrast agent enters the aortic dissection.

Time	0	1/6T	1/3T	1/2T	2/3T	5/6T	T	TDI image
Mean	0.6794	0.6340	0.6948	0.6507	0.6958	0.5965	0.5978	0.6025
Standard deviation	0.3585	0.3452	0.3473	0.3554	0.3430	0.3784	0.3835	0.4425
Coefficient of variation (%)	52.77	54.44	49.98	54.62	49.30	63.44	64.15	73.44

$$v_{\text{inlet}}(t) = \begin{cases} 2.4e^{-7.557t} \sin(13.09t), & 0 \leq t \leq 0.24, \\ -0.343e^{-7.557(t-0.24)} \times \sin(13.09(t-0.24)) \text{ (m/s)}, & 0.24 < t < 0.2743 \text{ (s)}, \\ 0, & 0.2743 < t \leq 0.8, \end{cases} \quad (5b)$$

$$\frac{1}{M} \times \sum_{j=0}^{M-1} \left(\frac{G_j(x_0, y_0)}{q_j(x_0, y_0)} \right)^2 \geq \left(\frac{\Delta t \times \sum_{j=0}^{M-1} G_j(x_0, y_0)}{\Delta t \times \sum_{j=0}^{M-1} q_j(x_0, y_0)} \right)^2 = \left(\frac{b(x_0, y_0) - b_x(x_0, y_0)}{b_x(x_0, y_0)} \right)^2, \quad (5c)$$

$$\left\| \lim_{M \rightarrow +\infty} \left(k \times \sum_{j=0}^{M-1} \left(N_j \times \frac{T}{M} \right) \right) - \mathbf{b} \right\|_2 < \left\| \lim_{M \rightarrow +\infty} \left(k \times \sum_{j=0}^{M-1} \left(N_j \times \frac{T}{M} \right) \right) - \mathbf{W}_j \times T \right\|_2. \quad (5d)$$

According to Reference [22], when the cardiac cycle length is 0.8 seconds, the blood flow rate at the aortic inlet, denoted by v_{inlet} , follows Equation (5b). The first part of Equation (5b) denotes the ejection phase, which is followed by a brief closure of blood after the closure of the aortic valve. The flow rate in the rest time is 0. Since the time varies when each particle enters the view field, the time when they arrive at the same position on the image also varies. Therefore, the number of images which satisfy $N_j(x, y) \neq 0$ is greater than one in most positions. Thus, Equation (5c) can be obtained.

According to Equation (5c), the signal-to-noise ratio of image \mathbf{b} (\mathbf{b}_x is defined as the noise-free image in this calculation) is higher than the mean signal-to-noise ratio of original DSA images at each pixel. Therefore, the result of

our method contains lower noise in the entire view field, and our method can suppress the noise.

Furthermore, Equation (5d) can be deduced from Equation (3e), where $\|\cdot\|_2$ stands for the two-norm of matrix. According to Equation (5d), image \mathbf{b} is closer to the noise-free TDI image \mathbf{b}_x than all of the DSA images, which means that image \mathbf{b} has the highest clarity. Thus, the image \mathbf{b} can improve the clarity of the original DSA images.

5. Conclusion

In summary, this study presents a DSA image denoising and enhancement method based on the periodicity of blood flow. Firstly, the DSA images are reconstructed through the median

filter, and then DSA images in a cardiac cycle are integrated and the overall time-domain integration image **b** is obtained. According to the mathematical derivation as well as the verification using aortic dissecting aneurysm images, this study demonstrates that the TDI image of the contrast agent has a lower overall noise than original DSA images, and it is also clearer than the original image. This method can contribute to the feature location extraction and disease prophylaxis in circulatory disease, such as the first break's position extraction of aortic dissecting aneurysms and the analysis of stress distribution on vessel wall [23], which are also our future work.

Data Availability

The data used to support the findings of this study are available from the corresponding author upon request.

Conflicts of Interest

The authors declare that they have no conflicts of interest.

Authors' Contributions

Shuo Huang and Le Cheng contributed equally to this work.

Acknowledgments

This work was supported by the National Key R&D Program of China under grant number 2017YFC0112801, the National Natural Science Foundation of China under grant numbers 61127002, 11572087, 61771130, and 31300780, the Research Center for Learning Science of Southeast University under grant number 3207038391, and the School of Biological Sciences and Medical Engineering under grant number 3207037434.

References

- [1] R. Erbel, F. Alfonso, C. Boileau et al., "Diagnosis and management of aortic dissection: recommendations of the task force on aortic dissection, European society of cardiology," *European Heart Journal*, vol. 22, no. 18, pp. 1642–1681, 2001.
- [2] A. White, J. Broder, J. Mando-Vandrick, J. Wendell, and J. Crowe, "Acute aortic emergencies—part 2: aortic dissections," *Advanced Emergency Nursing Journal*, vol. 35, no. 1, pp. 28–52, 2013.
- [3] J. O. Balzer, M. Doss, A. Thalhammer, H.-G. Fieguth, A. Moritz, and T. J. Vogl, "Urgent thoracic aortal dissection and aneurysm: treatment with stent-graft implantation in an angiographic suite," *European Radiology*, vol. 13, no. 10, pp. 2249–2258, 2003.
- [4] E. Sueyoshi, H. Nagayama, I. Sakamoto, and M. Uetani, "Carbon dioxide digital subtraction angiography as an option for detection of endoleaks in endovascular abdominal aortic aneurysm repair procedure," *Journal of Vascular Surgery*, vol. 61, no. 2, pp. 298–303, 2015.
- [5] S. Osher and J. A. Sethian, "Fronts propagating with curvature-dependent speed: algorithms based on Hamilton-Jacobi formulations," *Journal of Computational Physics*, vol. 79, no. 1, pp. 12–49, 1988.
- [6] S. Wan, B. I. Raju, and M. A. Srinivasan, "Robust deconvolution of high-frequency ultrasound images using higher-order spectral analysis and wavelets," *IEEE Transactions on Ultrasonics, Ferroelectrics and Frequency Control*, vol. 50, no. 10, pp. 1286–1295, 2003.
- [7] S. G. Mallat, "Multifrequency channel decompositions of images and wavelet models," *IEEE Transactions on Acoustics, Speech, and Signal Processing*, vol. 37, no. 12, pp. 2091–2110, 1989.
- [8] M. Lebrun, A. Buades, and J. M. Morel, "A nonlocal bayesian image denoising algorithm," *SIAM Journal on Imaging Sciences*, vol. 6, no. 3, pp. 1665–1688, 2013.
- [9] P. Perona and J. Malik, "Scale-space and edge detection using anisotropic diffusion," *IEEE Transactions on Pattern Analysis and Machine Intelligence*, vol. 12, no. 7, pp. 629–639, 1990.
- [10] E. J. Candes, J. Romberg, and T. Tao, "Robust uncertainty principles: exact signal reconstruction from highly incomplete frequency information," *IEEE Transactions on Information Theory*, vol. 52, no. 2, pp. 489–509, 2004.
- [11] D. Needell and R. Vershynin, "Uniform uncertainty principle and signal recovery via regularized orthogonal matching pursuit," *Foundations of Computational Mathematics*, vol. 9, no. 3, pp. 317–334, 2009.
- [12] A. Scholefield and P. L. Dragotti, "Image restoration using a sparse quadtree decomposition representation," in *Proceedings of 2009 IEEE International Conference on Image Processing*, pp. 1473–1476, IEEE, Cairo, Egypt, November 2009.
- [13] A. Adler, Y. Hel-Or, and M. Elad, "A shrinkage learning approach for single image super-resolution with over-complete representations," in *Proceedings of 2010 European Conference on Computer Vision*, pp. 622–635, Springer Berlin Heidelberg, Crete, Greece, September 2010.
- [14] M. Elad, M. A. T. Figueiredo, and Y. Ma, "On the role of sparse and redundant representations in image processing," *Proceedings of the IEEE*, vol. 98, no. 6, pp. 972–982, 2010.
- [15] D. Needell and R. Vershynin, "Signal recovery from incomplete and inaccurate measurements via regularized orthogonal matching pursuit," *IEEE Journal of Selected Topics in Signal Processing*, vol. 4, no. 2, pp. 310–316, 2010.
- [16] J. L. Starck, J. M. Fadili, and C. Chesneau, "Image deconvolution by stein block thresholding," in *Proceedings of 2009 IEEE International Conference on Image Processing*, pp. 1329–1332, Cairo, Egypt, November 2009.
- [17] D. Tzikas, A. Likas, and N. Galatsanos, "Variational bayesian blind image deconvolution with student-T priors," in *Proceedings of 2007 IEEE International Conference on Image Processing*, pp. I-109–I-112, San Antonio, TX, USA, September 2007.
- [18] M. Elizabeth, *Concise Medical Dictionary*, Oxford University Press, Oxford, UK, 2015.
- [19] W. D. Jeans, "The development and use of digital subtraction angiography," *British Journal of Radiology*, vol. 63, no. 747, pp. 161–168, 1990.
- [20] C. R. Wilke and P. Chang, "Correlation of diffusion coefficients in dilute solutions," *AIChE Journal*, vol. 1, no. 2, pp. 264–270, 1955.
- [21] J. Ling and A. C. Bovik, "Smoothing low-SNR molecular images via anisotropic median-diffusion," *IEEE Transactions on Medical Imaging*, vol. 21, no. 4, pp. 377–384, 2002.
- [22] C. Y. Wen, A. L. Yang, and J. W. Chai, "Investigation of pulsatile flow field in healthy thoracic aorta models," *Annals of Biomedical Engineering*, vol. 38, no. 2, pp. 391–402, 2010.
- [23] J. Charonko, S. Karri, J. Schmiege, S. Prabhu, and P. Vlachos, "In vitro comparison of the effect of stent configuration on wall shear stress using time-resolved particle image velocimetry," *Annals of Biomedical Engineering*, vol. 38, no. 3, pp. 889–902, 2010.

Research Article

Analysis of Exercise-Induced Periodic Breathing Using an Autoregressive Model and the Hilbert-Huang Transform

Tieh-Cheng Fu,^{1,2,3} Chaur-Chin Chen,⁴ Ching-Mao Chang ^{5,6}
Hen-Hong Chang ^{7,8} and Hsueh-Ting Chu ^{9,10}

¹ Department of Physical Medicine and Rehabilitation, Chang Gung Memorial Hospital, Keelung, Taiwan

² Heart Failure Center, Department of Internal Medicine, Chang Gung Memorial Hospital, Keelung, Taiwan

³ College of Medicine, Chang Gung University, Tao-Yuan, Taiwan

⁴ Department of Computer Science, National Tsing Hua University, Hsinchu, Taiwan

⁵ Center for Traditional Medicine, Taipei Veterans General Hospital, Taipei, Taiwan

⁶ Faculty of Medicine, National Yang-Ming University, Taipei, Taiwan

⁷ School of Post-Baccalaureate Chinese Medicine, College of Chinese Medicine, Research Center for Chinese Medicine & Acupuncture, China Medical University, Taichung, Taiwan

⁸ Department of Chinese Medicine, China Medical University Hospital, Taichung, Taiwan

⁹ Department of Computer Science and Information Engineering, Asia University, Taichung, Taiwan

¹⁰ Department of Department of Medical Research, China Medical University Hospital, China Medical University, Taichung, Taiwan

Correspondence should be addressed to Ching-Mao Chang; magicbjp@gmail.com and Hsueh-Ting Chu; htchu.taiwan@gmail.com

Received 27 February 2018; Accepted 21 May 2018; Published 26 June 2018

Academic Editor: Dominique J. Monlezun

Copyright © 2018 Tieh-Cheng Fu et al. This is an open access article distributed under the Creative Commons Attribution License, which permits unrestricted use, distribution, and reproduction in any medium, provided the original work is properly cited.

Evaluation of exercise-induced periodic breathing (PB) in cardiopulmonary exercise testing (CPET) is one of important diagnostic evidences to judge the prognosis of chronic heart failure cases. In this study, we propose a method for the quantitative analysis of measured ventilation signals from an exercise test. We used an autoregressive (AR) model to filter the breath-by-breath measurements of ventilation from exercise tests. Then, the signals before reaching the most ventilation were decomposed into intrinsic mode functions (IMF) by using the Hilbert-Huang transform (HHT). An IMF represents a simple oscillatory pattern which catches a part of original ventilation signal in different frequency band. For each component of IMF, we computed the number of peaks as the feature of its oscillatory pattern denoted by Δ_i . In our experiment, 61 chronic heart failure patients with or without PB pattern were studied. The computed peaks of the third and fourth IMF components, Δ_3 and Δ_4 , were statistically significant for the two groups (both p values < 0.02). In summary, our study shows a close link between the HHT analysis and level of intrinsic energy for pulmonary ventilation. The third and fourth IMF components are highly potential to indicate the prognosis of chronic heart failure.

1. Introduction

The rehabilitation of patients with chronic heart failure (CHF) is a slow process, and sometimes, good progress is difficult to obtain for some patients. Exercise-induced periodic breathing (EPB) was found to be an important evidence of poor prognosis [1–6]. Therefore, physiatrists commonly check exercise breathing patterns of patients with CHF by using cardiopulmonary exercise testing (CPET; Figure 1(a)) to guide the pharmacological and nonpharmacological

treatments for these patients. CPET involves measurements of ventilation (VE) respiratory oxygen uptake (VO_2) and carbon dioxide production (VCO_2) during a symptom-limited exercise test [7]. On increasing the bicycle workload during a CPET test, the respiratory exchange rate and tidal volume increase simultaneously. For more respiratory exchanges, a periodic breathing (PB) pattern might occur in some patients with CHF. PB (Figure 1(d)), first described in the 1970s [8], is a phenomenon of abnormal hyperventilation that alternates apneas and hypopneas. In this study, we investigated the

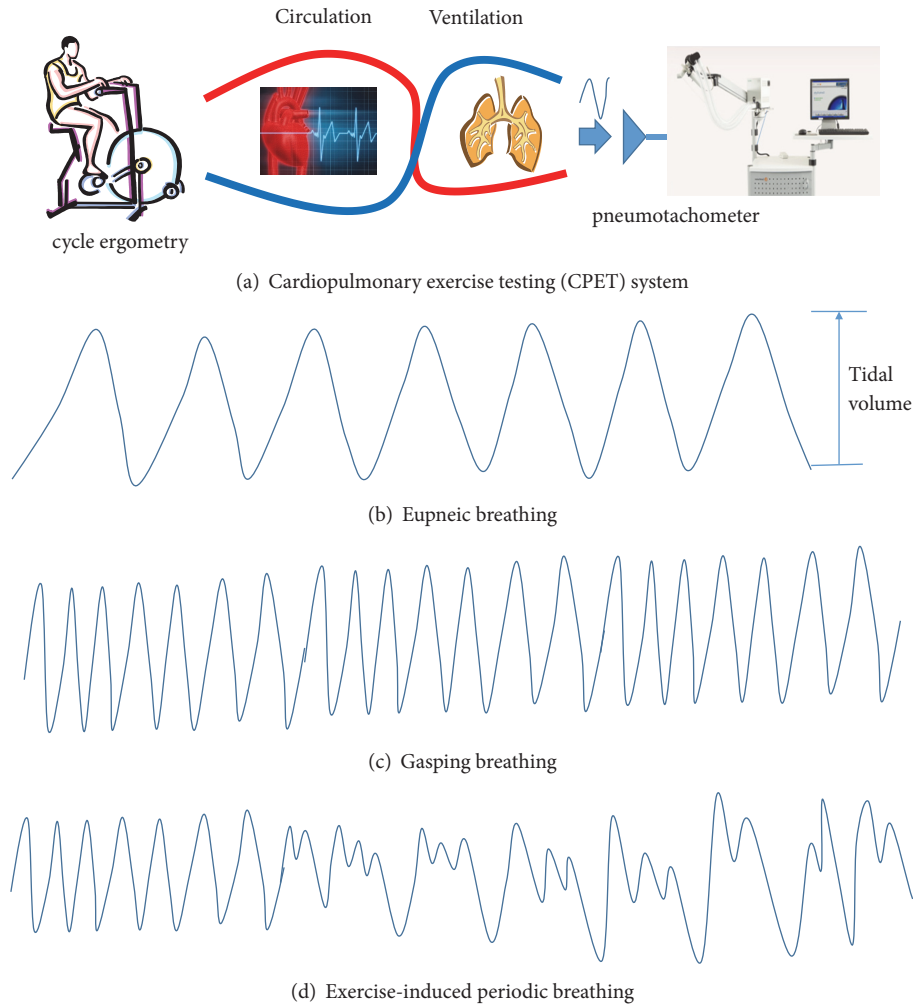


FIGURE 1: **A cardiopulmonary exercise testing (CPET) system and breathing patterns.** (a) A CPET machine is comprised of a cycle ergometer and pneumotachometer. During the test, the bicycle workload for the patient is increased until maximal exertion is reached. (b–d) Breathing patterns include eupneic, gasping, and periodic breathing (PB). Tidal volume is the volume of air exchange between inhalation and exhalation.

difference in ventilation signals between PB and non-PB patients [9].

From the analysis of cardiopulmonary exercise testing (CPET) measurements, two significant indicators have been studied in the literature, namely, peak VO_2 and VE/VCO_2 slope. Peak oxygen consumption (peak VO_2) was considered the gold standard assessment parameter of prognosis in CHF [10, 11]. Then, the ratio of ventilation-to-carbon dioxide production (VE/VCO_2 slope) was also studied later with the same importance as peak VO_2 [12, 13]. More recently, the quantification of PB patterns was investigated in both the spatial and frequency domains [3–5]. Here, we endeavored to link CPET measurements and the quantification of PB patterns by using the Hilbert-Huang transform (HHT) [14]. The Hilbert-Huang transform has been applied in many biomedical analyses [15], including blood pressure [16, 17], nasal flow [18], and electroencephalography [19, 20]. To apply the Hilbert-Huang transform on the analysis of ventilation

measurements, we propose two important steps of preprocessing. In the first step, we examine the ventilation measurements from CPET tests. Some ventilation measurements are noisy and aberrant when the testing patient is gasping. The occurrence of such aberrant signals is caused by the limitation of a CPET system. The ventilation VE values are obtained from breath-by-breath calculation of gas exchange at the mouth. A nonrebreathing valve is connected to a mouthpiece to prevent mixing of inspired and expired air. Thus, one irregular gasping exhalation may be recorded as two or more breaths. As a result, we filter out those aberrant measurements.

Moreover, not all measurements from entire CPET tests were used in our analysis. To determine the meaningful difference in cardiopulmonary response between the PB and non-PB patients, we only selected the period before the patient's ventilation reached the maximal volume. The common respiratory rate for an adult at rest is 12–20 breaths per

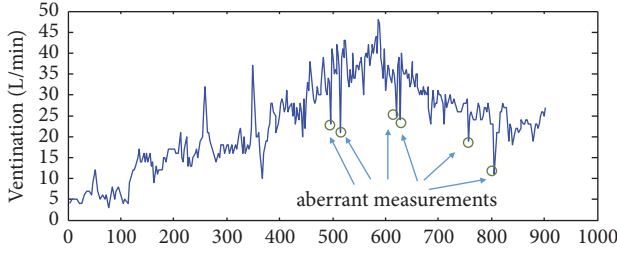


FIGURE 2: Measured signals of exercise breath-by-breath ventilation. Very low measurements usually occur when the patient is gasping. In this study, when the ventilation volume was high, these exceptional measurements were observed as noises.

minute, which will increase up to 30–50 breaths per minute during exercise testing. Thus, PB patterns are most likely to appear around the peak respiratory volume. Therefore, 200 ventilation measurements, that is, a period of 4–6 minutes before the peak volume, were used in the analysis.

2. Materials and Methods

2.1. Breath-by-Breath Ventilation Signals for 61 Patients with Chronic Heart Failure. Exercise ventilation signals were recorded from CHF patients who received rehabilitation at the Chang Gung Memorial Hospital-Keelung Branch in Taiwan. All the subjects were studied in accordance with a protocol previously approved by the local ethics committee and registered at the ClinicalTrials.gov website with ID No. NCT01053091. The respiratory signals were acquired using a pneumotachometer connected to a mask and analyzed using the machine MasterScreen CPX Metabolic Cart. In common cases, the signals, including VO_2 and VCO_2 , are output per 30 seconds, although they are measured breath by breath. More information about the collected CPET data can be found in Fu et al. (2017). For this study, we output the original breath-by-breath signals of ventilation instead. The total measurement period was 10–15 minutes. We obtained 61 deidentified ventilation samples marked as PB ($n = 20$) or non-PB ($n = 41$) by physiatrists.

2.2. Filtering of Ventilation by an Autoregressive Model. Many observations of biosignal series exhibit serial autocorrelation and can be modelled with autoregressive (AR) models. Garde *et al.* showed that ventilation signals can also be fitted by AR models [18]. They used the coefficients of AR models to characterize the respiratory pattern of PB or non-PB patients. However, the average ventilation measurements per minute were adapted in their study. In our study, we analyzed breath-by-breath signals and applied the AR model method to fit the curve of exercise ventilation as shown in Figure 2.

The AR models predict y_t as a function of past observations, $y_{t-1}, y_{t-2}, \dots, y_{t-p}$. The form of the AR model is

$$\bar{y}_t = c + \phi_1 y_{t-1} + \dots + \phi_p y_{t-p}, \quad (1)$$

where p is the degree of the AR model and denoted by $AR(p)$ and \bar{y}_t is the predicted term.

For the analysis of PB or non-PB exercise ventilation, 200 serial measurements before the largest ventilation volume were chosen, and an $AR(6)$ model is applied to the series. By using the equation to fit the exercise ventilations, we filtered out the observed measurement of ventilation y_t if $y_t < 0.8\bar{y}_t$. This filtered series of ventilation signals is called “the most exhausted exercise ventilations (MEE-Ve)” in this paper.

2.3. Decomposition of the Chosen Ventilation Signals by the Hilbert-Huang Transform. The Hilbert-Huang transform (HHT) is a signal decomposition method developed by Norden E. Huang in the 1990s [14]. By using this processing method, biosignals are decomposed into a set of IMFs by an empirical mode decomposition (EMD) process. The instantaneous frequencies and amplitudes of all IMFs can be used to identify embedded signal structures.

The HHT representation of series $X(t)$ is

$$X(t) = \Re \sum_{j=1}^n a_j(t) e^{i\theta_j(t)} = \Re \sum_{j=1}^n [C_j(t) + iY_j(t)], \quad (2)$$

where $C_j(t)$ and $Y_j(t)$ are, respectively, the j -th IMF component of $X(t)$.

To obtain IMFs, EMD [14], which is an iterative process that output a set of signal components called IMFs, is performed. Figure 3 shows an example of decomposed IMFs for a series of MEE-Ve. The original signals are decomposed into the components $IMF_1, IMF_2, \dots, IMF_5$. Different IMF components may imply particular factors. We calculated the peaks of the oscillations in each IMF with MATLAB’s “mspeaks” function [21]. The estimated peaks of the IMF components of IMF_i are denoted as Δ_i to compare the PB and non-PB samples.

2.4. Statistical Analyses. Student’s t -tests were used to identify statistically significant differences between two groups of features of PB and non-PB samples.

3. Results

3.1. The Computation of IMFs of Most Exhausted Exercise Ventilations (MEE-Ve) for PB and Non-PB Patients. The measurements of ventilation (VE) obtained from cardiopulmonary exercise testing (CPET) were analyzed using the proposed method. The programs were written in MATLAB. We analyzed the extracted exercise ventilations in this section by using HHT for 20 patients with or without PB as judged by physiatrists. The empirical mode decomposition (EMD) process is applied to the VE data and several IMFs are extracted. Figure 3 depicts the HHT decomposition result for IMF_1 - IMF_5 . In addition, we show the corresponding instantaneous frequency of the decomposed IMF_1 - IMF_4 in Figure 4. All figures of HHT decomposition results for the 61 patients are available at our Github repository (<https://github.com/htchu/EpbAnalysis>).

3.2. Numbers of Peaks as the Features of IMFs. We used MATLAB’s “mspeaks” function to perform the peak fitting of IMFs and the source ventilations. Figure 5 illustrates

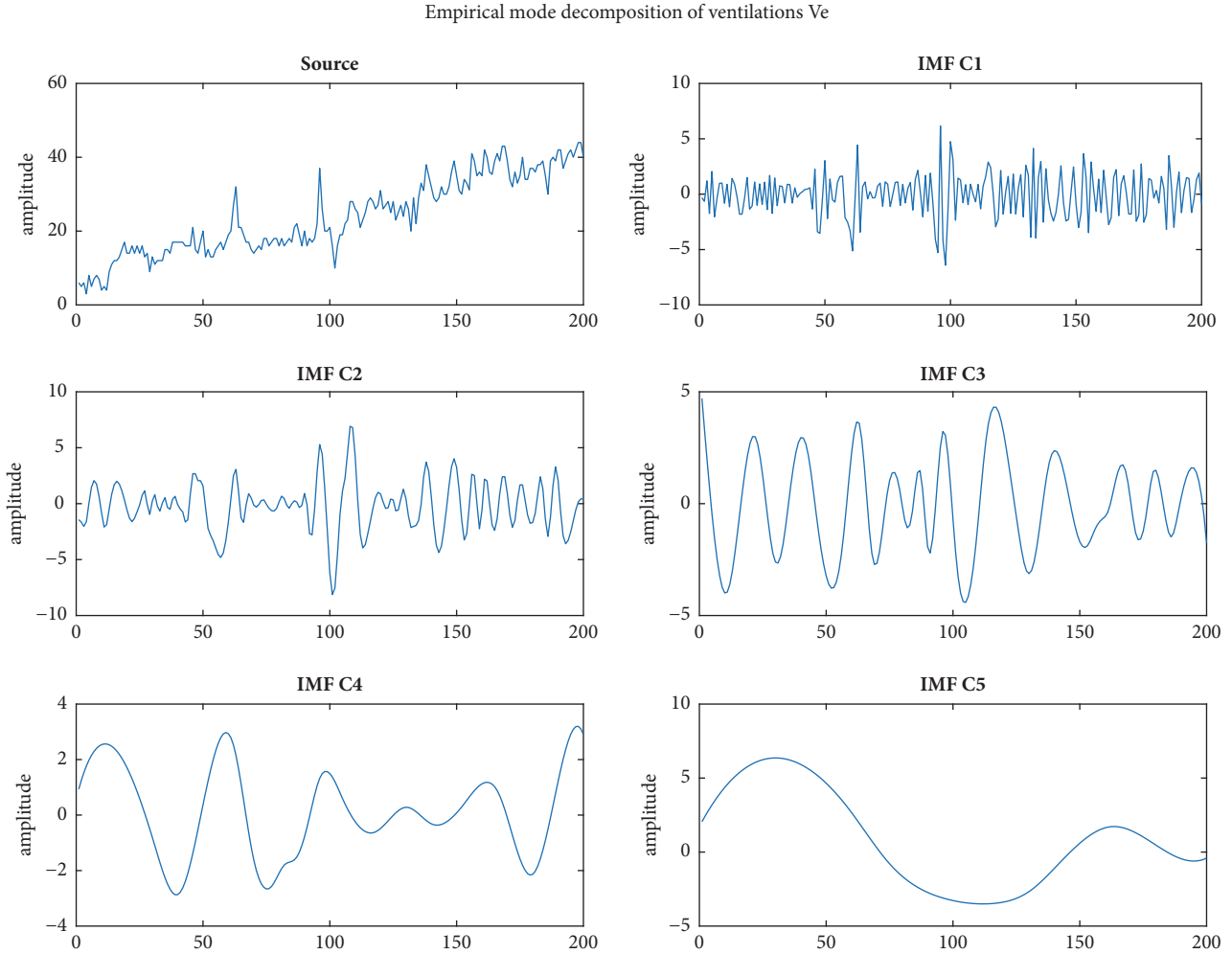


FIGURE 3: An example of empirical mode decomposition of most exhausted exercise ventilations (MEE-Ve). The MEE-Ve signals are k ventilations before the peak volume. The number k is 200 in this paper. The illustration is from the analysis of the patient ID: pb0001 which was judged as a periodic breathing (PB) case. All results of the EMD analysis for the PB or non-PB cases can be found at the Github repository (<https://github.com/htchu/EpbAnalysis>).

the computed locations of peaks for the same experimental data in Figure 3. Obviously, the peak fittings for the source ventilations and the first IMF (Figures 5(a) and 5(b)) are not as good as the peak fittings for the other IMFs (Figures 5(c)–5(f)). Table 1 lists the numbers of computed peaks of IMF_1 – IMF_5 for first 20 patients (10 PBs and 10 non-PBs). Supplemental Table 1 provides all of the computed peaks for the entire test dataset.

3.3. Statistical Significance Test of IMFs. The statistical significance test derived by Wu and Huang [22] is illustrated in Figure 6. The five extracted IMFs are shown along with the 95% and 99% confidence limits. All IMFs are above the 99-percentile confidence limit except for the IMF_5 . Therefore, only the IMF_5 is not statistically significant from noise [22].

3.4. More Peaks of IMF_3 and IMF_4 for Better Prognosis of Chronic Heart Failure Cases. Student's t-tests were used to

identify statistically significant differences between the two groups (PB and non-PB patients). Table 2 lists the p values for the comparison between the two groups for the computed peaks of IMFs. The p values for first two IMFs are greater than 0.1 such that the peak computations are not statistically significant for IMF_1 and IMF_2 . By contrast, the p values for IMF_3 and IMF_4 are less than 0.02 such that the peak computations are statistically significant for IMF_3 and IMF_4 .

4. Discussion and Conclusion

This paper conducted a new analysis on exercise ventilation signals to predict the prognosis of CHF patients. We defined MEE-Ve as a breath-by-breath ventilation measurement filtered using an AR model. We ran our correlation analysis through IMFs, extracted from the EMD process, and found that PB patterns were highly correlated to IMF_3 and IMF_4 . To clarify the correlation, we introduced peak computation of

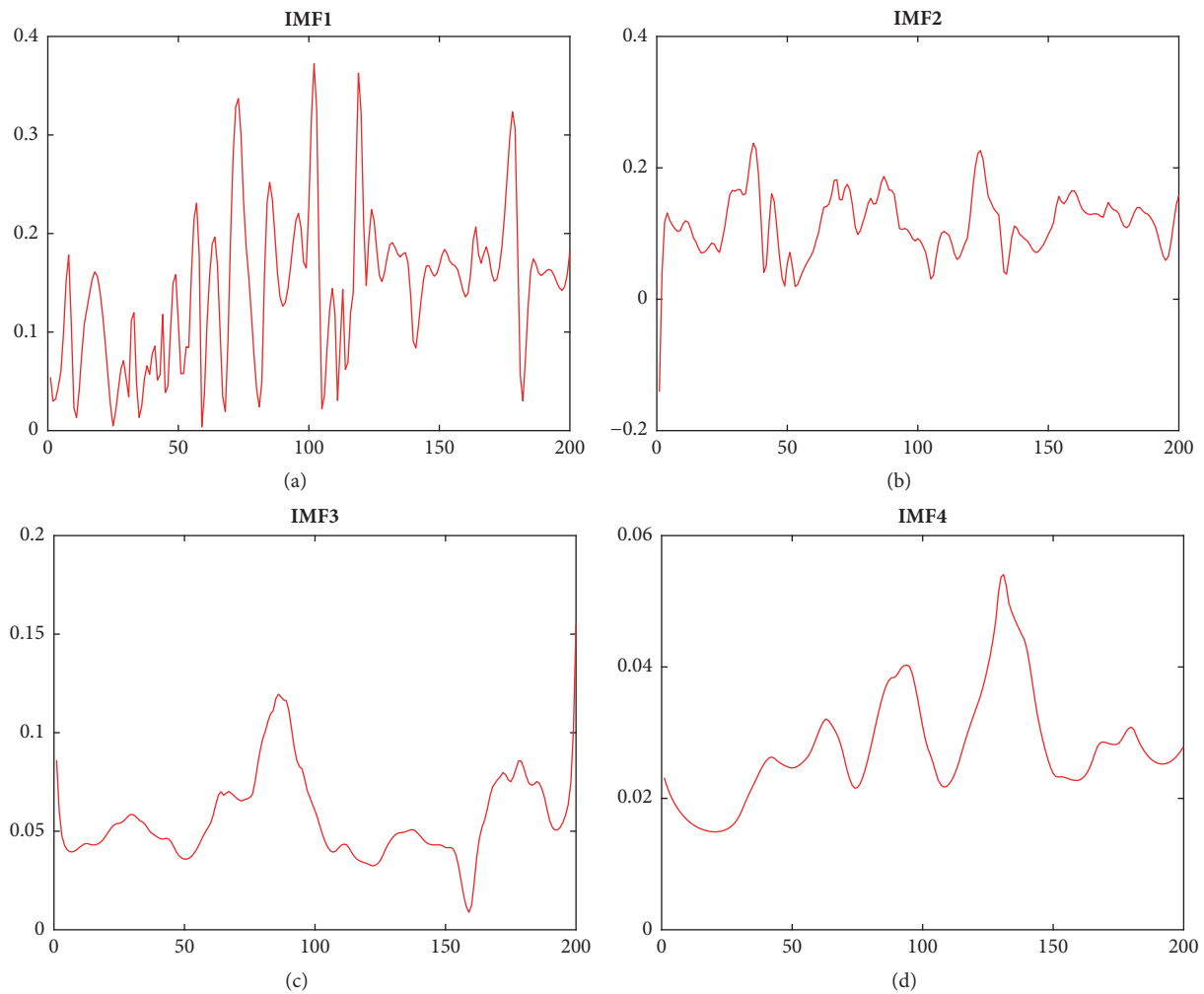


FIGURE 4: The corresponding instantaneous frequency of the decomposed IMF_1 - IMF_4 (Figure 3).

IMF_3 and IMF_4 (Δ_3, Δ_4) as the feature of ventilation signals from cardiopulmonary exercise testing (CPET).

However, the effectiveness of the proposed method needs more clinical examinations in the future. Meanwhile, the range selection of exercise ventilations is another issue for more studies. We plan to examine this method with more cardiopulmonary tests.

Data Availability

The MATLAB programs and EPB data of this work are available at <https://github.com/htchu/EpbAnalysis/>.

Disclosure

A preliminary study of the article had been presented in the conference ICS2014 (<http://ics2014.thu.edu.tw/>).

Conflicts of Interest

The authors declare no conflicts of interest.

Authors' Contributions

Tieh-Cheng Fu and Hsueh-Ting Chu coordinated the project and prepared the test dataset. The programs were written by Chaur-Chin Chen and Hsueh-Ting Chu. Hsueh-Ting Chu, Chaur-Chin Chen, Tieh-Cheng Fu, Hen-Hong Chang, and Ching-Mao Chang discussed the project and jointly wrote the manuscript. Ching-Mao Chang and Tieh-Cheng Fu interpreted the analysis results.

Acknowledgments

This work is supported by the Ministry of Science and Technology, Taiwan, under Grant no. 102-2628-B-182A-001-MY3, and Chang Gung Medical Research Program (CMRPG2A0162 and CMRPG2C0402).

Supplementary Materials

Supplemental Table 1: computed peaks for the decomposed intrinsic mode functions (IMFs) from exercise ventilation

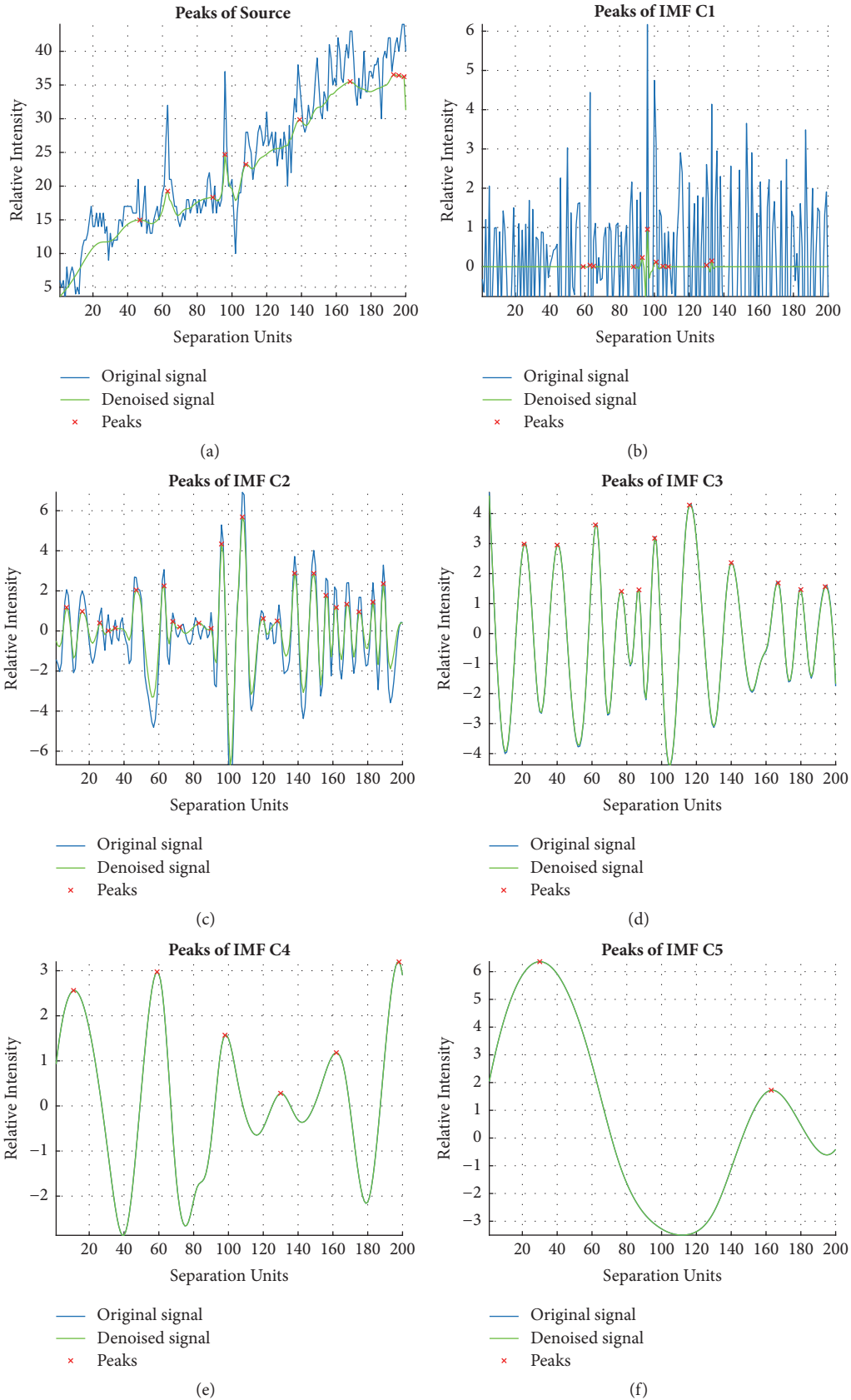


FIGURE 5: Peak Computations of IMFs (Figure 3).

TABLE 1: Computed peaks Δ_i of IMFs by mspeaks.

PB or non-PB Patient	Δ_1	Δ_2	Δ_3	Δ_4	Δ_5
PB-1	11	23	11	6	2
PB-2	2	28	17	7	3
PB-3	11	29	13	5	2
PB-4	9	30	13	7	3
PB-5	14	27	14	4	2
PB-6	8	25	13	5	2
PB-7	0	28	14	6	3
PB-8	21	25	16	8	3
PB-9	0	30	15	7	3
PB-10	3	23	9	5	2
nPB-1	7	26	16	6	3
nPB-2	7	29	15	8	2
nPB-3	8	28	16	9	4
nPB-4	2	24	14	7	3
nPB-5	4	28	17	10	5
nPB-6	0	30	17	7	5
nPB-7	15	26	15	6	2
nPB-8	8	27	15	7	3
nPB-9	9	26	16	8	4
nPB-10	2	31	17	8	3

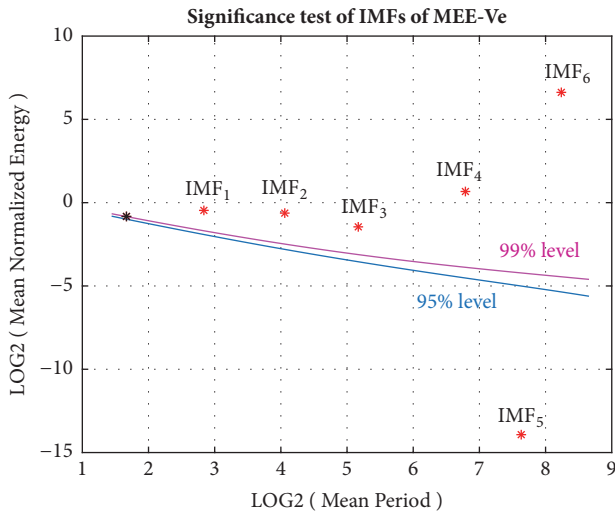


FIGURE 6: Statistical significance test for the decomposed IMFs. The IMF_5 is below the 95% confidence limit and is therefore considered statistically insignificant.

TABLE 2: P values of Student’s t-test for IMFs.

IMF component	Δ_1	Δ_2	Δ_3	Δ_4
P value	0.6330	0.1103	0.016	0.017

signals of 61 chronic heart failure patients. (Supplementary Materials)

References

- [1] P. Agostoni, U. Corrà, and M. Emdin, “Periodic breathing during incremental exercise,” *Annals of the American Thoracic Society*, vol. 14, pp. S116–S122, 2017.
- [2] B. P. Dhakal, R. M. Murphy, and G. D. Lewis, “Exercise Oscillatory Ventilation in Heart Failure,” *Trends in Cardiovascular Medicine*, vol. 22, no. 7, pp. 185–191, 2012.
- [3] J. J. Leite, A. J. Mansur, H. F. G. De Freitas et al., “Periodic breathing during incremental exercise predicts mortality in patients with chronic heart failure evaluated for cardiac transplantation,” *Journal of the American College of Cardiology*, vol. 41, no. 12, pp. 2175–2181, 2003.
- [4] T. P. Olson and B. D. Johnson, “Quantifying oscillatory ventilation during exercise in patients with heart failure,” *Respiratory Physiology & Neurobiology*, vol. 190, no. 1, pp. 25–32, 2014.
- [5] J. P. Ribeiro, “Periodic breathing in heart failure: Bridging the gap between the sleep laboratory and the exercise laboratory,” *Circulation*, vol. 113, no. 1, pp. 9–10, 2006.
- [6] G. Tumminello, M. Guazzi, P. Lancellotti, and L. A. Piérard, “Exercise ventilation inefficiency in heart failure: Pathophysiological and clinical significance,” *European Heart Journal*, vol. 28, no. 6, pp. 673–678, 2007.
- [7] K. Albouaini, M. Egred, A. A. Alahmar, and D. J. Wright, “Cardiopulmonary exercise testing and its application,” *Postgraduate Medical Journal*, vol. 83, no. 985, pp. 675–682, 2007.
- [8] G. Preiss, S. Iscoe, and C. Polosa, “Analysis of a periodic breathing pattern associated with Mayer waves,” *American Journal of Physiology-Endocrinology and Metabolism*, vol. 228, no. 3, pp. 768–774, 1975.

- [9] T. Fu, W. Lin, J. Wang et al., "Detection of exercise periodic breathing using thermal flowmeter in patients with heart failure," *Medical & Biological Engineering & Computing*, vol. 55, no. 8, pp. 1189–1198, 2017.
- [10] G. A. MacGowan and S. Murali, "Ventilatory and heart rate responses to exercise: better predictors of heart failure mortality than peak exercise oxygen consumption.," *Circulation*, vol. 102, no. 24, p. E182, 2000.
- [11] M. Robbins, G. Francis, F. J. Pashkow et al., "Ventilatory and heart rate responses to exercise better predictors of heart failure mortality than peak oxygen consumption," *Circulation*, vol. 100, no. 24, pp. 2411–2417, 1999.
- [12] R. Arena, J. Myers, S. S. Aslam, E. B. Varughese, and M. A. Peberdy, "Peak VO₂ and VE/VCO₂ slope in patients with heart failure: A prognostic comparison," *American Heart Journal*, vol. 147, no. 2, pp. 354–360, 2004.
- [13] F. M. Sarullo, G. Fazio, I. Brusca et al., "Cardiopulmonary exercise testing in patients with chronic heart failure: Prognostic comparison from peak vo₂ and ve/vco₂ slope," *The Open Cardiovascular Medicine Journal*, vol. 4, pp. 127–134, 2010.
- [14] N. E. Huang, Z. Shen, S. R. Long et al., "The empirical mode decomposition and the Hilbert spectrum for nonlinear and non-stationary time series analysis," *Proceedings A*, vol. 454, no. 1971, pp. 903–995, 1998.
- [15] C.-F. Lin and J.-D. Zhu, "Hilbert-Huang transformation-based time-frequency analysis methods in biomedical signal applications," *Proceedings of the Institution of Mechanical Engineers, Part H: Journal of Engineering in Medicine*, vol. 226, no. 3, pp. 208–216, 2012.
- [16] C.-C. Chang, T.-C. Hsiao, and H.-Y. Hsu, "Frequency range extension of spectral analysis of pulse rate variability based on Hilbert-Huang transform," *Medical & Biological Engineering & Computing*, vol. 52, no. 4, pp. 343–351, 2014.
- [17] Q. Zhang, Y. Shi, D. Teng et al., "Pulse transit time-based blood pressure estimation using hilbert-huang transform," in *Proceedings of the 2009 Annual International Conference of the IEEE Engineering in Medicine and Biology Society*, pp. 1785–1788, Minneapolis, MN, September 2009.
- [18] C. Lin, M. Lo, and C. Guilleminault, "Exploring the Abnormal Modulation of the Autonomic Systems during Nasal Flow Limitation in Upper Airway Resistance Syndrome by Hilbert–Huang Transform," *Frontiers in Medicine*, vol. 4, 2017.
- [19] M. Han and M. Wang, "Multichannel EEG feature extraction based on Hilbert-Huang transform and extreme learning machine," vol. 2013, pp. 5406–5409, 2013.
- [20] R. Kumar, R. Ramaswamy, and B. Nath Mallick, "Local Properties of Vigilance States: EMD Analysis of EEG Signals during Sleep-Waking States of Freely Moving Rats," *PLoS ONE*, vol. 8, no. 10, Article ID e78174, 2013.
- [21] J. S. Morris, K. R. Coombes, J. Koomen, K. A. Baggerly, and R. Kobayashi, "Feature extraction and quantification for mass spectrometry in biomedical applications using the mean spectrum," *Bioinformatics*, vol. 21, no. 9, pp. 1764–1775, 2005.
- [22] Z. H. Wu and N. E. Huang, "A study of the characteristics of white noise using the empirical mode decomposition method," *Proceedings of the Royal Society A Mathematical, Physical and Engineering Sciences*, vol. 460, no. 2046, pp. 1597–1611, 2004.

Research Article

Wall Shear Stress Estimation of Thoracic Aortic Aneurysm Using Computational Fluid Dynamics

J. Febina,¹ Mohamed Yacin Sikkandar ,² and N. M. Sudharsan ³

¹Department of Biomedical Engineering, GRT Institute of Engineering and Technology, Tiruttani, India

²Department of Medical Equipment Technology, College of Applied Medical Sciences, Majmaah University, Al Majmaah 11952, Saudi Arabia

³Department of Mechanical Engineering, Rajalakshmi Engineering College, Chennai, India

Correspondence should be addressed to Mohamed Yacin Sikkandar; m.sikkandar@mu.edu.sa

Received 1 February 2018; Revised 16 April 2018; Accepted 30 April 2018; Published 3 June 2018

Academic Editor: Dominique J. Monlezun

Copyright © 2018 J. Febina et al. This is an open access article distributed under the Creative Commons Attribution License, which permits unrestricted use, distribution, and reproduction in any medium, provided the original work is properly cited.

An attempt has been made to evaluate the effects of wall shear stress (WSS) on thoracic aortic aneurysm (TAA) using Computational Fluid Dynamics (CFD). Aneurysm is an excessive localized swelling of the arterial wall due to many physiological factors and it may rupture causing shock or sudden death. The existing imaging modalities such as MRI and CT assist in the visualization of anomalies in internal organs. However, the expected dynamic behaviour of arterial bulge under stressed condition can only be effectively evaluated through mathematical modelling. In this work, a 3D aneurysm model is reconstructed from the CT scan slices and eventually the model is imported to Star CCM+ (Siemens, USA) for intensive CFD analysis. The domain is discretized using polyhedral mesh with prism layers to capture the weakening boundary more accurately. When there is flow reversal in TAA as seen in the velocity vector plot, there is a chance of cell damage causing clots. This is because of the shear created in the system due to the flow pattern. It is observed from the proposed mathematical modelling that the deteriorating WSS is an indicator for possible rupture and its value oscillates over a cardiac cycle as well as over different stress conditions. In this model, the vortex formation pattern and flow reversals are also captured. The non-Newtonian model, including a pulsatile flow instead of a steady average flow, does not overpredict the WSS (15.29 Pa compared to 16 Pa for the Newtonian model). Although in a cycle the flow behaviour is laminar-turbulent-laminar (LTL), utilizing the non-Newtonian model along with LTL model also overpredicted the WSS with a value of 20.1 Pa. The numerical study presented here provides good insight of TAA using a systematic approach to numerical modelling and analysis.

1. Introduction

Aorta is the major artery that carries blood from heart to all parts of the body and part of the aorta that runs through the chest is called thoracic aorta [1]. When an area of thoracic aorta expands or bulges, it is called a thoracic aortic aneurysm (TAA). According to the study of incidence and mortality rate of TAA, the incidence of ruptured thoracic aneurysms in individuals aged 60–69 years is about 100 cases per 10,000; in those aged 70–79 years, it is about 300 cases per 10,000 and in those aged 80–89 years, it is about 550 cases per 10,000 people [1]. TAA causes plaque formation, which is a serious health risk as it can burst or rupture the inner wall intima continuing to the outer wall adventitia. However,

plaque cap rupture per se does not lead to stoppage of blood flow. Rather, plaque cap rupture provides a surface that initiates thrombosis, which may then grow to occlude the vessel and stop blood flow [2]. TAA exists in both saccular shape and fusiform shape. The saccular shape aneurysm is eccentric, involving only one portion of the circumference of an aortic wall. The fusiform aneurysm is concentric and involves the full circumference of the vessel wall. The effect of high shear hemodynamics on thrombus growth has profound implications for the understanding of all acute thrombotic cardiovascular events as well as for vascular reconstructive techniques and vascular device design, testing, and clinical performance [3]. In the present work, saccular shape TAA is considered in detail due to the fact that it has caused

TABLE 1: Derived values of aortic diameter, average velocity, and Reynolds number.

Patient No. *	D = (Re* μ)/(V _{peak}) Aortic diameter (D) (m)	V _{avg} = Q/A Average velocity (m/sec) (V _{avg})	Re _{avg} = (ρ *D*V _{avg})/ μ Average Reynolds number (Re _{avg})
2	0.0302	0.1229	730.03
3	0.0287	0.1333	797.38
4	0.0262	0.1629	856.39
5	0.0261	0.1674	844.23
6	0.0304	0.1281	811.12

*Table 1 of Stein et al. [4].

greater rupture risks than fusiform aneurysm [3]. This work aims to show that Computational Fluid Dynamics (CFD) is an effective tool that can provide better insights into TAA diagnosis with proper solver settings and a numerical protocol.

The viscosity values for a group of five normal people were estimated by Stein et al. [4] to be in the range of 0.0051 to 0.0055 Pa s (average value of 0.0053 Pa s) and the same has been used in the present study (Table 1). The aorta diameter was computed using the peak Reynolds number, peak velocity, and viscosity. This value was then used to obtain the average velocity and Reynolds number. The density value of blood is taken to be $\rho = 1060 \text{ kg/m}^3$. It can be seen from table that the flow of blood inside aorta is predominantly laminar in nature. Owing to the pulsatile nature, the flow is sometimes (locally) turbulent. The derived values obtained from Stein et al. [4] are shown in Table 1.

From Table 1, it is clear that turbulent flow occurs only with peak blood flow velocity values. With average velocity values, the flow tends to be laminar with the average Reynolds number in the range of 730 to 856. A regular geometry profile that mimics an aneurysm was modelled and numerically solved by Berguer et al. [5]. Both laminar and turbulent pulsatile flows were studied. The actual diseased model was not studied. The effects of Newtonian and non-Newtonian behaviours of blood were compared. They concluded that non-Newtonian turbulent flow is to be considered in the study of aneurysms. It is to be noted that the pulsatile flow will be both laminar and turbulent based on the velocity attained at that instant of time. A transit model that could best handle both laminar and turbulent flow would be a better predictor of the flow phenomenon and provide more acceptable wall shear stress values.

A transitional flow model based on Menter et al. [6] was employed by Tan et al. [7] for predicting the blood flow patterns in a fusiform aneurysm region assuming the blood to be Newtonian in nature. In essence, although the flow was pulsatile with a major pulse component being laminar in nature, the transitional flow model solves the fluid flow in the near wall region as laminar and turbulent elsewhere. From the simulation results, they observed that the transitional model gave better inference compared with the laminar simulation. Highly disturbed, recirculating flow was observed within the bulged region of the aneurysm. High

turbulence intensity values were particularly observed near the outlet of the aneurysm. It was also presented that the wall shear stress values obtained could be an overestimate. It would be of interest to investigate an appropriate transitional model considering blood to be non-Newtonian in nature on a saccular aneurysm of a diseased aorta. However, the effective implementation of this basic scheme requires a very fine grid resolution near the wall region. The suggested y^+ (nondimensional distance from wall) value is < 2 . This is extremely fine and would be computationally intensive. The detailed significance and explanation of computation is presented under the numerical protocol section of this paper. An optimum solution to this would be to achieve a good prediction even with a comparative fine mesh having a selected wall y^+ value of 100, at the same time taking care to ensure that the laminar/turbulent transition is in a pulsatile flow instead of using the typical transitional flow model.

A. C. Benim et al. [8] observed that, for a normal human aorta, time averaged velocity field of pulsatile flow did not show remarkable differences in steady-state results. They indicated that the mobilization of atherosclerotic plaques needs to be considered as a very important issue for extracorporeal circulation. However, the effect of actual flow pattern on a diseased aorta was, however, not studied. A detailed lumen surface representation of aortic aneurysm is very important in the analysis of stress pattern [9]. However, the fluctuations of blood flow inside an aneurysm lumen region were not studied in detail. Qiao et al. described the formation and development of aortic plaque in an aneurysm region using CFD [10]. The simulation was performed for a fusiform aneurysm in the descending aorta with pulsatile flow but the cell refinement and grid independence test were not performed. Callaghan et al. presented a work that combined a 4D flow and CFD simulation of a thoracic aortic aneurysm case [11]. They reported that high wall shear stress values of 20 Pa were found in the ascending aorta during the turbulent flow and concluded that the CFD provides results supplementing the 4D flow data in the understanding of aneurysm development and risk; however, the laminar flow and significance of wall y^+ in the aneurysm model were not studied. Numata et al. [12] and Markl et al. [13] reported that CFD simulation alone does not guarantee fidelity to reproduce in vivo hemodynamics due to inherent model limitations. They noted that the grid resolution errors were a possible source of uncertainty. In order to overcome this, mesh independence study was performed. Soudah et al. [14] provided a detailed methodology and the importance of wall y^+ for capturing the WSS. However, it was computed for the peak systolic instant time using flat inlet velocity profile for a normal aorta. Basri et al. [15] detailed the recent usage of CFD in biomedical applications. The authors reviewed several research papers that studied the use of CFD as a tool for determining the pathophysiology of a cardiovascular system. The abnormalities discussed by the authors included narrowing of aortic wall, leakage of blood from the valve opening, and stenosis conditions. However, the usage of CFD in aneurysm condition was not studied.

In summary, from the analysis of available literature, it is seen that it is necessary to consider a geometry model

that is as close as possible to the real aorta. This can be ensured by using one of the several imaging modalities, like CT. This model has to be discretized (meshed) with proper refinement close to the wall and must be fine enough to avoid numerical errors. In this research work, an aorta having a saccular aneurysm is reconstructed from a CT image. The detailed discretization scheme is an extension of [14] with improvements in mesh topology which are explained in detail in the next section. As far as the physics is concerned, it is seen from literature that the flow should be considered as pulsatile and fluid (blood) as non-Newtonian. The discretization of the geometry is very important to obtain a solution with minimum numerical error. The protocol adopted is presented in detail in the next section. The numerical scheme is the key to accurate prediction. From the study of available literature, it is seen/noted that several schemes have been tried, namely, laminar, turbulent, and transitional models assuming a steady velocity profile and/or pulsatile profile with a Newtonian behaviour. A pulsatile flow with non-Newtonian fluid model has not been attempted thus far/ yet and it is suggested that this improved method of approach with above-mentioned modelling parameters would provide a more accurate estimation of WSS values.

In this research work, an attempt is made to test the efficacy of the numerical scheme by comparing the results obtained using a pulsatile velocity profile for both Newtonian and non-Newtonian models considering the flow to be laminar. The reason for using the laminar flow model is that for a pulse of 0.8 seconds the flow is turbulent only from 0.02 to 0.2 seconds, where the Re values exceed 2200. The average Re is always less than 2200. To find an alternate to the transitional model that assumes the bulk of the fluid transport as fully turbulent (which it is not) and also requires a very fine mesh (a computationally intensive proposition), it is proposed to use a laminar-turbulent switch based on the Reynolds number. This is to see if the possibility of overprediction of WSS [8] can be mitigated. The velocity trace can be mapped to a laminar-turbulent-laminar flow from a cardiac cycle. In this model, the velocity trace is mapped to the Reynolds number. For all values of $Re < 2200$, the laminar flow solver is enabled, and for $Re > 2200$, the standard k-epsilon model is enabled.

2. Materials And Methods

2.1. Numerical Evaluation Protocol. The workflow followed in this study is pictorially represented in Figure 1 and is briefly explained below.

2.1.1. Geometry Selection. In this research, the 3D aneurysm model was reconstructed from the CT scan slices using MIMICS. The original CT image file format was DICOM. The total number of scanning slices is 600 and the range of scanning was from neck to legs. The distance between neighbouring layers was 1 mm. The CT data was imported into MIMICS software and data of the aortic vessel was extracted by means of 3D threshold segmentation. Then, the model is imported to Star CCM+ (Siemens, USA) for CFD analysis. The domain is discretized using polyhedral mesh with prism

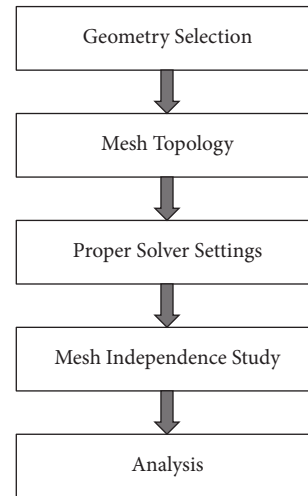


FIGURE 1: Workflow.

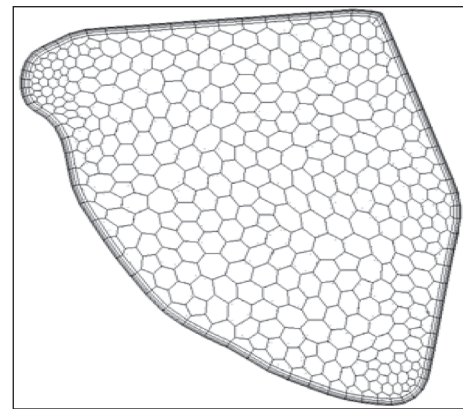


FIGURE 2: Prism layer at the outlet.

layers to capture the boundary more accurately based on the following reasons.

2.1.2. Polyhedral Mesh. Polyhedral meshes provide a balanced solution for complex mesh generation problems. They are relatively easy and efficient to build, requiring no more surface preparation than the equivalent tetrahedral mesh. They also contain approximately five times fewer cells than a tetrahedral mesh for a given starting surface. Multiregion meshes with a conformal mesh interface are allowed.

2.1.3. Prism Layer Mesh. The prism layer mesh model as shown in Figure 2 is used with a core volume mesh to generate orthogonal prismatic cells next to wall surfaces or boundaries. This layer of cells is necessary to improve the accuracy of the flow solution and provides a conformal mesh for the model. This helps in capturing the velocity across the boundary layer more accurately than depending on standard wall functions. This is decided from the wall y^+ value that is discussed later in this section. It is to be noted that Figure 2 presents only the representation of the prismatic layer near wall with polyhedral cells in the center. The actual mesh is

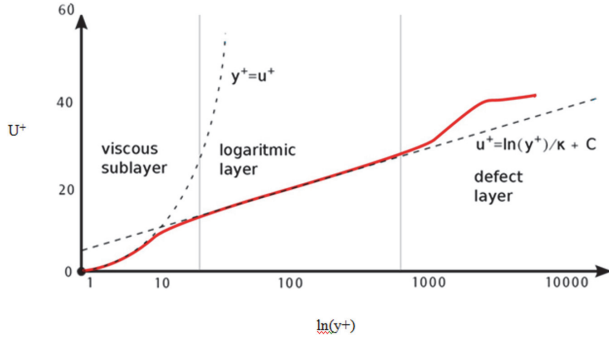


FIGURE 3: Nondimensional distance from wall y^+ versus nondimensional velocity U^+ .

extremely fine (average distance from the wall to the adjacent grid is 0.0001 m.) and one would not be able to see the geometric progression of cell layer thickness from wall to the inner fluid region.

2.1.4. Significance of Wall y^+ Value. To understand the actual physics of wall shear stress, the flow close to the boundary layer has to be accurately captured. Since the boundary layer thickness is extremely small, the first grid point must be very close to the wall. This distance from the wall is represented as nondimensional wall y^+ .

$$y^+ = \frac{y u_\tau}{\vartheta}, \quad u_\tau = \sqrt{\frac{\tau_w}{\rho}} \quad (1)$$

where

- y^+ is nondimensional distance from the wall,
- y is the distance from the wall, m,
- u_τ is frictional velocity,
- ϑ is kinematic viscosity, m^2/s ,
- τ_w is wall shear stress, Pa,
- ρ is density, kg/m^3 .

The velocity profile close to the wall is generally assumed to be parabolic and the boundary layer variation is assumed to be parabolic. However, this is not the case. The nondimensional velocity u^+ is plotted against the nondimensional distance from the wall and defined as y^+ (Figure 3). As seen in Figure 3, the boundary layer can be divided into three regions and they are viscous sublayer, log layer, and defect layer. In the viscous sublayer $y^+ = u^+$ and this holds good for a value of y^+ up to 5. It means that the viscous forces are as strong as the inertial forces. In the log layer, the u^+ value increases exponentially in comparison to the distance from the wall and is linear when plotted in logarithmic scale.

Wall y^+ value indicates the position of the grid inside the boundary layer. A value of less than five signifies that the first grid is in viscous sublayer and a value of 300 signifies that the first grid is in log layer. It is desirable that y^+ be in this range to ensure that the physics of boundary layer are truly represented in this study's computation even though standard

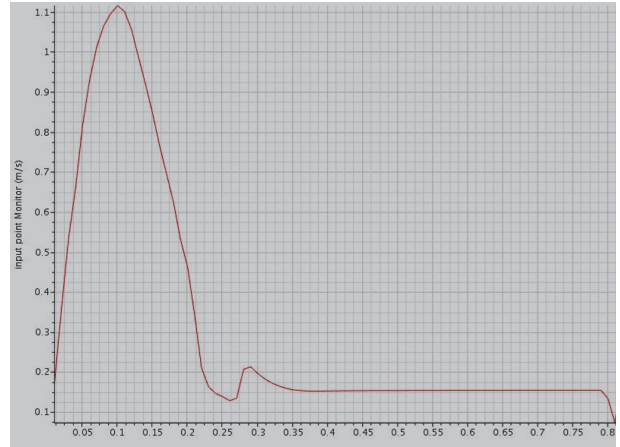


FIGURE 4: Velocity profile graph [15].

wall functions are enabled. In this case, y^+ ranges from 3 to 100, respectively. This clearly satisfies the condition that, in the present simulation, the flow inside boundary layer is fully represented by the prism layer grid points.

2.1.5. Mesh Independence Study. In order to avoid the grid resolution errors, three different mesh models are generated in the fluid domain. The number of cells generated is two, four, and eight hundred thousand, respectively. The number of prism layers is set to four for capturing the near-wall velocity profile. The simulations were performed for pulsatile velocity profile of a typical resting condition on the aneurysm region in thoracic aorta and the results presented are of a male person (age 61) in Figure 4. The velocity profile was obtained from the published literature [15].

The simulation is performed assuming Newtonian behaviour. The simulation is run for 6 cycles to allow the solver to stabilize and the results for the seventh cycle are plotted. Three points are monitored. Point 1 corresponds to inlet, point 2 corresponds to the location where the aneurysm is present, and point 3 refers to the outlet (Figure 5). Figures 6–8 present the velocity profile over time for various mesh counts. The negative value in the velocity is because the flow is considered to be positive in the upward direction in the inlet region. It can be seen from all the three figures that the mesh-independent solution is reached for a mesh count of 400,000. However, for ensuring fidelity, all further simulations are performed with a refined mesh having a mesh count of 800,000.

2.1.6. Solver Settings. Regarding physical conditions, they include unsteady, pulsatile, and laminar, segregated flows. The laminar flow is considered based on the value obtained from the Reynolds number. The average Reynolds number for pulsatile flow is 1405. From the velocity profile, it is found that 78% is laminar and 22% is turbulent. As the flow is predominantly laminar, the laminar flow model is chosen. However, the laminar-turbulent-laminar (LTL) model is also simulated for comparison.

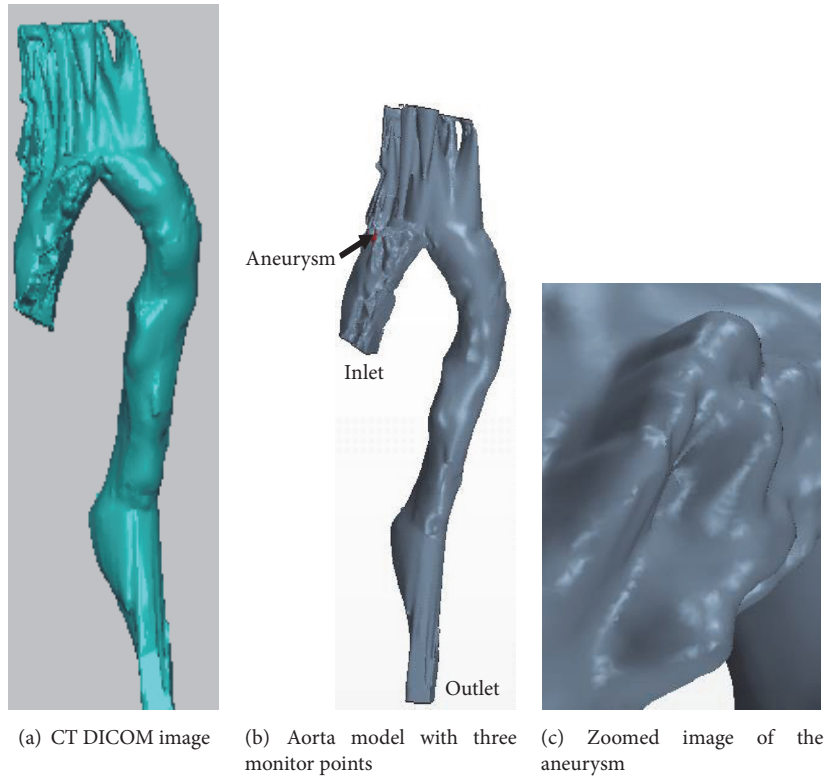


FIGURE 5

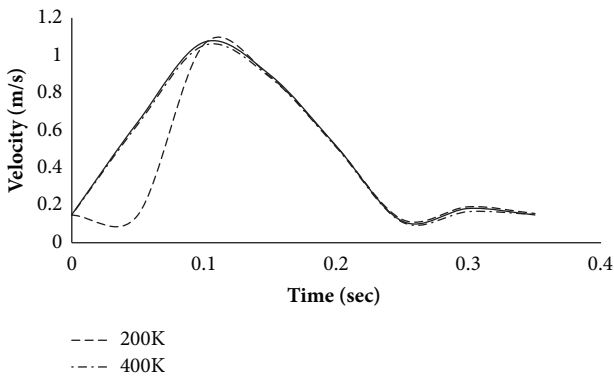


FIGURE 6: Velocity profile over time at monitoring point 1 (inlet) for various mesh counts.

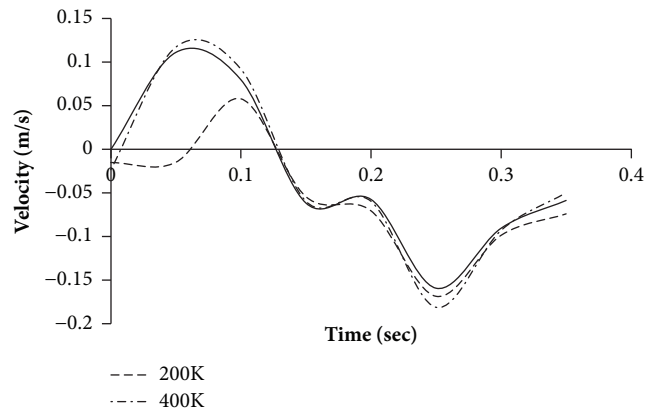


FIGURE 7: Velocity profile over time at monitoring point 2 (aneurysm) for various mesh counts.

Regarding boundary conditions, the inlet boundary condition is velocity inlet and the velocity profile given in the inlet is shown in Figure 5(a). For CFD analysis, the average velocity has to be set as an inlet boundary condition instead of using peak velocity value. The wall is assumed to be rigid and no slip condition is set in the wall. The outlet boundary condition is the pressure outlet.

For Newtonian or non-Newtonian fluid, generally, blood follows a Newtonian behaviour in large arteries and non-Newtonian behaviour in small arteries and capillaries. But in both medium and large sized blood vessels, non-Newtonian behaviour influences hemodynamic factors [16–18]. To understand this effect, non-Newtonian model of blood

is also adopted and compared with the results obtained using Newtonian flow. The viscosity of the blood is set at 0.0052 Pa-s based on the experimental results reported in [4].

During the steady state, non-Newtonian behaviour affects the wall shear stress predicting larger values than the Newtonian model [16, 17, 19–21]. Solving this aorta model assuming a steady average velocity, WSS value is estimated as 13.2 Pa for non-Newtonian model, which is higher than the WSS value of Newtonian model (7.4 Pa). But when pulsatile flow is considered, Newtonian behaviour tends to provide larger WSS than the non-Newtonian behaviour as can be seen from the graph presented above (Figure 9) with average values

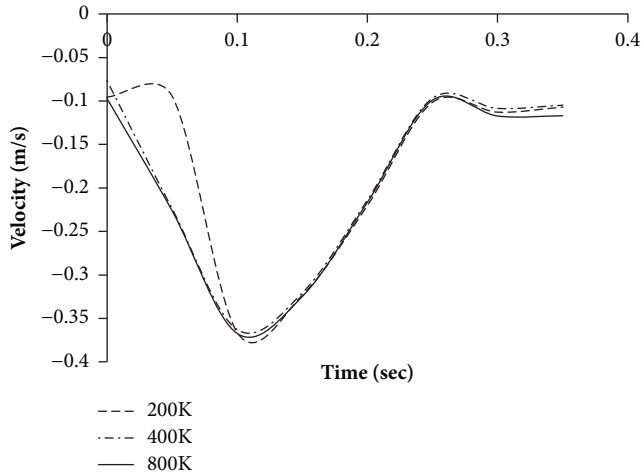


FIGURE 8: Velocity profile over time at monitoring point 3 (outlet) for various mesh counts.

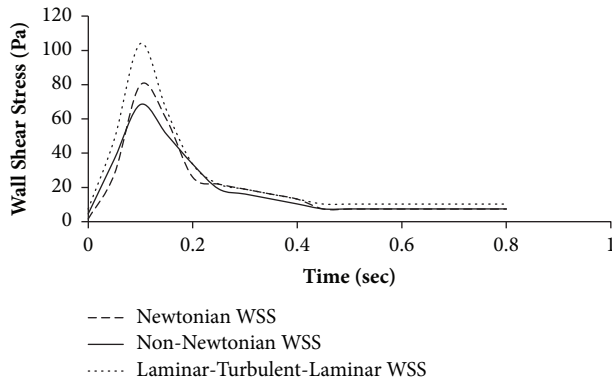


FIGURE 9: Pulsatile flow wall shear stress versus time for Newtonian and non-Newtonian WSS.

of 16 Pa and 15.29 Pa, respectively. The graph also shows the laminar-turbulent-laminar (LTL) model proposed in this paper. This model (LTL) overpredicts WSS with an average value of 20.10 Pa. In effect, it is amply evident from this work and others that considering blood flow as laminar is the right assumption/presumption.

The simulation was performed based on three conditions: during rest, light exercise, and moderate exercise. The velocity profile varies with the stress condition and the same is presented in Figure 10.

3. Result and Discussion

We consider the velocity profile and vorticity at the three peaks at 0.05, 0.25, and 0.75 time instants in the velocity profile of blood flow during rest, light exercise, and moderate exercise positions (Figure 10).

From Figure 10, it is observed that, for moderate exercise conditions, the velocity profile has peaks at 0.05, 0.25, 0.4, and 0.75 seconds and two peaks for the other two stress conditions. The corresponding velocity vector at these three time instants is plotted in Figure 10.

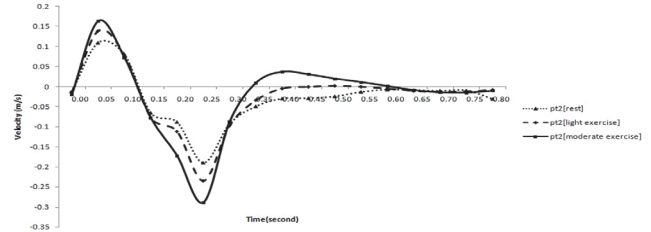


FIGURE 10: Velocity in the aneurysm region at different exercise conditions. Note: pt2 indicates the point in the aneurysm region.

Figures 11(a) and 11(b) indicate the vector scene represented during the first peak in Figure 10 at the aneurysm point for both laminar and laminar-turbulent-laminar methods. This shows that the flow is towards the left side, which makes the base for the formation of vortex. Figure 11(c) presents the vorticity plot at the same time instant. The vorticity value at the aneurysm using laminar method is 110.7285(/s) and for LTL method it is 221.6708 (/s). Although the pulsatile flow behaves as a laminar-turbulent-laminar based on the velocity profile, it overpredicts the values when compared to a laminar method. This again fortifies that the simulation needs to be performed using a non-Newtonian and laminar scheme.

Figure 12 indicates the flow reversal in the aneurysm region (i.e., flow towards the right). Figure 12(c) presents the vorticity plot at the same time instant. The vorticity value at the aneurysm using laminar method is 111.07(/s) and for LTL method it is 182.44 (/s).

In Figure 13, the flow is towards the left side and this vector scene is obtained during the second positive peak in Figure 10. Figure 13(c) presents the vorticity plot at the same time instant. The vorticity value at the aneurysm using laminar method is 19.39(/s) and for laminar-turbulent-laminar method it is 46.98 (/s).

In Figures 14(a) and 14(b), the flow vector direction is towards the right, indicating the flow reversal in the aneurysm region again. This flow reversal may have an effect on wall abrasion and the possibility of rupture. There is an increase in peak velocity of flow in the ascending aorta with exercise [22]. Figure 14(c) presents the vorticity plot at the same time instant. The vorticity value at the aneurysm using laminar method is 13.5542 (/s) and for laminar-turbulent-laminar method it is 31.3758(/s).

According to Taylor [23], for a normal person, reverse flow occurs in aorta during rest and reverse flow gets eliminated during exercise. The present model was carried out on subject with aneurysm and from the analysis it was found that there is reverse flow and flow fluctuations during exercise condition in the aneurysm region, which could lead to rupture.

Although the LTL scheme provides the same vector scene as non-Newtonian model, the WSS is comparatively high for the laminar-turbulent-laminar scheme. Also the vorticity value is high for the laminar-turbulent-laminar scheme when compared to the laminar scheme.

The WSS is associated with blood flow through an artery and also depends on the size and geometry of an aorta. The

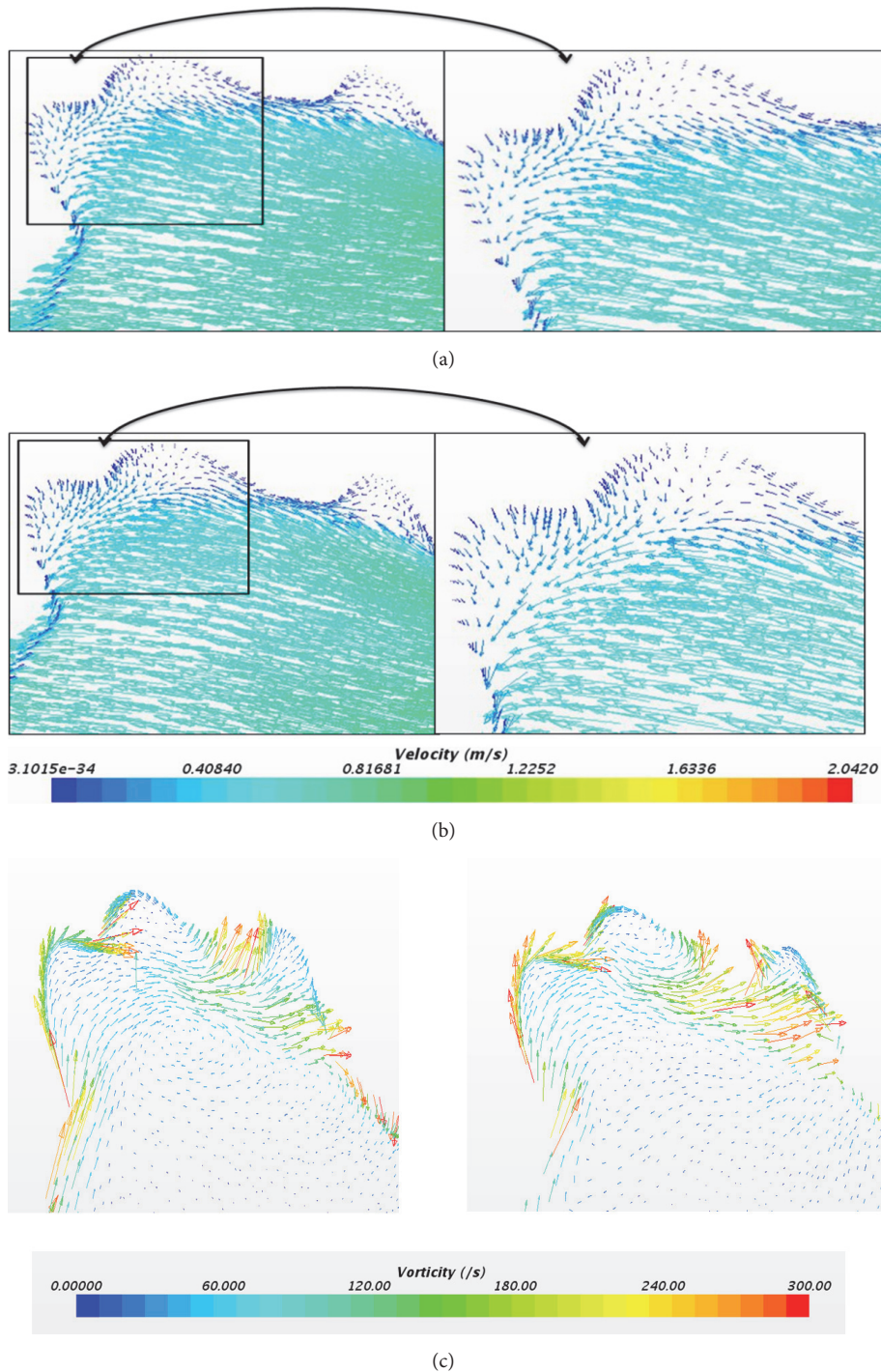


FIGURE 11: (a) Velocity profile at 0.05 sec using laminar method. (b) Velocity profile at 0.05 sec using laminar-turbulent-laminar scheme. (c) Vorticity profile using laminar and laminar-turbulent-laminar methods at 0.05 sec.

corresponding WSS during rest, light exercise, and moderate exercise are shown in Figures 15 and 16.

From this, it is clear that laminar-turbulent-laminar scheme overpredicts high WSS values. So, the alternate choice of the non-Newtonian model with laminar flow can provide better results among the different models discussed above.

WSS is an important factor for rupture and plaque formation. Results so far published in open literature have emphasised that the WSS is overpredicted in a numerical experiment. Numerical results heavily depend on the settings and these have not been well documented so far. In order to obtain solutions that match the physical experiments, there is

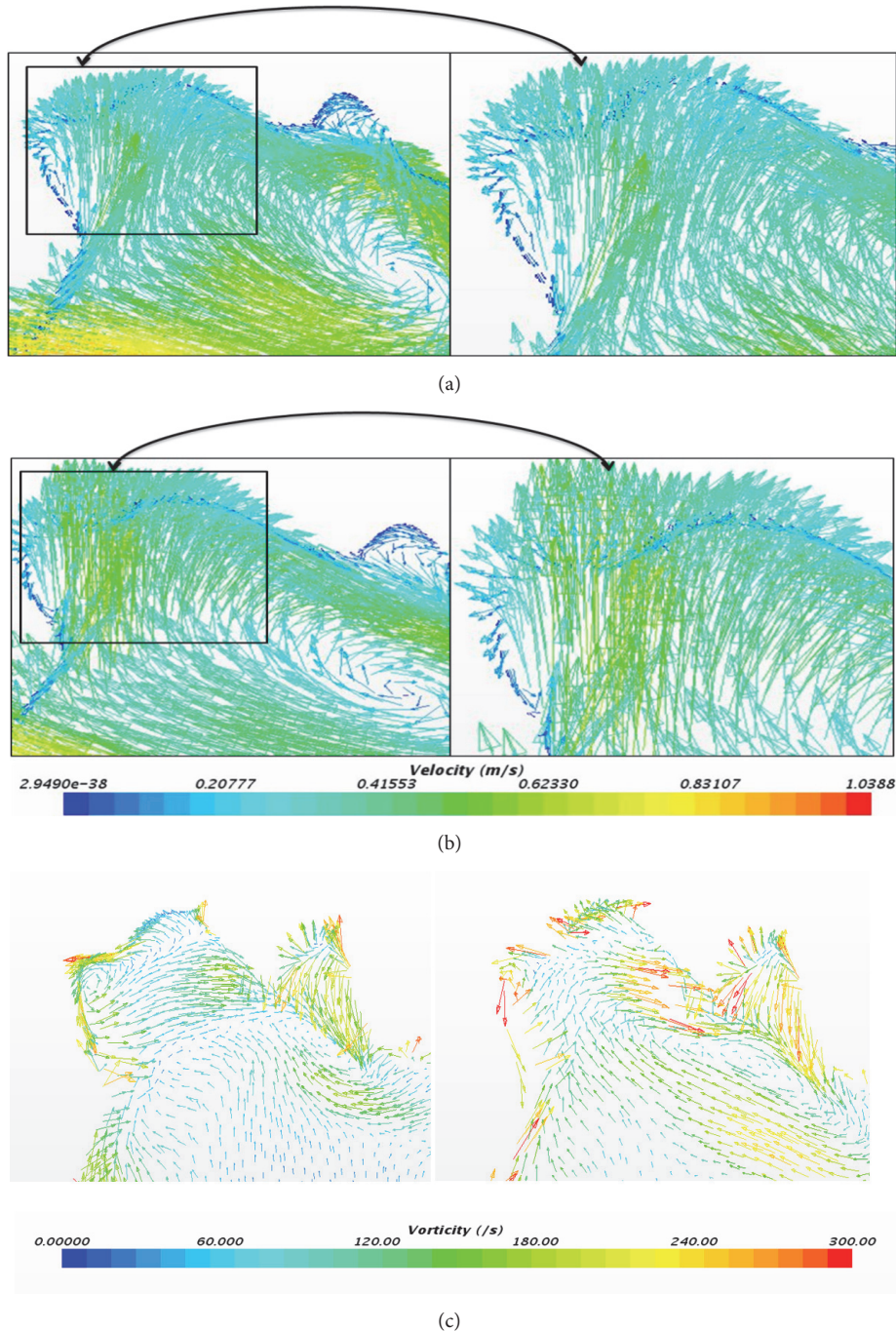


FIGURE 12: (a) Velocity profile at 0.25 sec using laminar method. (b) Velocity profile at 0.25 sec using laminar-turbulent-laminar scheme. (c) Vorticity profile using laminar and laminar-turbulent-laminar methods at 0.25 sec.

a need for (a) proper extraction of the geometry without loss of detail and a good discretization scheme; (b) choice of flow; and (c) choice of physics. These are explained in detail below.

The discretization of the geometry must follow a protocol in such a way that the near-wall region is adequately captured along with a mesh-independent study to check the fidelity of the solution. Although the flow behaviour is laminar-turbulent-laminar over a cardiac cycle, it has been seen that this model overpredicts WSS as well as the vorticity. Surprisingly, it is assumed that the flow to be laminar provides a

better estimate for WSS. Also the physics of the fluid are taken as non-Newtonian and this provides a better result than Newtonian. It is to be noted that a pulsatile flow with non-Newtonian fluid model has not been attempted so far and seen as an improved method of approach with above-mentioned modelling parameters to estimate the WSS more accurately.

Also, the development of vortex and flow reversal is presented in this work, which is a possible reason for formation of plaque deposition. This is a cause for reduction

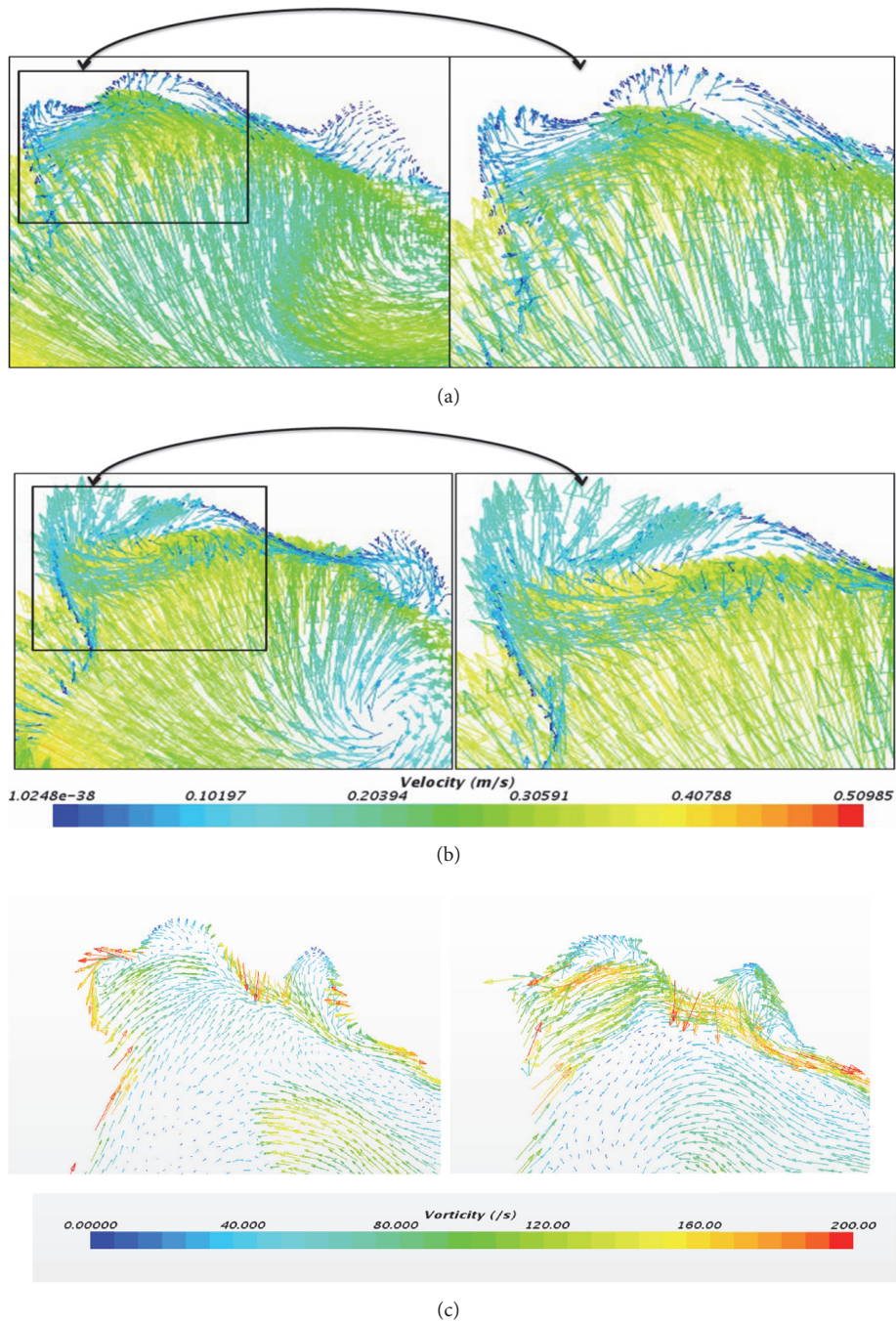


FIGURE 13: (a) Velocity profile at 0.4 sec using laminar method. (b) Velocity profile at 0.4 sec using laminar-turbulent-laminar scheme. (c) Vorticity profile using laminar and laminar-turbulent-laminar method at 0.4 sec.

in flow area and increase in internal pressure. This insight on the flow reversal and vortex development has not yet been explored based on the available literature to the best of the authors' knowledge. Chatzizisis et al. and Chen et al. have presented that, at locations where there is a presence of atherosclerotic lesions, oscillatory or low shear stress is predominantly observed [24, 25]. However, Chen et al.

also observe that effect of stress on plaque is unknown [25].

4. Conclusion

The conformal mesh for the model is obtained using the polyhedral and prism layer mesh. The flow along the sides of

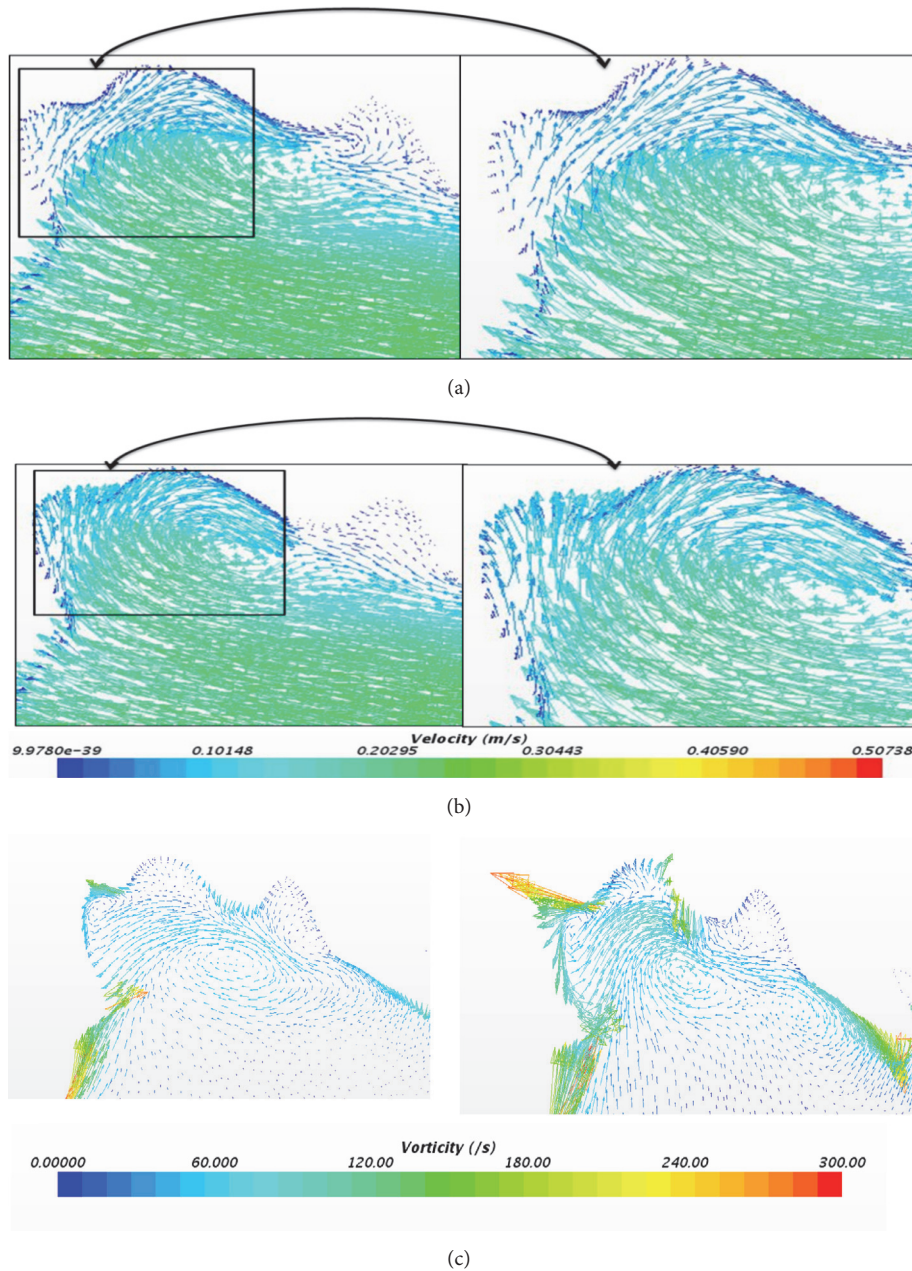


FIGURE 14: (a) Velocity profile at 0.75 sec using laminar method. (b) Velocity profile at 0.75 sec using laminar-turbulent-laminar scheme. (c) Vorticity profile using laminar and laminar-turbulent-laminar method at 0.75 sec.

the wall is captured well by using wall y^+ . It has been observed that considering pulsatile blood flow to be laminar is correct and it does not overpredict the WSS values. Moreover, it is also found necessary to consider the blood to be non-Newtonian even when the flow is in the larger blood vessel. The true representation of the geometry, discretization with fine meshes in the near wall region ($y^+ < 100$), and the proper choice of numerical scheme are the keys to correct prediction of flow and WSS. CFD as a mathematical tool can help in understanding the flow physics phenomena inside

an artery. The advantage is that the model can be tested for varying stresses that an artery may be subjected (to) in day to day life. This tool will help in evaluating treatment methodology and suggest lifestyle modifications for the diseased patient. Thus, the relationship between CFD and cardiovascular hemodynamics was studied with different assumptions. It was found that CFD can provide better results with proper modelling, mesh, and solver settings. Limitation of this study is that the present findings are based on limited population (i.e., one particular case). In future, more CT data

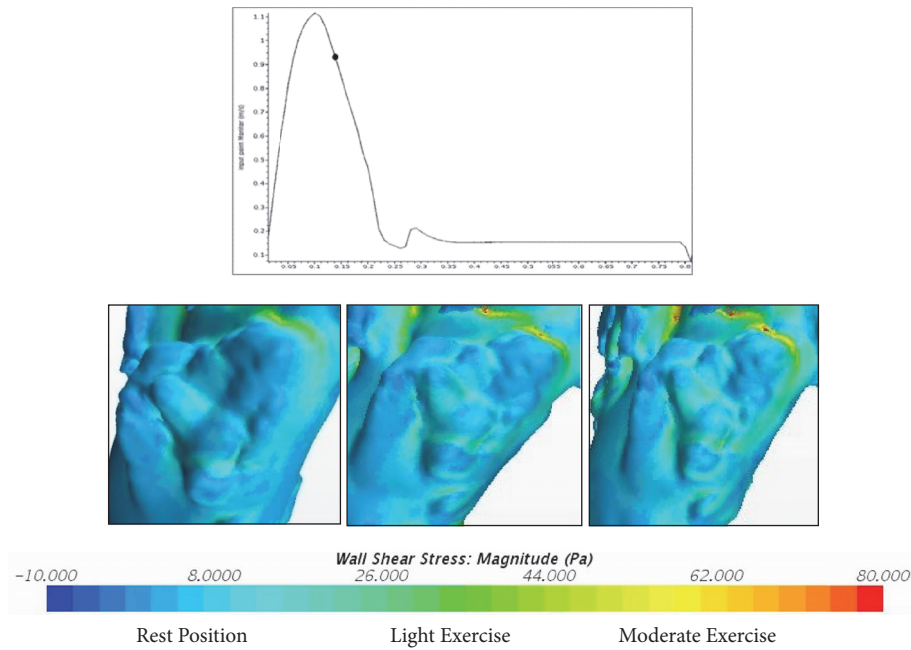


FIGURE 15: WSS during rest, light exercise, and moderate exercise at 0.15 sec.

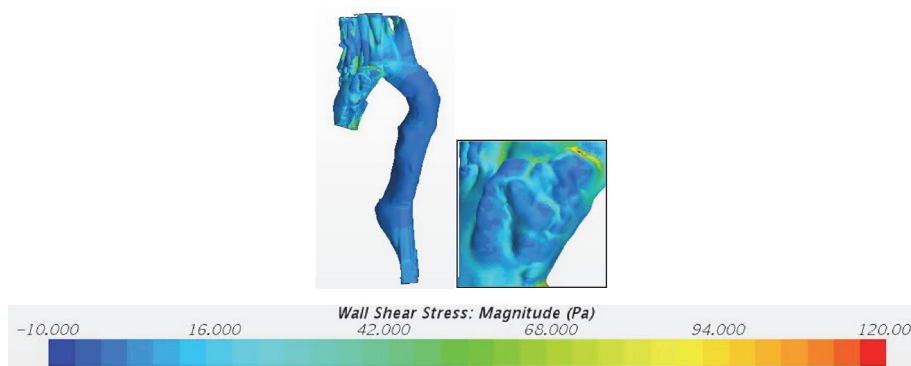


FIGURE 16: Wall shear stress during moderate exercise using the laminar-turbulent-laminar scheme.

of saccular shape thoracic aortic aneurysm patients can be obtained and then simulation can be done to provide more appropriate numerical results.

Data Availability

The clinical data are available upon request in accordance with the volunteers' informed consent. The data will not be shared online.

Conflicts of Interest

The authors declare that they have no conflicts of interest.

References

- [1] R. Erbel and H. Eggebrecht, "Aortic dimensions and the risk of dissection," *Heart*, vol. 92, no. 1, pp. 137–142, 2006.
- [2] L. D. C. Casa, D. H. Deaton, and D. N. Ku, "Role of high shear rate in thrombosis," *Journal of Vascular Surgery*, vol. 61, no. 4, pp. 1068–1080, 2015.
- [3] E. K. Shang, D. P. Nathan, W. W. Boonn et al., "A modern experience with saccular aortic aneurysms," *Journal of Vascular Surgery*, vol. 57, no. 1, pp. 84–88, 2013.
- [4] P. D. Stein and H. N. Sabbah, "Turbulent blood flow in the ascending aorta of humans with normal and diseased aortic valves," *Circulation Research*, vol. 39, no. 1, pp. 58–65, 1976.
- [5] R. Berguer, J. L. Bull, and K. Khanafer, "Refinements in mathematical models to predict aneurysm growth and rupture," *Annals of the New York Academy of Sciences*, vol. 1085, pp. 110–116, 2006.
- [6] F. R. Menter, R. B. Langtry, S. R. Likki, Y. B. Suzen, P. G. Huang, and S. Volker, "A correlation-based transition model using local variables, part i - model formulation," in *Proceedings of the ASME Turbo Expo 2004: Power for Land, Sea, and Air*, pp. 57–67, Vienna, Austria, 2004.

- [7] F. P. P. Tan, A. Borghi, R. H. Mohiaddin, N. B. Wood, S. Thom, and X. Y. Xu, "Analysis of flow patterns in a patient-specific thoracic aortic aneurysm model," *Computers and Structures*, vol. 87, no. 11-12, pp. 680–690, 2009.
- [8] A. C. Benim, A. Nahavandi, A. Assmann, D. Schubert, P. Feindt, and S. H. Suh, "Simulation of blood flow in human aorta with emphasis on outlet boundary conditions," *Applied Mathematical Modelling: Simulation and Computation for Engineering and Environmental Systems*, vol. 35, no. 7, pp. 3175–3188, 2011.
- [9] A. Borghi, N. B. Wood, R. H. Mohiaddin, and X. Y. Xu, "3D geometric reconstruction of thoracic aortic aneurysms," *Biomedical Engineering Online*, vol. 5, article no. 59, 2006.
- [10] A.-K. Qiao, W.-Y. Fu, and Y.-J. Liu, "Study on hemodynamics in patient-specific thoracic aortic aneurysm," *Theoretical and Applied Mechanics Letters*, vol. 1, Article ID 014001, 2011.
- [11] F. M. Callaghan, J. Karkouri, K. Broadhouse, M. Evin, D. F. Fletcher, and S. M. Grieve, "Thoracic aortic aneurysm: 4D flow MRI and computational fluid dynamics model," *Computer Methods in Biomechanics and Biomedical Engineering*, vol. 18, pp. 1894-1895, 2015.
- [12] S. Numata, K. Itatani, K. Kanda et al., "Blood flow analysis of the aortic arch using computational fluid dynamics," *European Journal of Cardio-Thoracic Surgery*, vol. 49, no. 6, pp. 1578–1585, 2016.
- [13] M. Markl, G. J. Wagner, and A. J. Barker, "Re: Blood flow analysis of the aortic arch using computational fluid dynamics," *European Journal of Cardio-Thoracic Surgery*, vol. 49, no. 6, pp. 1586-1587, 2016.
- [14] E. Soudah, J. Casacuberta, P. J. Gamez-Montero et al., "Estimation of wall shear stress using 4D flow cardiovascular MRI and computational fluid dynamics," *Journal of Mechanics in Medicine and Biology*, vol. 17, no. 3, Article ID 1750046, 2017.
- [15] E. I. Basri, A. A. Basri, V. N. Riazuddin, S. F. Shahwir, Z. Mohamad, and K. A. Ahmad, "Computational Fluid Dynamics Study in Biomedical Applications: A Review," *International Journal of Fluids and Heat Transfer*, vol. 1, no. 2, 2016.
- [16] S. S. Shibeshi and W. E. Collins, "The rheology of blood flow in a branched arterial system," *Applied Rheology*, vol. 15, no. 6, pp. 398–405, 2005.
- [17] Y. I. Cho and K. R. Kensey, "Effects of the non-Newtonian viscosity of blood on flows in a diseased arterial vessel. Part I: Steady flows," *Biorheology*, vol. 28, no. 3-4, pp. 241–262, 1991.
- [18] F. J. H. Gijssen, E. Allanic, F. N. van de Vosse, and J. D. Janssen, "The influence of the non-Newtonian properties of blood on the flow in large arteries: unsteady flow in a 90° curved tube," *Journal of Biomechanics*, vol. 32, no. 7, pp. 705–713, 1999.
- [19] J. P. W. Baaijens, A. A. Van Steenhoven, and J. D. Janssen, "Numerical analysis of steady generalized Newtonian blood flow in a 2D model of the carotid artery bifurcation," *Biorheology*, vol. 30, no. 1, pp. 63–74, 1993.
- [20] P. Ballyk, D. Steinman, and C. Ethier, "Simulation of non-Newtonian blood flow in an end-to-side anastomosis," *Biorheology*, vol. 31, no. 5, pp. 565–586, 1994.
- [21] D. N. Ku and D. Liepsch, "The effects of non-Newtonian viscoelasticity and wall elasticity on flow at a 90° bifurcation," *Biorheology*, vol. 23, no. 4, pp. 359–370, 1986.
- [22] P. J. Daley, K. B. Sagar, and L. S. Wann, "Doppler echocardiographic measurement of flow velocity in the ascending aorta during supine and upright exercise," *British Heart Journal*, vol. 54, no. 6, pp. 562–567, 1985.
- [23] C. A. Taylor and M. T. Draney, "Experimental and computational methods in cardiovascular fluid mechanics," in *Annual review of fluid mechanics*. Vol. 36, vol. 36 of *Annu. Rev. Fluid Mech.*, pp. 197–231, Annual Reviews, Palo Alto, CA, 2004.
- [24] Y. S. Chatzizisis, A. U. Coskun, M. Jonas, E. R. Edelman, C. L. Feldman, and P. H. Stone, "Role of endothelial shear stress in the natural history of coronary atherosclerosis and vascular remodeling: molecular, cellular, and vascular behavior," *Journal of the American College of Cardiology*, vol. 49, no. 25, pp. 2379–2393, 2007.
- [25] C. Cheng, D. Tempel, R. van Haperen et al., "Atherosclerotic lesion size and vulnerability are determined by patterns of fluid shear stress," *Circulation*, vol. 113, no. 23, pp. 2744–2753, 2006.